# Ferromagnetism in oxide and dichalcogenide based diluted magnetic semiconductors

**Author:**
Ding, Xiang

**Publication Date:**
2019

**DOI:**
https://doi.org/10.26190/unsworks/21441

# Ferromagnetism in Oxide and Dichalcogenide Based Diluted Magnetic Semiconductors

**Xiang Ding**

A thesis in fulfilment of the requirements for the degree of

**Doctor of Philosophy**


School of Materials Science and Engineering

Faculty of Science

University of New South Wales

March 2019

**THE UNIVERSITY OF NEW SOUTH WALES**

**Thesis/Dissertation Sheet**

**Surname or Family name:** Ding

**First name:** Xiang **Other name/s:**

**Abbreviation for degree as given in the University calendar: PhD**

**School:** School of Materials Science & Engineering **Faculty:** Faculty of Science

**Title:** Ferromagnetism in oxide and dichalcogenide based diluted magnetic semiconductors


**Abstract 350 words maximum:**

Over the past decades, the world has witnessed the rapid development of semiconductor industry according to Moore's law. However, the pace of advancement has slowed in recent years and is already nearing its end due to the limits of miniaturization. The industry is in urgent need for new materials and device designs, for example, spintronics. Spintronics is a multifunctional device that utilizes spin degrees of freedom of electrons. The key issue in spintronics is the manipulation of spins. Diluted magnetic semiconductors are able to combine both semiconducting and magnetic properties into spintronics. Room-temperature ferromagnetism has been predicted to achieve in transition metal oxides like $TiO_2$ and transition metal dichalcogenides such as $MoS_2$ and $WS_2$, which are the subjects of this dissertation.

In the first part of this dissertation, 5 at% Co-doped $TiO_2$ thin films were grown on $LaAlO_3$ and $SrTiO_3$ substrates by pulsed laser deposition. The growth mechanism and magnetic properties of the thin films were investigated in detail. It was found that although only anatase phase was observed in X-ray diffraction, the epitaxial films can be either fully strained or fully relaxed based on the choice of deposition substrates. The Co dopants tend to segregate near the interface, but the size and distribution of the nanoclusters depend on the deposition parameters. Higher temperatures and slow growth rate lead to bigger cluster size and greater distance to the interface. The highest magnetic moments reaches 4.73 $\mu_B$/Co at room temperature, supported by the first-principles calculations considering spin-orbit coupling. Polarised neutron reflectometry measurement reveals that Co clusters and possible surrounding defects are the main magnetic sources.

The second part of this dissertation focuses on defect engineering in $WS_2$ and $MoS_2$. Both $WS_2$ annealed in reducing gas and Nd-doped $MoS_2$ show enhanced room-temperature ferromagnetism. The magnetic properties of the annealed $WS_2$ powders are governed by the sulfur vacancies, which significantly increase in density with increased annealing temperature. In the Nd-doped $MoS_2$ crystals, the exchange coupling of $Nd^{3+}$ ions and sulfur vacancies introduced by ion implantation can form magnetic polarons that determine the magnetic properties.

# ORIGINALITY STATEMENT

‘I hereby declare that this submission is my own work and to the best of my knowledge it contains no materials previously published or written by another person, or substantial proportions of material which have been accepted for the award of any other degree or diploma at UNSW or any other educational institution, except where due acknowledgement is made in the thesis. Any contribution made to the research by others, with whom I have worked at UNSW or elsewhere, is explicitly acknowledged in the thesis. I also declare that the intellectual content of this thesis is the product of my own work, except to the extent that assistance from others in the project's design and conception or in style, presentation and linguistic expression is acknowledged.’

Signed …….....

Date …….....

# INCLUSION OF PUBLICATIONS STATEMENT

UNSW is supportive of candidates publishing their research results during their candidature as detailed in the UNSW Thesis Examination Procedure.

**Publications can be used in their thesis in lieu of a Chapter if:**

- The student contributed greater than 50% of the content in the publication and is the "primary author", ie. the student was responsible primarily for the planning, execution and preparation of the work for publication
- The student has approval to include the publication in their thesis in lieu of a Chapter from their supervisor and Postgraduate Coordinator.
- The publication is not subject to any obligations or contractual agreements with a third party that would constrain its inclusion in the thesis

Please indicate whether this thesis contains published material or not.

☐ *This thesis contains no publications, either published or submitted for publication (if this box is checked, you may delete all the material on page 2)*

☐ *Some of the work described in this thesis has been published and it has been documented in the relevant Chapters with acknowledgement (if this box is checked, you may delete all the material on page 2)*

☐ *This thesis has publications (either published or submitted for publication) incorporated into it in lieu of a chapter and the details are presented below*

**CANDIDATE'S DECLARATION**

I declare that:

- I have complied with the Thesis Examination Procedure
- where I have used a publication in lieu of a Chapter, the listed publication(s) below meet(s) the requirements to be included in the thesis.

| **Name** | **Signature** | **Date (dd/mm/yy)** |
|---|---|---|
| | | |

**Postgraduate Coordinator's Declaration (to be filled in where publications are used in lieu of Chapters)**

I declare that:

- the information below is accurate
- where listed publication(s) have been used in lieu of Chapter(s), their use complies with the Thesis Examination Procedure
- the minimum requirements for the format of the thesis have been met.

| **PGC's Name** | **PGC's Signature** | **Date (dd/mm/yy)** |
|---|---|---|
| | | |

# COPYRIGHT STATEMENT



# AUTHENTICITY STATEMENT

# ACKNOWLEDGEMENT

I would first like to offer my sincere thanks to my supervisors, Prof. Jiabao Yi and Prof. Tao Wu. I am grateful for their continuing guidance and support throughout my Ph.D research. Furthermore, they have given numerous precious suggestions in my academic writing. I am deeply indebted to them for the valuable advices to improve this thesis. I would also like to thank my co-supervisor, Dr. Judy Hart, for her enthusiasm and encouragement.

Secondly, I would like to express my appreciations to all the lab managers and technicians who have help me overcome various difficulties in experiments. Special thanks to Dr. Jeffrey Cheung in ANFF and Dr. Sean Lim and Dr. Yin Yao in EMU for their expertise in PLD and other equipment. I am also grateful to all my all my group members for their kind companionship, including Li-Ting Tseng, Yiren Wang, Sohail Ahmed, Xun Geng and Mengyao Li, and Shu Li.

Finally, I must express my very profound gratitude to my parents for their support in my life.

# LIST OF PUBLICATIONS

1. **X. Ding**, T. Liu, S. Ahmed, N. Bao, J. Ding, and J. B. Yi. "Enhanced ferromagnetism in $WS_2$ via defect engineering." *Journal of Alloys and Compounds*, 772 (2019): 740.

2. **X. Ding**, and J. B. Yi. "Synthesis and Applications of 2d Transition Metal Dichalcogenides." In Functional Materials and Electronics, *Apple Academic Press*, 2018, pp. 1-33.

3. S. Ahmed, **X. Ding**, N. Bao, P. Bian, R. Zheng, Y. Wang, P. P. Murmu, J.V. Kennedy, R. Liu, H. Fan, and K. Suzuki. "Inducing high coercivity in $MoS_2$ nanosheets by transition element doping." *Chemistry of Materials*, 29(21) (2017): 9066.

4. L. T. Tseng, A. Suter, Y. Wang, F. Xiang, P. Bian, **X. Ding**, A. Tseng, H. Hu, H. Fan, R. Zheng, and X. Wang. "Intrinsic and spatially nonuniform ferromagnetism in Co-doped ZnO films." *Physical Review B*, 96(10) (2017): 104423.

5. X. Luo, L.T. Tseng, Y. Wang, N. Bao, Z. Lu, **X. Ding**, R. Zheng, Y. Du, K. Huang, L. Shu, and A. Suter. "Intrinsic or Interface Clustering-Induced Ferromagnetism in Fe-Doped $In_2O_3$-Diluted Magnetic Semiconductors." *ACS applied materials & interfaces*, 10(26) (2018): 22372.

6. S. Ahmed, P. Viboon, **X. Ding**, N. Bao, Y. H. Du, T. S. Herng, J. Ding, and J. B. Yi. "Annealing effect on the ferromagnetism of $MoS_2$ nanoparticles." *Journal of Alloys and Compounds*, 746 (2018): 399.

7. S. Ahmed, **X. Ding**, P.P. Murmu, N. Bao, R. Liu, J. Kennedy, J. Ding, and J. B. Yi. "Magnetic properties of Co doped $WSe_2$ by implantation." *Journal of Alloys and Compounds*, 731 (2018): 25.

# ABSTRACT

Over the past decades, the world has witnessed the rapid development of semiconductor industry according to Moore's law. However, the pace of advancement has slowed in recent years and is already nearing its end due to the limits of miniaturization. The industry is in urgent need for new materials and device designs, for example, spintronics. Spintronics is a multifunctional device that utilizes spin degrees of freedom of electrons. The key issue in spintronics is the manipulation of spins. Diluted magnetic semiconductors are able to combine both semiconducting and magnetic properties into spintronics. Room-temperature ferromagnetism is expected in transition metal oxides like $TiO_2$ and transition metal dichalcogenides such as $MoS_2$ and $WS_2$, which are the subjects of this dissertation.

In the first part of this dissertation, 5 at% Co-doped $TiO_2$ thin films were grown on $LaAlO_3$ and $SrTiO_3$ substrates by pulsed laser deposition. The growth mechanism and magnetic properties of the thin films were investigated in detail. It was found that although only anatase phase was observed in X-ray diffraction, the epitaxial films can be either fully strained or fully relaxed based on the choice of substrates. The Co dopants tend to segregate near the interface, but the size and distribution of the nanoclusters depend on the deposition parameters. Higher temperatures and slow growth rate lead to bigger cluster size and greater distance to the interface. The magnetic moments can reach 3.5 $\mu_B$/Co at room temperature, supported by the first-principles calculations considering spin-orbit coupling. Polarised neutron reflectometry measurement reveals that Co clusters and possible surrounding defects are the main magnetic sources.

The second part of this dissertation focuses on defect engineering in $WS_2$ and $MoS_2$. Both $WS_2$ annealed in reducing gas and Nd-doped $MoS_2$ show enhanced room-temperature ferromagnetism. The magnetic properties of the annealed $WS_2$ powders are governed by the sulfur vacancies, which significantly increase in density with increased annealing temperature. In the Nd-doped $MoS_2$ crystals, the exchange coupling of $Nd^{3+}$ ions and sulfur vacancies introduced by ion implantation can form magnetic polarons that determine the magnetic properties.

# Table of Contents

# Chapter 1 Introduction

## 1.1 Background

In semiconductor industry, the number of transistors in a dense integrated circuit is expected to increase twice in every two years. This is the famous Moore's law predicted by Gordon Moore. Moore's prediction has been proved accurate for several decades and served as a long-term guide in the semiconductor industry. However, the doubling has already started to falter in recent years due to unavoidable heat problem and other fundamental limits. The International Technology Roadmap for Semiconductors (ITRS) in 2016, also known as the final roadmap, has officially ended the long pursuit of Moore’s law. Next-generation semiconductor chips demand the development of novel semiconductor materials, especially in low dimensions. Diluted magnetic semiconductors (DMSs), which can combine semiconducting and magnetic properties in a single device, are of great importance and attract massive research interests.

In general, DMSs are semiconducting matrix materials doped with low-concentration transition or rare-earth metals. The dopants, such as Mn, Co, Fe and Gd, have uncompensated electron spins in partially occupied 3d or 4f orbitals and can induce long-range ferromagnetism into the matrix materials. The combination of semiconducting and magnetic properties leads to potential integration of logic semiconductors and magnetic information-storage capability in a single electric component. DMSs can be employed as critical component in spintronics, which manipulates the spin degrees of freedom of electrons, rather than mere charge degrees of freedom in traditional electronics. These devices possess potential advantages of higher integration density, higher processing speed, and lower power consumption.

To date, the most mature DMS system is Mn doped semiconductors, especially (Ga,Mn)As. (Ga,Mn)As has been extensively studied and is considered as the prototype DMS, providing textbook magnetic and thermodynamic properties. The methods used to fabricate (Ga,Mn)As and other DMS materials are usually in conditions far beyond thermal equilibrium, such as pulsed-laser deposition (PLD), molecular beam epitaxy (MBE), and sputtering. The induced ferromagnetism in (Ga,Mn)As is mediated by carriers (holes) and can be explained by mean-field Zener model. As the hole density in (Ga,Mn)As can be tuned via extrinsic means, such as electric field, light and strain, this provides researchers possible methods to manipulate the magnetic properties, including magnetization, Curie temperature and magnetic anisotropy, without changing temperature. Upon the successful modulation of the magnetic properties, spintronic devices like (Ga,Mn)As based memory cell have been designed and constructed. However, the low Curie temperature (~ 200 K) severely limits its potential applications.

Practical applications require DMSs materials with ferromagnetism persisted to above room temperature. Theoretical studies have predicted that room-temperature ferromagnetism is expected in some nitride and oxide systems, such as GaN and ZnO. This leads to massive research exploration in the following decade in the field of diluted magnetic semiconducting oxides (DMSO) and most research has been carried out on $TiO_2$ and ZnO. Co doped $TiO_2$ has demonstrated to be a remarkable DMS system with room-temperature ferromagnetism in both rutile and anatase forms in a variety of morphologies, such as thin films, nanoparticles, and nanorods. However, the origin of the ferromagnetism in the system has not been fully understood. In the meantime, there has been renewed interest in 2D transition metal dichalcogenides (TMDCs) due to their unique band structure, for example, spin-orbit splitting and inherently coupled spin and valley carriers.

## 1.2 Research objectives

A critical issue in Co doped $TiO_2$ is the puzzle relationship between growth conditions and Co distribution in $TiO_2$. Using similar techniques, segregation of Co, usually in the form of metallic nanoclusters, are observed in epitaxial thin films as often as homogeneously distributed Co atoms. The uncertainty of growth mechanism also leads to strong fluctuations in the magnetic properties. For instance, the magnetic moments observed in Co doped $TiO_2$ significantly from 2 to 0.01 $\mu_B$/Co reported by different research groups. In addition, the relatively high magnetic moment is only achieved by magnetometer measurement and there is no evidence to directly observe the high magnetic moment of the magnetic element and therefore, the mechanism for the high magnetic moment is still unclear. In this dissertation, 5% Co doped $TiO_2$ thin films were deposited on $LaAlO_3$ (001) and $SrTiO_3$ (001) substrate using a pulsed laser deposition system (PLD). With the delicate control of deposition parameters, we achieved the microstructure of metallic Co nanoclusters embedded in $TiO_2$ matrix with extremely high magnetic moment over 3.5 $\mu_B$/Co at room temperature. This result is striking since it is well-known that bulk Co has a magnetic moment of only 1.72 $\mu_B$/Co. We proposed the theory of confinement effect induced high magnetization of clusters. Moreover, from the fundamental science, it is challenging to achieve a large magnetization at high temperature. However, the thin film we prepared has a Curie temperature close to 1000 K. The embedded Co clusters are structurally, chemically and magnetically protected by the oxide matrix, enabling more stable magnetic properties. In addition, the structure and magnetic properties of the thin films can be controlled by tuning PLD growth parameters.

2D transition metal dichalcogenides (TMDs) have attracted wide interest due to many extraordinary properties and potential applications. $MoS_2$ and $WS_2$ are two common

TMD materials that have been extensively investigated. Especially, $MoS_2$ is almost the second most studied 2D material next to Graphene. Hence, in this thesis, the research is focused on $MoS_2$ and $WS_2$. Although pure low-dimensional $MoS_2$ and $WS_2$ have exhibited room temperature ferromagnetism due to vacancies or edge states, the magnetic study of TMDCs are still in its infantry and the manipulation of magnetic properties through doping and other defect engineering methods remain rarely explored. This dissertation aims to employ defects engineering to manipulate magnetic properties of TMD materials via heat treatment and ion implantation. It is revealed that defects can lead to the enhancement of room-temperature ferromagnetism and ferromagnetic properties are strongly associated with defect concentrations. Furthermore, during the investigation, we first discovered negative irreversible magnetization, usually observed in random field systems, in TMD materials.

The research outlines are shown below:

- To prepare 5 at% Co doped anatase epitaxial $TiO_2$ thin films on $LaAlO_3$ and $SrTiO_3$ (001) substrates via pulsed laser deposition and study the structure and magnetic properties of the thin films.
- To further prepare Co doped $TiO_2$ thin films under various conditions and study how deposition parameters affect films' structure and magnetism.
- To examine the vacancy defects and ferromagnetic ordering in $WS_2$ powders treated via annealing.
- To study the doping impact of Nd on the magnetic properties of $MoS_2$ crystals by ion implantation.

## 1.3 Thesis outline

This thesis consists of seven chapters. An overview of previous studies about diluted magnetic semiconductors and the objectives of this thesis are given in chapter 1. Chapter 2 presents a literature review about current development of spintronics and three flagship examples of diluted magnetic semiconductors. Chapter 3 gives a brief introduction of the methods used to fabricate and characterize the samples. Chapter 4 presents a detailed investigation on the microstructure and magnetic origin of PLD grown $TiO_2$ thin film doped with cobalt. Chapter 5 further explores the growth mechanism of $TiO_2$ thin film and the relationship between film structure and magnetic properties. Chapter 6 depict the modulation of magnetic properties in $WS_2$ powders and $MoS_2$ single crystals via annealing and ion implantation, respectively. Finally, a summary of the results and findings can be found in chapter 7.

# Chapter 2 Literature Review

## 2.1 Spintronics

Spintronics refers to an advanced electronic concept that mainly focuses on the intrinsic electron spin, magnetic moment and other associated physics phenomena. Spintronic devices utilize the unique spin degrees of freedom of electrons, rather than the charge degrees of freedom in traditional electronics. These devices possess potential advantages of higher integration density, higher processing speed, and lower power consumption [1]. In theory, ideal spintronic devices are operational even without applying an electric current, which unfortunately has not been accomplished yet.

The most successful industrial application of spintronics so far appears in the field of data storage, owing to the discovery of giant magnetoresistance (GMR) in multilayer thin films [2]. GMR is first unveiled in thin films made up of alternating metallic ferromagnetic and nonmagnetic layers. The electrical resistance of the thin films, dependent on the spin transport behaviors, is determined by the alignment of spins within the ferromagnetic layers. Later, a GMR-based device, spin valve, is demonstrated with a structure in which a nonmagnetic layer is sandwiched between two ferromagnetic layers [3]. Only one of the two ferromagnetic layers is spin free, while the other layer is pinned so its magnetization cannot be changed by an external magnetic field. The resistance of spin valve is controlled by the relative orientation of magnetizations in two ferromagnetic layers (parallel or antiparallel). The schematic diagram of a spin valve is shown in figure 2.1.

Read heads in hard disk drives were first benefited from GMR technology, enabling a significant improvement of the areal density. With the advantages of high sensitivity and large scale of integration, a wide range of applications have placed GMR devices as the

default magnetic sensors, such as integrated circuit (IC) current monitoring, automotive applications, non-destructive evaluation and biosensors for life science applications [4-7]. For instance, GMR effect can be used for biosensors by detecting the stray field of superparamagnetic nanoparticles attached to a target molecule hybridized to the specific proteins that are immobilized on the sensor surface [8].

Another major advanced application for GMR is magnetoresistive random-access memory (MRAM). For the past two decades, static RAM (SRAM), dynamic RAM (DRAM), and Flash have dominated the entire solid-state memory. While most SRAM applies six transistors in a flip-flop architecture, DRAM (volatile) and Flash (non-volatile) rely on stored electric charge. In contrast, MRAM utilizes the magnetic hysteresis associated with the ferromagnetic materials. The majority of current MRAM technologies are based on magnetic tunnel junction (MTJ) devices. Similar to spin valve, a typical MTJ also have two separated ferromagnetic layers, but the tunnel barrier between two layers is thin enough (< 2 nm) to let electrons pass through by quantum tunneling. The resistance of the device depends on the relative orientation of the magnetization in the free and fixed layers. For most materials, the resistance is lower when the two layers are aligned, similar to figure 2.1. To create an operational memory array, each memory cell consists of one MTJ which is grounded via a transistor. All current commercial MRAMs employ this architecture, known as 1-transistor-1-magnetic-tunnel-junction (1T-1MTJ) MRAM, as shown in figure 2.2 [9]. While the first generation of MRAM is field-switched, the second MRAM generation triggers magnetic switching by spin transfer torque (STT), enabling smaller MTJ devices for higher storage density. Recent STT-MRAM can achieve a high density of 4 Gb with compact cell structure (90 nm pitch) through optimizing parasitic resistance [10].

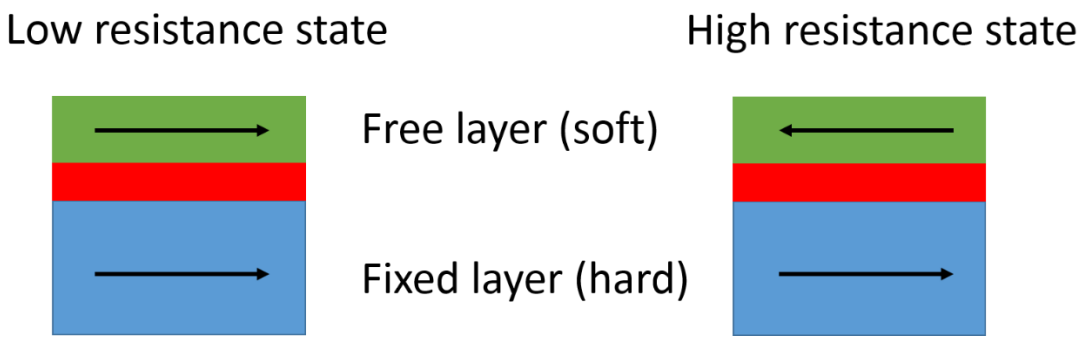


**Figure 2.1 A schematic diagram of a pseudo spin valve. The fixed and free layer are magnetically hard and soft, respectively. When the magnetic layers are aligned (left), the electrical resistance is lower than when they are antiparallel (right).**

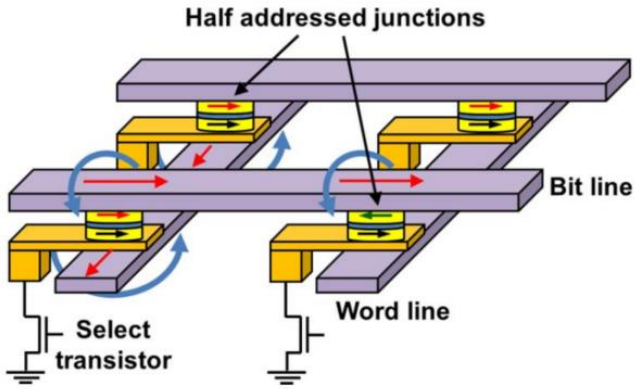


**Figure 2.2 A schematic diagram of an array of MRAM cells [9].**

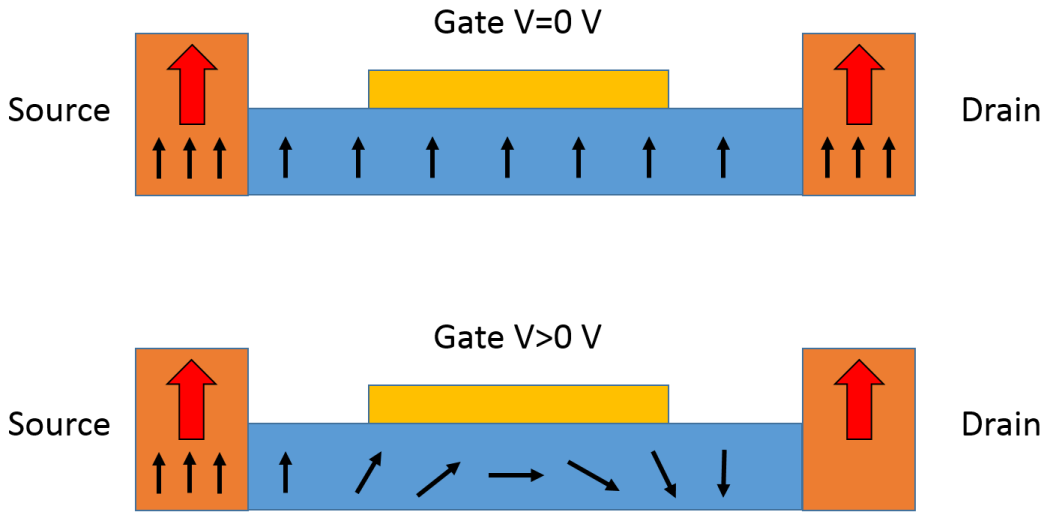


**Figure 2.3 A schematic diagram of a spin-FET device. Spin can only transport through semiconductor channel with zero gate voltage (on state). Applying a gate voltage blocks the spin current and turns the device off.**

The successful utilization of GMR has intrigued profound research interests in exploring spintronics with more complex structures and functionalities, such as spin-field effect

transistor (spin-FET), spin-light emitting diode (spin-LED) [11-14]. However, unlike GMR-based devices which have been quickly commercialized after the discovery, the realization of these spintronics at room temperature has not yet to be accomplished due to many unsolved problems. Take spin-FET as an example, the operation of the device follows three steps: spin injection through the source contact, spin transportation via the semiconductor channel, and spin detection from the drain contact. None of above steps have been perfectly solved so far and researchers around the world are still working toward improvement [15]. Figure 2.3 presents a conceptual structure of a spin-FET [16], which consists of two ferromagnetic contacts connected by a semiconductor channel. Electrons are polarized by the source contact and then injected into the channel. During the propagation, the spins precess due to spin-orbit interaction. The final current depends on the relative angle between the spin direction at the end of the channel and the magnetization direction of the drain contact. Since the spin direction at the end of the channel relies on the strength of the spin-orbit interaction in the channel, which can be modulated by external electric field, the current of the spin-FET can be controlled by gating.

## 2.2 Diluted magnetic semiconductors

Diluted magnetic semiconductors (DMS) can be served as a key material in spintronic devices. DMSs consist of a semiconducting matrix doped with a small percentage of magnetic impurities. The doping elements include transition and rare-earth metals (Mn, Co, Fe, Gd and Nd), which have uncompensated electron spins in the partially occupied 3d or 4f orbitals in the ground state. These dopants may induce magnetism into the semiconductors, leading to potential integration of logic semiconductors and magnetic information-storage capability in a single electric component. As the trend of

miniaturization of electronic products continues, such multifunctional elements with combined semiconducting and magnetic properties are of great importance. Moreover, DMSs provide a platform to the observation and investigation of a series of fundamental physics phenomena, such as tunneling anisotropic magnetoresistance, spin torque and spin Seebeck effect [17]. Figure 2.4 shows a simplified model of a DMS.

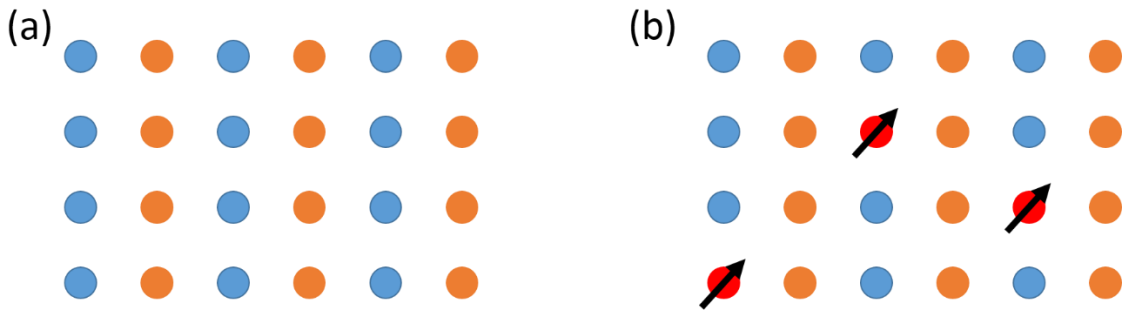


**Figure 2.4 A schematic diagram of (a) a pure nonmagnetic semiconductor and (b) a diluted magnetic semiconductor.**

According to the accumulated studies, most DMSs that support spontaneous polarization of spins can be divided into two categories. The first group is uniform DMSs, in which magnetically doped cations are randomly distributed within the semiconducting matrix. The most extensively investigated example in this group is Mn-doped III-V semiconductors. The spin-spin interactions in uniform DMSs are usually mediated by high concentration of carriers, either delocalized or weakly localized. The second class is heterogeneous DMSs, in which magnetic impurities are nonrandomly distributed. Magnetic dopants in these DMSs tend to aggregate in some particular nanoregions, such as interface or grain boundaries. To this class, it also exists a number of materials, in which magnetic properties are more related to various defects, rather than the doping regions. In both cases, the Curie temperature of heterogeneous DMSs appears obviously higher than uniform DMSs.

### 2.2.1 (Ga,Mn)As

Over the course of past decades, Mn-containing DMSs have been extensively investigated and related studies are the most mature. The flagship example is (Ga,Mn)As, which is widely considered as the prototype DMS, providing textbook magnetic and thermodynamic properties. GaAs is a mainstream semiconductor utilized in a variety of devices, including lasers and high-mobility transistors. As a consequence, (Ga,Mn)As holds great appeal if one can induce ferromagnetism by simply doping Mn into GaAs.

Generally, due to the low solubility of the magnetic dopants, dopants tend to aggregate and form dopant-rich nano compounds embedded in semiconducting matrix during the growth of DMSs at high temperatures. For instance, it was shown that at substrate temperature of 300-350 $^{o}$C, MnAs nanoclusters with size in the range of 30-50 nm and height around 2-5 nm can be observed on the surface of pre-deposited GaAs buffer layer [18]. For (Ga,Mn)As with high Mn concentration (5 at%), the formation of MnAs nanocrystals can be characterized by an sharp transition from 2D to 3D features in reflection high-energy electron diffraction (RHEED), whereas the transition is rather gradual for low Mn doped GaAs (1 at%). Consequently, the growth of (Ga,Mn)As is more preferred under lower substrate temperature in the range of 200-300 $^{o}$C and the approaches are commonly in the conditions far beyond thermal equilibrium, including pulsed-laser deposition (PLD), molecular beam epitaxy (MBE), and sputtering [19, 20].

More importantly, as the solubility of TM dopants in semiconductors is extremely low under thermal equilibrium, reducing the substrate temperature during epitaxy makes it possible to achieve ultra-high Mn concentrations (~10 at%). Another method to introduce a considerable density of doping elements is through ion implantation. In such cases, whether the high density of Mn ions can keep uniformly distributed in GaAs becomes a question. According to previous ab initio calculations [21, 22], a strong, short-range

attractive interaction is expected between the nearest Mn neighbors. This confirms the tendency for Mn dopants to aggregate into small nanoclusters and the requirement of sophisticated low-temperature non-equilibrium fabrication methods to limit or totally eliminate phase separation. A number of advanced characterization methods indicate that the formation of secendary phases can be indeed suppressed by low-temperature epitaxy process. According to a state-of-the-art laser-assisted wide angle 3D atom probe technique, Mn dopants are uniformly distributed in $Ga_{0.963}Mn_{0.037}As$ along both the in-plane and out-of-plane directions with 1 nm resolution [23]. This rules out the existence of large Mn aggregation inside GaAs or at the interface. However, the method cannot exclude the possibility of the formation of Mn dimmers or trimmers which are within the 1 nm resolution. In another study, high-resolution scanning tunneling microscopy (STM) was carried out to visualize electronic states of Mn dopants [24]. The STM images illustrate the wave functions of individual Mn dopant. Due to the unique topographic signatures, the figures not only show Mn dopants on the surface, but also those from the second and third subsurface layer. The result is in line with the fact that Mn ions can be uniformly distributed in (Ga,Mn)As without Mn aggregation.

In (Ga,Mn)As, Mn dopants substituted at Ga atom sites, serving both as acceptors and localized spins, the latter align with each other to give rise to long-range magnetic orderings. The valence state of Mn dopant in GaAs is $Mn^{2+}$ and the configuration of its outermost d-shell electrons is half-filled $d^5$ [25, 26]. The half-filled valence d shell attributes to a variety of magnetic behaviors, depending on the way of interactions between neighbouring Mn ions. Direct exchange occurs when electron wave-functions of neighbouring Mn ions directly overlap, whereas indirect exchange refers to interactions mediated by carriers in GaAs.

To date, a number of models have been proposed to solve the mystery of ferromagnetism in DMSs. The mean-field Zener model is the most widely accepted model for the ferromagnetism in (Ga,Mn)As. Zener proposed the original model in the 1950s to address the ferromagnetism in transition metals [27]. According to Zener, three types of spin coupling, the direct exchange between half-filled d shells of neighbouring atoms, the exchange between inner d electrons and conduction electrons, and the Fermi kinetic energy of the conduction electrons are responsible for the magnetic properties of transition metals. The relative magnitudes of these types of spin coupling decide the final magnetic behavior in a specific metal. Nearly 50 years later, Dietl *et al.* discovered that the model can be extend to DMSs with mean-field approximation [28, 29]. In the new model, the free energy density can be divided into two parts, one related to the mere Mn spins without any carriers and another describes the free energy density of the carriers surrounding the Mn spins. Equilibrium magnetization is solved by minimizing the function of the free energy density with respect to the magnetization at given temperature and magnetic field.

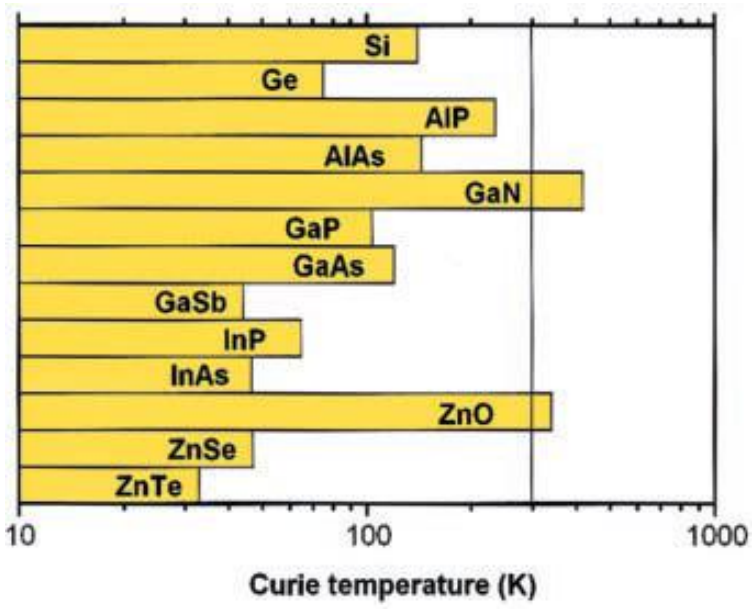


**Figure 2.5 Theoretical Tc values for a variety of 5 at% Mn doping p-type semiconductors with hole density of $3.5\times10^{20}/cm^3$ [30].**

The limitation of the mean-field Zener model mainly originates from thermodynamic magnetization fluctuations, antiferromagnetic interactions, Kondo effect, and effects of disorder and localization [28] [31-34]. These limitations can eventually lead to an accumulated error of at most 25 at% in theoretical Tc. The Curie temperatures of various DMSs evaluated by the mean-field Zener model are illustrated in figure 2.5 [30]. The simulated Curie temperature of 5 at% Mn doped GaAs with hole density of $3.5\times10^{20}/cm^3$ is ~120 K. Compared with experimental results, the calculation underestimates and overestimates the Tc value in low and high Ms range. It is also suggested by Zener modal that Curie temperature above room temperature can be achieved in (Ga,Mn)As containing 10 at% Mn in the absence of self-compensation. However, up to now the highest reported values, enhanced by post-annealing and nanostructure engineering, can only reach slightly above 200 K [35-38].

A key step towards the successful realization of spintronic devices is the manipulation of ferromagnetism in DMSs. As the hole density in (Ga,Mn)As can be tuned via extrinsic means, such as electric field and light, this provides us possible methods to manipulate the magnetic properties, including magnetization, Curie temperature and magnetic anisotropy, without changing temperature.

Gating, by applying an electric field to the semiconductor layer, is a highly mature technique in the semiconductor industry nowadays. For example, gating allows field-effect transistor (FET) to electrically switch between on and off states. Therefore, the possibility to turn on and off magnetic states through gating holds significant research interests since it is compatible with the existing commercial techniques. On early stage, a heterostructure consist of Mn doped GaAs and AlGaAs sandwiched by two GaAs layers was designed [39]. The heterostructure exhibits paramagnetic ground state due to low density of holes. By applying a negative gate bias, holes are electrostatically induced to

(Ga,Mn)As layer, resulting in a phase transition from paramagnetism to ferromagnetism. The operation temperature lays in the range of 100-117 K.

One big obstacle to modulate the magnetism in (Ga,Mn)As is the small modulation ratio. (Ga,Mn)As thin film has thickness dependent conductivity which transforms to an insulator with thickness thinner than 5 nm. However, employing thicker channel layer in order to lower conductivity is detrimental to the modulation ratio. One solution is adding a $Al_2O_3$ layer with high dielectric constant between (Ga,Mn)As and Au gate electrode. The modulation of magnetic anisotropy is evidenced by the observation of clear hysteresis loops at zero and negative electric field, while positive E leads to $\mu_0 H_c=0$ [40]. Similar control of magnetic properties can be accomplished by metal-insulator-semiconductor (MIS) structures with a conducting ferromagnetic (Ga,Mn)As channel [33, 41]. However, the change of Tc is limited around 20 K as the Fermi level is frequently pinned by gap surface states, even Tc itself can vary from 45 to 165 K over a wide range of (Ga,Mn)As thicknesses and Mn concentrations [42]. A electric double layer transistor structure, with a polymer electrolyte dropping on top of (Ga,Mn)As channel, was proposed to increase the range of Tc modulation, but the improvement is insignificant [42].

Polarized illumination provides another effective method to tune magnetic properties of (Ga,Mn)As. Circularly polarized light generates spin-polarized holes that change the orientation of Mn spins [43]. This light ellipticity dependent phenomenon creates a large magnetization variation up to 15% of Ms. A memorization effect is demonstrated by the remanent Hall resistance after illumination. In addition, the number of polarized holes required for magnetization switching by illumination is much less that via gating. Further study demonstrates a 90 degrees switching of magnetization can be realized in (Ga,Mn)As microbar though a scanning laser magneto-optical microscope [44].

Magnetic anisotropy is extremely sensitive to strain, which is often unavoidable in epitaxial thin film due to lattice mismatch between film and substrate. Therefore, the magnetic properties of (Ga,Mn)As can also be tuned via strain engineering. In core-shell nanowires, in which GaAs core is wrapped by MBE grown (Ga,Mn)As shell, easy axis is oriented along the nanowire axis [45]. The observed magnetic anisotropy is strain induced, similar to the lithographically patterned nanobars. In the case of nanobars, the easy axis can be rotated by 90 degrees via nanopatterning [46, 47].

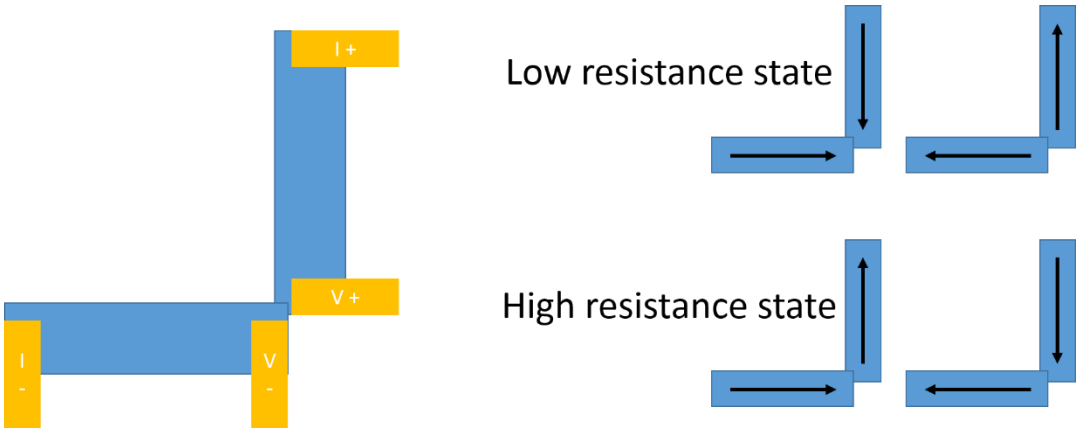


**Figure 2.6 A schematic diagram of (Ga,Mn)As nanobar based memory cell. The resistance of the memory cell is controlled by the relative orientations of two perpendicular (Ga,Mn)As nanobars.**

Upon the successful modulation of magnetic properties, spin injection, transportation and detection have been further investigated in (Ga,Mn)As based semiconductors [48-51]. By employing Esaki diodes with $p^+$-(Ga,Mn)As/$n^+$-GaAs structure as contacts, spin injection and detection can be accomplished in a single lateral semiconductor device [52]. Spin injection efficiency reaches ~50% under low bias currents, but higher bias can dramatically reduce the efficiency. The spin relaxation time of the device is ~4.3 ns. Based on the lithographically patterned nanobars discussed above, it is possible to design a prototype of (Ga,Mn)As based memory cell that operates in non-volatile regime [52-54]. The memory cell consists of two (Ga,Mn)As nanobars, electrically connected and perpendicular to each other. As the easy axis of nanobars is oriented along the long axis,

such structure can create different relative orientations of magnetization which can be set by writing process, as presented in figure 2.6. The reading is done through measuring the resistance depending on the relative orientations. Although the on/off ratio in the report is only 280%, much improvement is expected in future research.

### 2.2.2 (Ti,Co)$O_2$

Although Mn doped III-V DMSs provide perfect demonstrations for modulation of the magnetic properties in semiconductors, the Curie temperatures are generally below room temperature and the operation temperatures of correspondent devices drop even lower (< 50 K). Ferromagnetic ordering that can persist up to above room temperature is highly desirable for a vast number of applications. In the same paper in which Dietl calculated the Tc of 5 at% Mn doped GaAs, he also pointed out that some nitrides or oxides, such as GaN and ZnO, are possible to obtain a Tc above 300 K, as shown in figure 2.5. This leads to massive research exploration in the field of diluted magnetic semiconducting oxides (DMSO) and most research has been carried out focusing on two specific metal oxides, $TiO_2$ and ZnO [55].

Among several polymorphs of $TiO_2$, three exist in nature, namely rutile, anatase and brookite. Figure 2.7 shows the unit cells of rutile and anatase. Both rutile and anatase have a tetragonal crystal structure with wide indirect bandgaps of ~3 eV and rutile is thought to be more thermodynamically stable at high temperature. $TiO_2$ is definitely the most intensively investigated DMSO, due to a variety of well acknowledged interest properties or simply because it is the first DMSO reported to show ferromagnetism at room temperature.

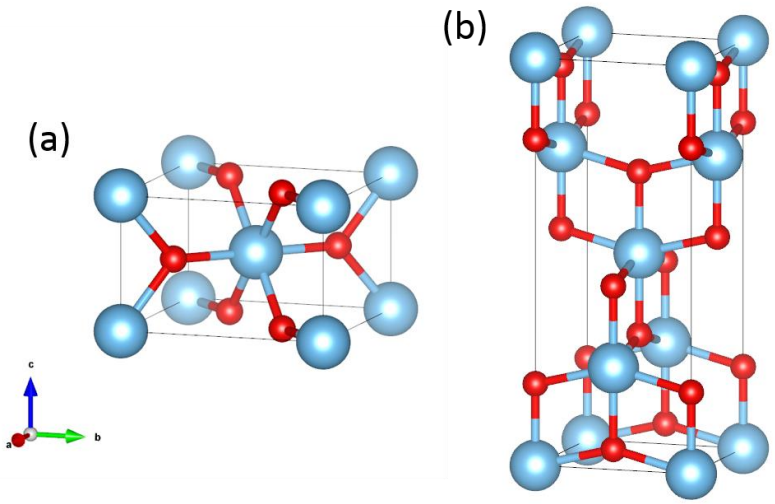


**Figure 2.7 Structure of $TiO_2$ polymorphs: (a) rutile and (b) anatase. Ti and O atoms are represented by blue and red balls.**

In the pioneering work published in journal Science in 2001 [56], Matsumoto *et al.* fabricated Co doped $TiO_2$ thin films, with cobalt concentrations between 0 and 8 at%, on $LaAlO_3$ (LAO) and $SrTiO_3$ (STO) substrates by the combinatorial laser MBE under oxygen pressure of $10^{-5}$-$10^{-6}$ Torr and temperatures of 950-1000 K. XRD result shows only anatase structure and no trace of segregation of impurities can be found in TEM images throughout the whole range of Co concentrations. Thus, the authors drew the conclusion that the distribution of Co in anatase was homogeneous. Long range ferromagnetic ordering was demonstrated by the magnetic domain structure of ~20 μm in diameter observed in magnetic force microscopy (MFM). Magnetic moment deduced from the Ms of $Ti_{1.93}Co_{0.07}O_2$ is 0.32 $\mu_B$ per Co atom, which is in agreement with the low spin state of Co ions. The Curie temperature is estimated to be at least higher than 400 K.

Following the work of Matsumoto's group, Co doped $TiO_2$, especially thin films, has been fabricated using a wide variety of techniques. Similar to the growth of (Ga,Mn)As, the majority of the fabrication methods are in conditions far beyond thermal equilibrium to achieve DMSOs with high dopant concentrations that exceed solubility limits, such as

laser MBE [56, 57], oxygen plasma assisted MBE [58, 59], reactive co-sputtering [60], and magnetron sputtering [61, 62]. However, these tremendous studies have failed to establish certain relationships between the growth conditions and the Co distribution in the thin films. In the epitaxial thin films, segregation of Co, in the form of metallic clusters, are observed as often as homogeneously distributed Co atoms.

The rather sensitive dependence of material structure on growth methods and conditions has raised fierce debate about the origin of observed ferromagnetism in Co-$TiO_2$. Is it intrinsic or extrinsic? The term diluted in DMS means dopant concentration should be diluted enough so that the distance between neighbouring dopants is mandatorily larger than the requirement for any conventional direct ferromagnetic exchange can take place. Thus, the intrinsic ferromagnetism in DMS can only be mediated through carrier. This is not a big issue in (Ga,Mn)As as Mn dopants are rather unlikely to form any secondary phases. However, in the case of Co-$TiO_2$, magnetic properties often originate from extrinsic effects such as metallic clusters or secondary phases. To distinguish intrinsic and extrinsic ferromagnetism, methods are carried out to measure unique phenomena caused by the interaction between dopant and carrier spins, such as optical magnetic circular dichroism (MCD), anomalous Hall effect (AHE), and etc. These characteristics can be regarded as the signature of intrinsic ferromagnetism, but real issues are often complex beyond expectations, which will be discussed later.

Toyosaki *et al.* reported anomalous Hall effect in laser MBE grown rutile $Ti_{1-x}Co_xO_{2-\delta}$ on r-sapphire substrates [57]. The oxygen vacancy density $\delta$ can be controlled by adjusting the partial oxygen pressure during deposition. The carrier density *n* determined from ordinary Hall effect varies from $10^{18}$ to $10^{22}$ $cm^{-3}$ with a rather stable mobility of ~$10^{-1}$ $cm^2V^{-1}s^{-1}$. The results show that the AHE resistance is dominant for lower magnetic field and develops with increasing carrier or oxygen deficiency concentrations. The authors

claimed the scaling behaviour of the $Ti_{1-x}Co_xO_{2-\delta}$ thin films is caused by a semiclassical nature of the charge carrier dynamics, which is not strongly affected by scattering from magnetic impurity, phonon and other defects. Later the temperature dependence of AHE in anatase $Ti_{1-x}Co_xO_{2-\delta}$ was studied over the range from 10 to 300 K [63]. While the anomalous Hall resistance and magnetization share the same magnetic field dependence, the former decreases at low temperature compared to nearly constant magnetization unaffected by temperature. Charge scattering may play an important role in AHE as its conductivity is proportional to the square of the mobility. Moreover, despite different conduction mechanisms, the scaling relationship between AHE conductivity $\sigma_{AHE}$ and conductivity $\sigma_{xx}$ follows the same rule of the rutile $Ti_{1-x}Co_xO_{2-\delta}$ discussed previously [57, 64]. In a subsequent study, the group expanded measuring temperature to 300-600 K [65]. The AHE resistivity shows clear ferromagnetic hysteresis loop up to 600 K with negligible change in the magnitude, suggesting a Curie temperature higher than 600 K.

In addition to anomalous Hall effect, magneto-optic properties were examined using PLD grown anatase $Ti_{1-x}Co_xO_2$ ($0 \leq x \leq 0.1$) on $LaSrAlO_4$ (001) substrates [66]. By controlling the partial oxygen pressure during deposition, the transport behaviour of the thin films varies from metallic, through semiconducting to insulating, suggesting successful modulation of carrier density *n*. Meanwhile, deposition at lower temperature leads to higher film conductivity. Magneto-optical circular dichroism (MCD) spectra show ferromagnetic response with a peak at the band edge. The MCD intensity is enhanced with the increase of either carrier concentration *n* or Co concentration x, indicating the essential role of the interaction between Co and carriers in the observed ferromagnetism. Subsequently, Toyosaki *et al.* also carried out MCD experiments on their laser MBE grown rutile $Ti_{1-x}Co_xO_{2-\delta}$ and made an effort to establish a direct link between MCD and AHE [67]. The MCD signal is trivial at low doping concentration $x \leq 0.1$, but for

$0.03 \leq x \leq 0.1$, intensity increases sharply in low magnetic field and quickly saturates in high magnetic field, showing obvious ferromagnetic behavior. The magnetic field dependency of the MCD and AHE resistivity for $Ti_{0.9}Co_{0.1}O_{2-\delta}$ shows unmistakable coincidence. The Hall resistivity and MCD represent the ferromagnetic response of the itinerant charge carriers and photoexcited carriers, respectively. Thus, a similarity of AHE and MCD results indicates the existence of a single ferromagnetic source, most probably the charge carriers induce the ferromagnetism.

In a more systematic study, massive data was summarized by Fukumura *et al.* to clarify the role of charge carriers for the room-temperature ferromagnetism in Co doped rutile $Ti_{1-x}Co_xO_{2-\delta}$ [68]. The results show clear dependence of Ms on both Co concentration and carrier density *n*. For instance, when Co concentration x=0.03, the magnetization is negligible at low carrier density $n=7\times10^{18}cm^{-3}$, but gradually increases with higher *n*. Clear ferromagnetic hysteresis loops can be observed for $n\geq2\times10^{20}$ $cm^{-3}$, while further increase in carrier density no longer improves Ms that is stabilized at ~1 $\mu_B$/Co. For a constant carrier density of $2\times10^{20}$ $cm^{-3}$, higher Co density leads to higher Ms. The Ms of $Ti_{1.95}Co_{0.05}O_{2-\delta}$ and $Ti_{0.9}Co_{0.1}O_{2-\delta}$ are approximately 1.1 and 1.5 $\mu_B$/Co. AHE resistivity and MCD of the Co doped rutile with different x and *n* show the same magnetic field dependence with Ms, indicating that the ferromagnetism is induced by charge carriers. The magnetic phase diagrams drew from the study suggest ferromagnetic ordering in Co doped $TiO_2$ is favored under higher Co concentration and carrier density, as shown in figure 2.8.

In addition to the above magnetic measurements, Fukumura *et al.* also evaluated electronic states of Co by XPS and XMCD. It is noted that Co ions are $Co^{2+}$ with high spin configuration, which is in agreement with several previous reports [69, 70]. The multiplet characteristics appeared in XMCD measurements at the Co $L_{2,3}$ edges on Co

doped rutile $TiO_2$ is claimed to originate from ferromagnetic $Co^{2+}$ ions coordinated by $O^{2-}$ ions [69]. In contrast, the XMCD of metallic Co is featureless. The multiplet feature matches the full atomic-multiplet calculation result of high-spin $Co^{2+}$ state in a crystal field with $D_{2h}$ symmetry, which is the local symmetry around the Ti site in rutile. This indicates $Co^{2+}$ ions substitute on Ti sites. However, the orbital and spin moments estimated from XMCD are only 0.013 and 0.12 $\mu_B$, respectively. The total magnetic moment (~0.13 $\mu_B$) is much smaller than that evaluated by magnetization measurement (~1 $\mu_B$) and the authors failed to explain the reason. The crystallographic position of Co in both rutile and anatase $TiO_2$ were further investigated by XRD utilizing anomalous scattering from K edge of Co [71]. Co should have the identical periodicity as the Ti ions in the lattice and generate a anomalous Bragg peak, if Co dopants are indeed substituting Ti site. However, unlike the results observed in Co-doped ZnO that support Co substitution, none of any anomaly was detected in Co doped rutile and anatase $TiO_2$, casting doubts on the exact whereabouts of Co in $TiO_2$.

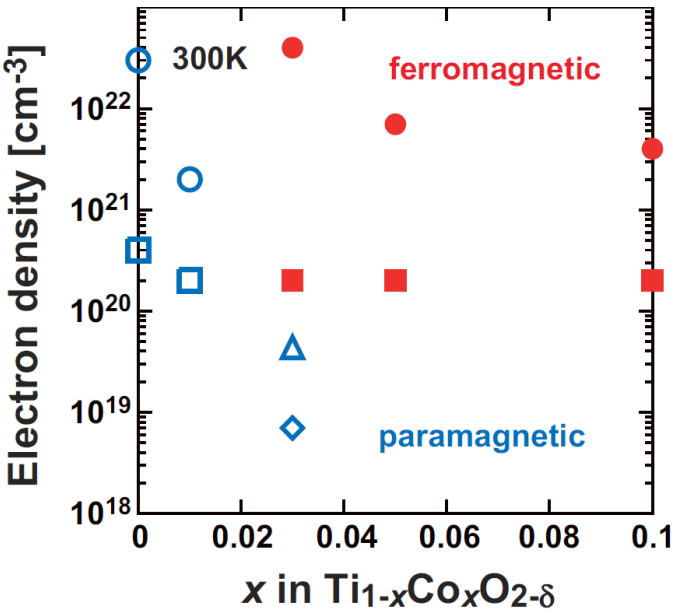


**Figure 2.8 Magnetic phase diagram for $Ti_{1-x}Co_xO_{2-\delta}$ as functions of x and *n* (measured at 300 K). Circle, square, triangle, and diamond symbols represent sample grown under partial oxygen pressure $P_{O2}=10^{-7}$, $10^{-6}$, $10^{-5}$, and $10^{-4}$ Torr, respectively [68].**

Are all the evidences mentioned above sufficient enough to prove the intrinsic nature of the ferromagnetism observed in Co doped $TiO_2$ systems? Unfortunately, the results failed to cease the considerable debate regarding the origin of ferromagnetism. The presence of nanosized cobalt clusters has been frequently observed by using similar or exactly same growth conditions [72, 73], making previous conclusions about intrinsic ferromagnetism suspicious. AFM, SEM and TEM are commonly used to identify the existence of Co nanoclusters, but their accuracy remains questionable. Under particular growth conditions, segregation of Co may only take place in particular regions, such as interface, surface and grain boundaries that avoid certain characterizations. In some extreme cases, conclusions are drawn too casually that only surface-sensitive probes like XPS were used, but Co may have different valence states in deeper regions compared to the surface. More strangely, post-annealing seems to be able to lead to opposite redistribution of Co dopants. While some believe annealing can dissolve Co nanoclusters and create $Co^{2+}$ ions [74, 75], others observed increased size of Co clusters, or precipitation of Co clusters on surface [72, 76]. The contradiction confirms the unreliability of judging Co states through mere STEM or XPS. Nevertheless, ferromagnetic orderings can be dramatically changed via annealing. For example, the Ms of 2 at% Co doped anatase $TiO_2$ increases from 0.3 to 1.1 $\mu_B$/Co after 450 $^oC$ annealing under ultra-high vacuum (< $10^{-8}$ Torr) [77].

Unfortunately, cobalt segregation is not the only possible source of extrinsic ferromagnetism. A number of magnetic contamination and instrumental artifacts can also generate ferromagnetic-like behaviours [78]. For example, any sample handling steps such as mounting and cleaning can accidentally contaminate the samples by forming magnetic compounds. Experiments must be treated carefully to minimize the contaminations.

To make things even worse, AHE was observed in rutile $TiO_2$ thin films with clear presence of 8-10 nm nanosized Co clusters at the interface [79]. The co-occurrence of AHE and superparamagnetism questions the employment of AHE as a signature of the intrinsic nature of the DMS. Although mere observation of AHE is not sufficient, some argue that the additional analysis of the magnitude of AHE and the comparison with theory may still be a reliable means.

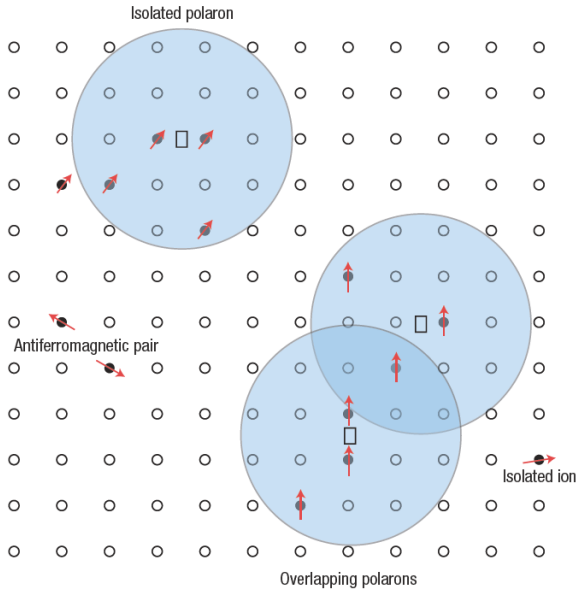


**Figure 2.9 A schematic diagram of magnetic polarons. Cation and unnoccupied oxygen sites are represented by small circles and squares, respectively [80].**

Due to the uncertainty of the dopant distribution, simulation of the Co-$TiO_2$ system using quantitative methods like the mean-field Zener model can be extremely inaccurate. Therefore, the system is often interpreted qualitatively and one of the most accepted models is bound magnetic polarons (BMPs) [80], as illustrated in figure 2.9. The concept was first proposed to explain the metal-insulator transition in EuO at low temperature [81]. In the BMPs model, defects like oxygen vacancies play the an important role, which not only donate electrons but also trap and bind the electrons to maintain insulating properties. The trapped electrons can couple and align the magnetic moments of the matrix, forming a bound polaron with a notable magnetic moment. The final magnetic

behaviour is determined by the interaction strength of neighbouring polarons. If the strength is strong, the material becomes ferromagnetic, while weak interaction can only leads to paramagnetic ordering [82, 83].

The ability to manipulate magnetism through gating is also considered as the most straightforward method to test the intrinsic ferromagnetism in DMSs. The first successful demonstration of modulation of ferromagnetism in Co doped anatase $TiO_2$ was done by Zhao's group [84]. A heterostructure consisting a bottom electrode $SrRuO_3$ layer (SRO), 7 at% Co doped $TiO_2$ layer, and a ferroelectric $PbZr_{0.2}Ti_{0.8}O_3$ (PZT) layer were deposited on $LaAlO_3$ substrate by PLD. The modulation effect both on Ms (15%) and coercivity (40%) were observed at room temperature. However, the mechanism explained by authors in terms of BMP remains obscure. The uniform distribution of Co dopants is suspicious as both Co concentration (7 at%) and growth temperature were very high (875 $^oC$) in the study, which frequently leads to Co segregation. The authors did not examine the issue carefully enough in the paper, but rather believed the result from the studies about post-annealing of Co-$TiO_2$ which have been proved doubtful. More recently, a electric double layer transistor (EDLT) was developed in pursuit of an extremely high electric field effect [85]. In contrast to conventional transistors, EDLTs use a liquid electrolyte instead of solid one. Under an electric field, ions within liquid electrolyte assemble to form a nanometer-thick electric double layer. This alters the transistor from a low-carrier paramagnetic state to a high-carrier ferromagnetic state. Figure 2.10 presents the concept of the EDLT.

To date, only a limited number of work about Co-$TiO_2$ based spintronic devices have been reported. Toyosaki *et al.* reported magnetic tunnel junctions composed of $Fe_{0.1}Co_{0.9}$ electrodes, $AlO_x$ tunnel barrier and ferromagnetic semiconducting $Ti_{1-x}Co_xO_{2-\delta}$ layer [86]. The resistance of the magnetic tunnel junctions exponentially increases with the barrier

thickness which can be controlled by stencil mask during the fabrication. The tunneling magnetoresistance and differential conductance in terms of bias voltage are extremely asymmetric at low temperature, which is probably caused by either degraded interface or asymmetric device structure.

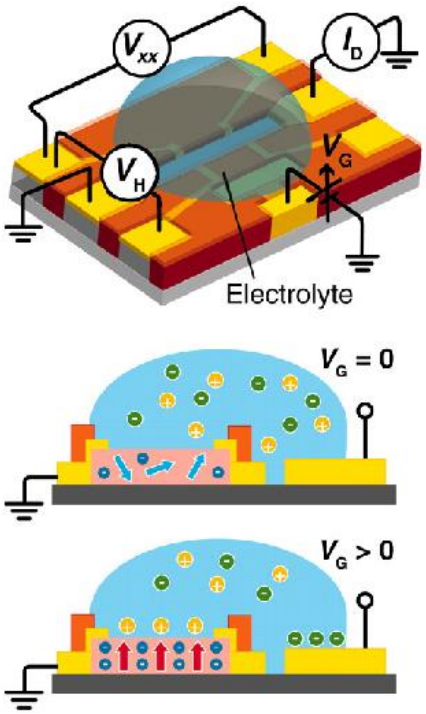


**Figure 2.10 A schematic diagram of EDLT. When gate voltage is zero, the transistor is in paramagnetic state as localized spins are randomly oriented. With a positive voltage applied, ferromagnetism is induced due to the accumulated eletron carriers on the channel surface [85].**

### 2.2.3 Transition metal dichalcogenides

While (Ga,Mn)As and (Ti,Co)$O_2$ based DMSs are under extensively exploration, scholars are still unceasingly searching for new kinds of semiconductors that are promising for spintronic applications. In 2004, graphene, a monolayer counterpart of graphite, was discovered and immediately attracted considerable research interest. Although at the moment graphene is still the most notable two-dimensional material, its zero bandgap restricts the potential applications in logical devices. Inspired by graphene, there has been renewed interest in graphene-like semiconductors, which have layered structure but with

atomic thickness, such as boron nitride, transition metal dichalcogenides (TMDCs), and transition metal oxides (TMOs).

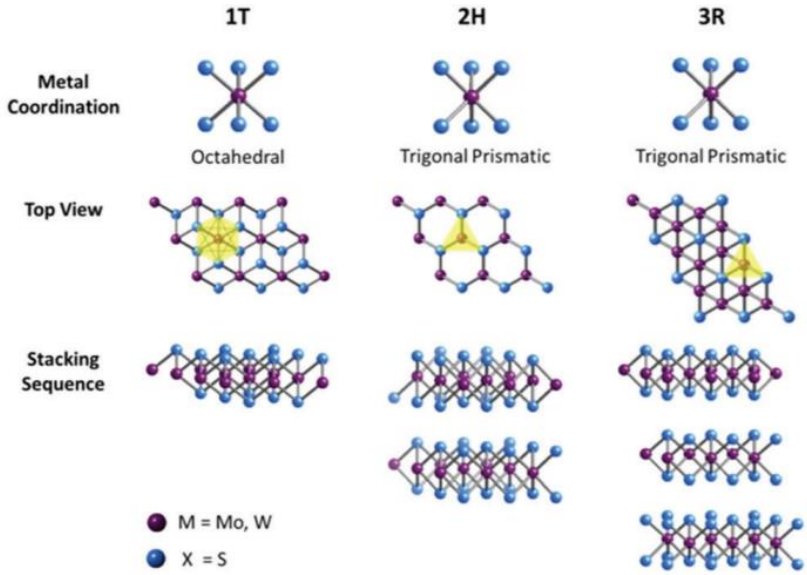


**Figure 2.10 Structure of 1T, 2H and 3R $MoS_2$ and $WS_2$ unit cells [87].**

TMDCs are a group of chemicals sharing a formula $MX_2$, in which M and X represent a transition metal and a chalcogen, respectively. Depending on the combination of different M and X, the TMDC family has more than 40 distinct members. $MoS_2$ and $WS_2$ are two most thoroughly studied TMDCs, especially for $MoS_2$, which is the only TMDC naturally existing in massive quantities. Both $MoS_2$ and $WS_2$ have sandwich-like layered structure. In each $MoS_2$ layer, a hexagonal plane of Mo atoms is sandwiched by two planes of S atoms. Like graphene, two neighboring $MoS_2$ layers are only connected by a weak van der Waals force, making it possible to obtain monolayer materials through exfoliation. Based on the type of Mo coordinations and stacking order of $MoS_2$ layers, three polymorphs of are $MoS_2$ commonly observed: 1T, 2H and 3R. The numbers refer to the number of $MoS_2$ layers in a primitive cell and the letters are abbreviations for the lattice symmetry (tetragonal, hexagonal and rhombohedral). Figure 2.10 shows the unit cell structures of three polymorphs.

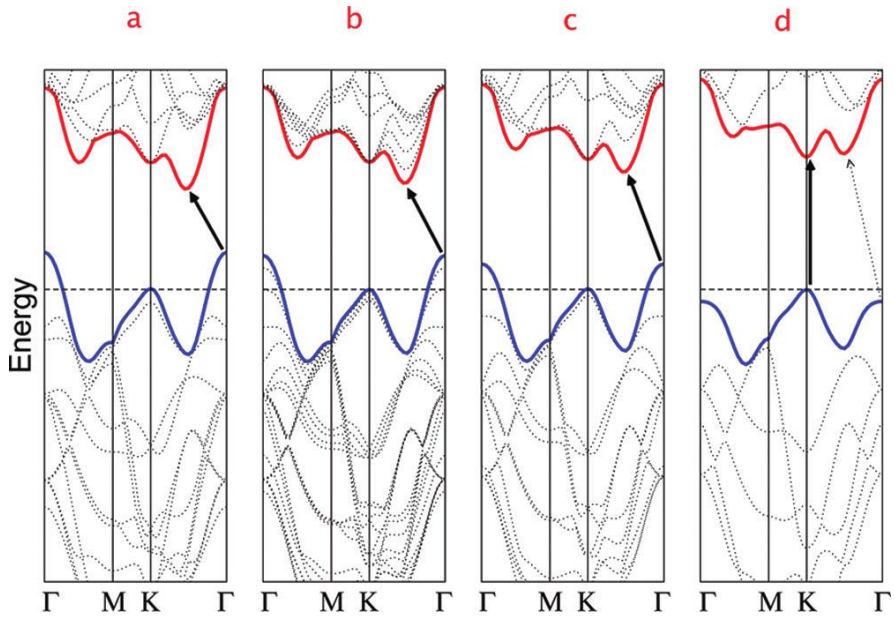


**Figure 2.12 The evolution of the band structure of $MoS_2$: (a) bulk, (b) four-layer, (c) bilayer, and (d) monolayer $MoS_2$ [88].**

One of the most intriguing features of 2D $MoS_2$ and $WS_2$ is the thickness-dependent band structure. For example, bulk $MoS_2$ has an initial indirect bandgap of 1.2 eV, which gradually increases with decreased layer number. However, an abrupt transition to direct bandgap occurs for monolayer $MoS_2$, with a much larger bandgap (~1.9 eV) located in the visible frequency region, as shown in figure 2.12. In addition to the direct bandgap, another significant property of monolayer $MoS_2$ and $WS_2$ is spin-orbit splitting. Due to the broken inversion symmetry, the band structure of monolayer $MoS_2$ at the top of valence band (TVB) splits into spin-up and spin-down bands with energy difference of 140-150 meV. The value is slightly bigger for $WS_2$ as W is heavier than Mo. More importantly, as a result of time-reversal symmetry, the splitting in opposite valleys must have opposite directions, indicating that the spin and valley carriers are inherently coupled. The modulation of the coupled spin and valley carries is the foundation of TMDC based spintronics and valleytronics.

Most methods used to fabricate graphene can be employed to 2D TMDCs with parallel effectiveness. The methods can be divided into two categories, top-down methods like

mechanical or chemical exfoliation [89-91], and bottom-up methods like chemical solution deposition or chemical vapor deposition (CVD) [92-97]. The simplest approach to obtain 2D TMDCs is through repeated cleavage, from initial bulk crystal to final few-layer or even monolayer TMDCs, by using scotch tapes. In general, mechanical exfoliation produce best single crystalline nanosheets with high purity and surface cleanliness, which are favorable for the evaluation of fundamental properties. For example, mobility is often used to evaluate the quality of monolayer $MoS_2$ as various defects can considerably reduce the value. Based on a large number of experimental work, mechanical exfoliated $MoS_2$ exhibit the most superior mobility of several tens of $cm^2/Vs$ [98-101]. Meanwhile, liquid-phase exfoliation can yield large quantity of TMD nanosheets. Using proper solvent such as N-methyl-pyrrolidinone (NMP), exfoliation of bulk $MoS_2$ to few-layer or monolayer nanosheets can be realized by one-step sonication [89]. Although the quality is usually low compared to mechanical exfoliation, it is extremely suitable for the applications that high crystallinity is not necessarily required and shape of the product has little impact on the performance, such as hydrogen evolution reaction, lithium ion batteries and supercapacitors [102, 103]. Li ion intercalation can dramatically increase the effectiveness of liquid-phase exfoliation process because sonication produces large microsheets as well as nanosheets and the yield of few-layer TMDCs is low [104]. More intriguing, Li ion intercalation causes a phase transition of $MoS_2$ from 2H phase to 1T phase. The two phases can coexist to form monolayer $MoS_2$ heterostructures [105]. Hydrothermal method, another approach often used for massive production, can also prompt the phase transition. With 1T phase occupies 25%, the density of electron carriers can increase by an order, leading to an intrinsic ferromagnetic response of 0.25 $\mu_B$ per Mo atom [106].

Defects can significantly modify the electronic and magnetic properties of single and few-layer $MoS_2$. All kinds of defects have been studied by first-principles calculations, including vacancies, interstitials, antisites and adatoms [107-111]. It is noted that S vacancies are the most easily formed and abundant defects in $MoS_2$. Although all theoretical studies predicted ideal $MoS_2$ crystal has a nonmagnetic ground state, $MoS_2$ nanosheets prepared through a variety of methods frequently display clear ferromagnetic behaviours at room temperature, in contrast to bulk $MoS_2$ which only shows diamagnetism as simulations predict. Gao *et al.* prepared $MoS_2$ nanosheets via liquid-phase exfoliation by sonicating $MoS_2$ powders in N,N-dimethylformamide (DMF) [112]. The size of the nanosheets can be tuned by the ultrasonic time. Higher Ms is obtained by smaller nanosheets and 10 h sonicated sample has a Ms of $1.1\times10^{-3}$ emu/g at room temperature. Larger Ms is shown by CVD prepared $MoS_2$ and $WS_2$ nanosheets [113]. $MoO_3$ and $WCl_6$ were used as precursors as Mo and W source. The Ms of $MoS_2$ decreases from 1.08 emu/g at 10 K to 0.55 emu/g at 623 K, while the Ms of $WS_2$ is a bit lower. The ferromagnetic ordering persists to 865 and 820 K for $MoS_2$ and $WS_2$, respectively.

In spite of the fact that room-temperature ferromagnetism of TMDs has been observed in a large number of experimental studies, the understanding of its origin remains puzzled for researchers. Since bulk $MoS_2$ is pure diamagnetic, the ferromagnetism observed in $MoS_2$ nanosheets is absolutely attributed to defects. To date, the ferromagnetism is generally interpreted by two types of defects, vacancies and zigzag edges [112, 114, 115]. However, most vacancies, including $V_S$ (monosulfur vacancy), are non-magnetic. According to theoretical studies, only a few vacancy complexes, such as $V_{MoS2}$ ($MoS_2$ triple vacancy), can contribute to ferromagnetic orderings. On the other hand, simulation of $MoS_2$ zigzag nanoribbons indicates the magnetic moment decreases with enlarged width. When the ribbon is 6.43 nm wide, the value is only 0.037 $\mu_B$ per $MoS_2$ [116],

which can be totally ignored since the size of nanosheets are much larger than several nanometres. Compared to zigzag edges, grain boundaries, another type of 1D defects, are more ubiquitous in TMDs. Recent first-principles studies suggest that dislocations or formation of antisite defects on $MoS_2$ grain boundaries can create a magnetic moment around 1 $\mu_B$ [117, 118].

Although vacancies and grain boundaries can theoretically introduce ferromagnetism into TMDCs, engineering of intrinsic defects has a number of drawbacks. First and foremost, it is next to impossible to experimentally evaluate the existence of the vacancies or grain boundaries in the material. Based on the first-principles calculations, ferromagnetism can only be caused by a few types of intrinsic defects, but the generation of these intrinsic defects is always accompanied by a bunch of other defects. For example, at least four types of vacancies and two types of antisites were observed in CVD grown monolayer $MoS_2$, but none of them can contribute to ferromagnetic orderings [119]. In contrast, magnetic doping already have mature techniques such as MBE and ion implantation that can achieve desired ionic substitutions with precise concentrations. Secondly, intrinsic defects usually have low magnetic moments less than 1 $\mu_B$/defect, while the magnetic moments of transition or rare earth metals can easily exceed 3 $\mu_B$/ion. Thus, high magnetization can be expected from magnetic doping. In addition, magnetic doping in 2D TMDCs has several advantages compared to DMS based on II-VI or III-V semiconductors. Generally, the single crystal quality is very high for 2D materials, so the defects in 2D materials can be more easily controlled by laser treatment, ion implantation and fabrication methods. Clustering or secondary phases are frequently observed and usually located in the interface between the thin film and substrate, destroying the intrinsic ferromagnetism in DMSs. For the magnetic dopants in TMDCs, the 2D nature of the thin film can avoid the formation of clusters or secondary phases.

Substitution of Mo atoms with transition and rare-earth metals has been investigated by a great number of research groups using first-principles calculations [120, 121]. Cheng *et al.* carried out a systematic simulation of 27 different transition metals and found that Fe, Co, Mn, Zn, Cd, and Hg doped monolayer $MoS_2$ are ferromagnetic [122]. Although some transition metals may not have direct contribution to magnetic moments, the result changes if they combine surrounding S vacancies to form a complex defect. For example, in V doped monolayer $MoS_2$, a V atom coupled a nearby S vacancy has a formation energy of 5.89 eV and can create a magnetic moment of ~ 1 $\mu_B$ [123]. Experimentally, either anions or cations in TMDCs can be easily substituted by elements from the same group. The alloys, such as $Mo_{1-x}W_xS_2$ and $MoS_{2x}Se_{2(1-x)}$, can be prepared by CVD with simply mixing two precursors together [124, 125]. However, substitutional doping of other transition metals has been proved to be far more difficult [102, 126]. In bilayer Co-doped $MoS_2$ nanosheets grown by CVD, Co is only observed at the edge of the nanosheets [127]. Further increase deposition temperature from 680 to 750 $^oC$ leads to growth of $CoS_2$ layer on top of the $MoS_2$ nanosheets. In another study, it took more than 500 hours to prepared Nb-doped $MoS_2$ nanosheets by a chemical vapour transport method, but the concentration of Nb dopants could only achieve 0.5 at% [128].

2D TMDCs have great potential in applications of spintronics and valleytronics. Wang *et al.* designed first $MoS_2$ based spin valve by using monolayer $MoS_2$ and Permalloy (Py) as the nonmagnetic spacer layer and ferromagnetic layers [129]. However, due to strong hybridization with Ni and Fe atoms, the $MoS_2$ layer behaves more like conducting film rather than tunnel barrier. The magnetoresistance is very low, only 0.73% at 10 K. Further first-principles calculation indicates the value can reach 9% for a perfect Py/$MoS_2$/Py junction, suggesting much space for improvement.

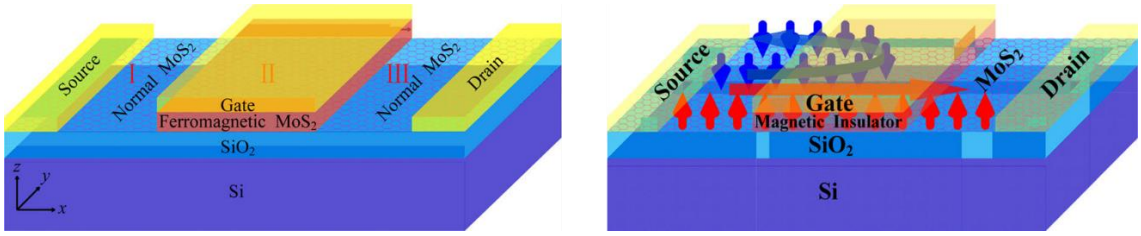


**Figure 2.13 The conceptual structure of an all $MoS_2$ junction (left) and its operation principle (right) [130].**

Most current research concerning 2D TMDCs related spintronics are based on non-magnetic channel material, since the magnetic modulation of 2D TMDCs is still in its infancy. Li *et al.* theoretically proposed a junction structure that consists of a ferromagnetic $MoS_2$ layer sandwiched between two normal non-magnetic monolayer $MoS_2$ [130], as shown in figure 2.13. By applying a gate voltage, not only can the charge transport be manipulated, but also fully valley- and spin-polarized conductance can be simultaneously obtained with tunable amplitude and direction. A two-dimensional spin field-effect switch was experimentally demonstrated based on a $MoS_2$/graphene heterostructure [131]. The spin current in the graphene channel can be electrically switched by adjusting the spin absorption into the $MoS_2$ layer. The device can be operative at temperatures up to 200 K.

# Chapter 3 Experimental Methods

## 3.1 Material fabrication

### 3.1.1 Pulsed laser deposition

Pulsed laser deposition (PLD) is a type of physical vapor deposition (PVD) techniques. The concept of PLD is schematically illustrated in figure 3.1. A pulsed high-energy laser beam is focused through a set of optical apparatuses onto the surface of a target which is usually placed at an angle of 45$^{o}$ to the incident beam. After absorbing the laser energy, the target ejects a tiny amount of material in the form of a plume due to superheating. The plasma then accumulates on a substrate facing the target. During deposition, the chamber can maintain at ultra high vacuum below $10^{-8}$ torr or fill with certain background gas. In our case, oxygen is used to deposit $TiO_2$ thin films.

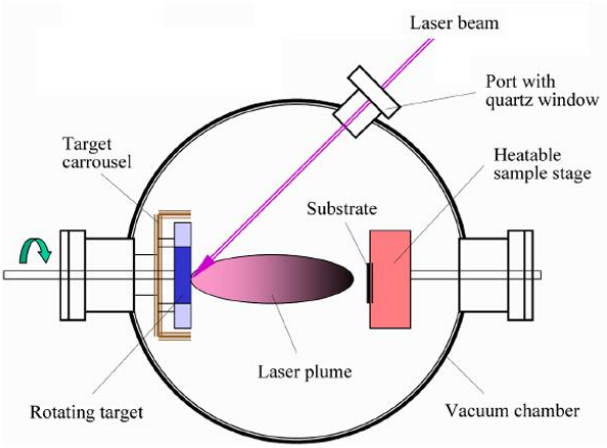


**Figure 3.1 A schematic diagram of a PLD system.**

While the basic concept is relatively simple, the physical mechanisms behind laser-target interaction and film growth are extremely complicated. The PLD process is generally modelled by Monte Carlo simulation [132], which consists of three crucial steps, including laser absorption and ablation of the target material, creation and dynamic of the plasma, and nucleation and film growth on the substrate.

The typical energy density and duration of a single laser pulse in PLD is approximately 1 J/cm$^2$ and 10 ns, leading to an instantaneous power density above $10^8$ W/cm$^2$. The laser energy is then converted into heat and conducted into the target. During the thermal diffusion, the temperature in the target surface can rise at a rate as high as $10^{11}$ K/s that generates a gas pressure of 10-500 atm, leading to the vaporization of the target material in an extremely non-equilibrium state. The characteristic ablation plasma, or plume, is caused by multiphoton ionization of the material gas.

In the second step, the plume expands in the direction perpendicular to the target surface towards the substrate, as illustrated in figure 3.1. The composition of the plume is considerably complex, containing both stable and metastable species such as electrons, atoms, ions, molecules, clusters, particulates, and molten globules, with high kinetic energies in the range of 1-500 eV [133]. The spatial distribution of the plume is determined by the chamber pressure. For example, narrow shaped plume with no scattering with background gas only occurs at high vacuum. In general, the distribution of the plume is beamlike, leading to a restricted deposition area of only a few cm$^2$. The difficulty to accomplish large area deposition is commonly claimed as a drawback of PLD. However, if the substrate is not fixed but repeatedly rastered across the path of the plume, the problem can be solved and even turn to advantage [134].

When the plume reaches the substrate, some target atoms are sputtered out from the surface and further collide with the plume to form a condensed collision region, where the gas is supersaturated [135]. Afterwards, nucleation and coalescence of nuclei give rise to different thin film growth modes [136], as illustrated in figure 3.2. When the nuclei are strongly bound to the substrate, the deposition materials first grow into a single-layer film before the nucleation and growth of the second layer. This is called layer-by-layer growth mode. On the other hand, island growth mode occurs when the interatomic bonds within

the deposition material dominate. In such case, the nuclei continue to grow in three dimensions to form large islands. The last layer plus island growth mode starts with layer by layer deposition and transits to island mode during deposition. A number of parameters have critical influence over the nucleation process and growth kinetics, including laser fluence, pulse interval, substrate surface and temperature, background gas and pressure, and distance between target and substrate.

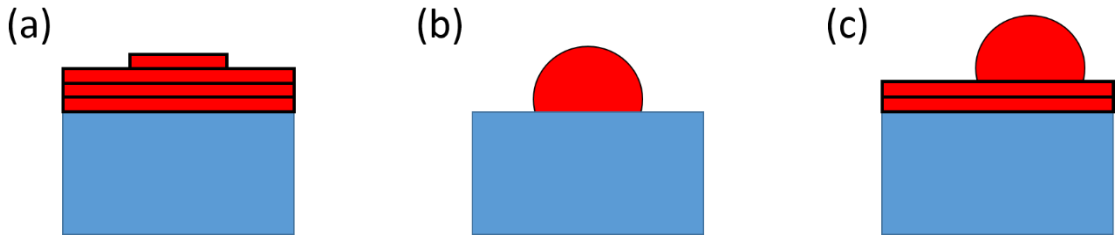


**Figure 3.2 Schematic diagrams of three modes of thin film growth: (a) layer-by-layer mode, (b) island mode and (c) layer plus island mode.**

In summary, PLD is a powerful technique and exhibits many practical advantages. Firstly, unlike other PVD methods such as thermal and e-beam evaporation, the energy source in PLD is located outside the vacuum chamber. This prevents contamination from the source and provides much more flexibility in equipment design. Secondly, owing to the ultra-high temperature in the laser focus area, almost any condensed matter material can be melt and ablated. Moreover, the stoichiometry of the thin film can be controlled with extreme accuracy. Finally, it is convenient with the ability to control film growth rate and thickness by merely changing the pulse repetition rate while keeping the energy input. However, PLD technique has a major drawback. Particulates with size as large as a few micrometers, or labelled as laser droplets, are inevitably generated during the laser irradiation, which can seriously affect the growth and final quality of the thin film. New techniques aiming to effectively block the laser droplets are still under development. In this work, the PLD was performed in Australian National Fabrication Facility (ANFF) at UNSW.

### 3.1.2 Ion implantation

Ion implantation is a low-temperature technique to dope an element into a target material. The dopant atoms are first generated by heating an ion source, then electrostatically accelerated and directed at a target chamber after separating by the mass-to-charge ratios. The total amount of dopant implanted in the target, which is called the dose, can be calculated by integral of the ion current over time. The ion energies applied in implantation typically range from 10 to 500 keV. If shallow implantation of only a few nanometers are required, energies in the range of 1 to 10 keV can be used. Energies lower than 1 keV only lead to ion beam deposition rather than implantation. On the other hand, energies of several million electron volts can also be used but may cause severe damage to the lattice structure of the target.

After entering the target lattice, the ions gradually lose energy accompanied by a series of collisions with the target atoms and finally stop at some depth within the target. This process is called ion stopping, influenced by both nuclei and electrons. While nuclear stopping can be described by classical kinematics, the modelling of electronic stopping is quite complex. The energy loss by the the interaction between the implanted ions and the electrons is believed to dissipate into thermal vibrations of host atoms through the electron cloud. Although each implanted ion travels though the target by a random path, the ion trajectories can be solved by a statistical method. The distribution is often simplified as a Gaussian. In addition, annealing is usually required to repair the structure damage and move dopants from interstitial to substitutional sites, where dopants can be electrically activated.

In this work, the ion implantation was carried out using the low-energy ion implanter at GNS Science, New Zealand.

## 3.2 Material characterisation

### 3.2.1 X-ray diffraction

X-ray diffraction (XRD) is one of the most significant techniques in material analysis because it can determine the atomic and molecular structure of a crystal [137]. X-rays are a form of electromagnetic radiation and the diffraction is based on Thomson scattering. When a beam of X-rays hits a material, its propagation can be modified by the electrons in the material while the kinetic energy, or wavelength, is conserved. If the material is a crystal, the incident X-rays is diffracted into certain directions based on the crystalline structure. The density of electrons within the three-dimensional crystal can be calculated from the angles and intensities of the diffracted beams. Further analysis can obtain more crystal information, such as the positions of the atoms, grain size, strain, and etc.

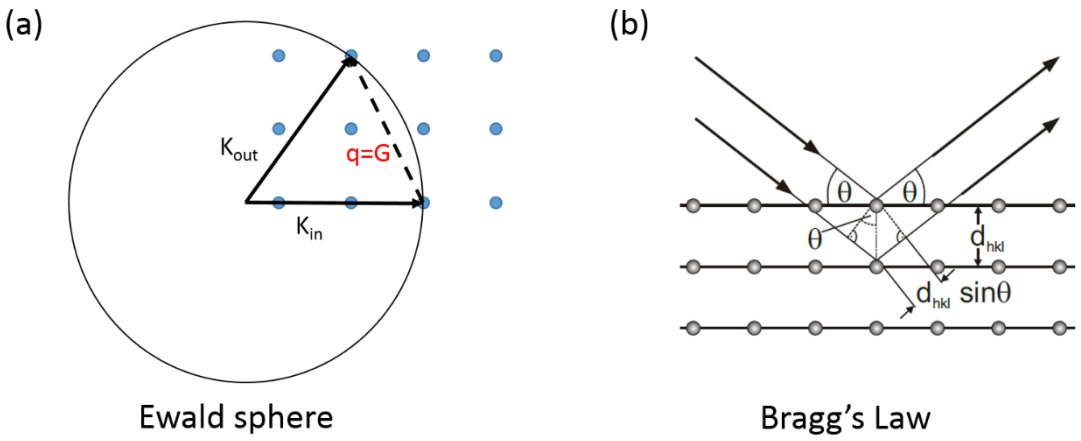


**Figure 3.3 (a) The geometric construction of Ewald sphere. (b) Interpretation of the Bragg equation.**

The diffraction of X-rays follows the rule $q=K_{out}-K_{in}=G$, in which $K_{out}$ and $K_{in}$ are wave vectors of diffracted and incident X-rays, and G is a reciprocal lattice vector. This condition is illustrated in figure 3.3(a), in which all the possible G are located with a sphere. The so called Ewald sphere has a diameter of $2|K|=4\pi/\lambda$. Assuming $G=nG_{hkl}$, one can eventually obtain the famous Bragg's Law $n\lambda=2d_{hkl}\sin\theta$, where the angle between $K_{in}$

and $K_{out}$ is 2θ. The Bragg equation is usually interpreted by a simple way, as shown in figure 3.3(b). The incident X-rays are reflected by lattice planes (hkl). The diffraction only occurs when the path difference of waves reflected by two neighbouring planes is equal to an integer multiple (n) of the wavelength.

A basic X-ray diffractometer consists of three elements: an X-ray tube, a sample holder, and an X-ray detector. In the X-ray tube, X-rays are generated by heating a filament to produce electrons and then bombarding a target (Cu, Fe, Mo, Cr) with electrons. Cu is the most common target material for X-ray diffraction, with $\lambda(K_\alpha)$=1.5418 Å. The X-ray generator and detector are located on the circumference of a graduated circle centred on the sample, as shown in figure 3.4(a). In some diffractometers, the sample holder can be rotated around three axes respectively (figure 3.4(b)), enabling a wide range of XRD scan modes. In the most commonly used θ/2θ scan, the geometry of the diffractometer, also known as Bragg-Brentanno geometry, is that the rotation of the sample (ω/θ) equals to a half of the rotation of the detector (2θ). Another example is **Ω** scan, also called rocking curve, in which sample is slightly rotated around the ω-axis while both generator and detector are fixed.

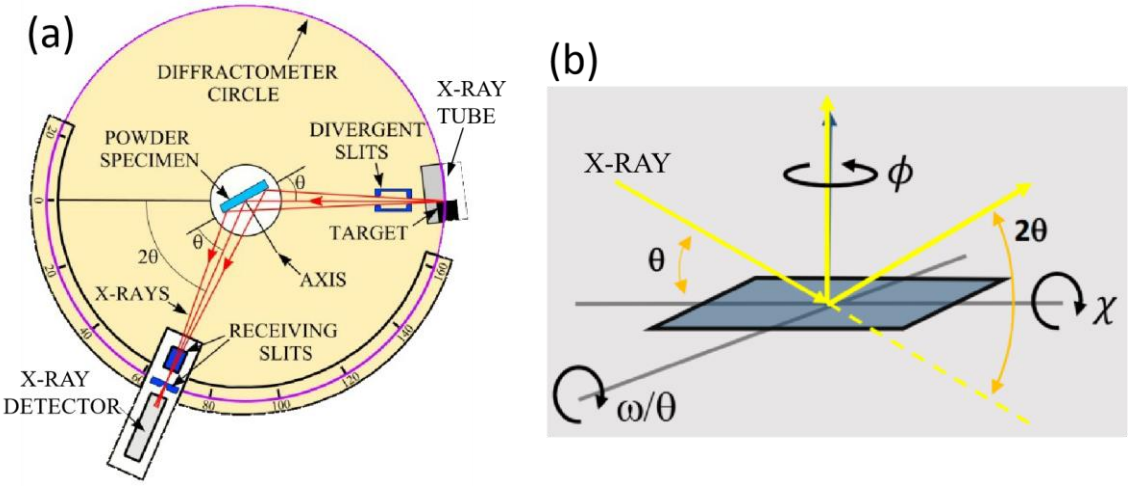


**Figure 3.4 (a) A schematic diagram of an X-ray diffractometer. (b) Rotation axes of the sample holder.**

The XRD data can be analyzed quantitatively. Rietveld refinement is a computational technique which compares the experimental data to a simulated diffraction profile. The Rietveld method employs a least squares based minimization algorithm. A variety of structural parameters of crystalline materials can be refined through the approach, including unit cell dimensions, preferred orientation, scale factors, etc.

In this work, Empyrean (PANalytical) Thin-Film X-ray Diffraction System and PANalytical Xpert Multipurpose X-ray Diffraction System was used for the phase identification of thin film and powder samples. X-rays are generated by the collision of high velocity electrons on a Cu target and then filtered to a monochromatic Cu $K_\alpha$ beam. The photon energy and wavelength of Cu Kα line are 8.05 keV and 0.154 nm, respectively. The minimum step size is $0.013^o$. Data analysis was accomplished by X'pert HighScore Plus software with a built-in Rietveld refinement package.

### 3.2.2 Scanning electron microscopy

A scanning electron microscope (SEM) is a type of electron microscope, which produces various signals containing information about the topography and composition of the sample surface [138]. When a focused electron beam, with a tunable acceleration voltage of 5-30 keV, stikes on a sample, the energy exchange between the electron beam and the sample results in a variety of electron scattering and radiation, such auger, secondary and backscattered electrons.

In most cases, we are interested in collecting and capturing images of secondary electrons that are emitted from very top of the sample surface. Secondary electrons are extremely surface sensitive and can produce high-resolution images of the sample surface. In addition to secondary electrons, the energy of characteristic X-rays are often measured by Energy-dispersive X-ray spectroscopy (EDX) to identify elements in the sample and

map the distribution. In this work, FEI Nova NanoSEM 450 was used to analyze the surface morphology of samples. The voltage of electron beam was set to 5 keV for high-resolution imaging and 20 keV for element identification.

### 3.2.3 Transmission electron microscopy

When a sample is thin enough (less than 100 nm), the beam of electrons interacted with the sample can transmit through it to form an image [139]. In a transmission electron microscope (TEM), the image is then magnified and focused onto a screen, either a fluorescent or a liquid-crystal display one. The major advantage of SEM and TEM over light microscopes is the ability to view samples at a considerably high resolution. This is attributed to the much shorter de Broglie wavelength of electrons (2.5 pm at 200 keV), especially in TEM where electrons are accelerated under several hundreds of kV, achieving an velocity ($> 2 \times 10^8$ m/s) that approaches the speed of light. Practically, the resolution in TEM is limited by the objective lens system to ~0.1 nm. An advanced TEM may include various aberration correctors to reduce the degree of distortion in the image. To date, the state-of-the-art transmission electron aberration-corrected microscope has a spatial resolution as low as 0.05 nm, which is roughly half the size of an hydrogen atom.

Selected area electron diffraction (SAED) is a crystallographic technique that can be employed inside a TEM. The electrons in TEM are more wave-like than particle-like and can be diffracted by atoms similar to XRD. SAED patterns consist of sharp diffraction spots. Each spot represents a reciprocal lattice. As the area selected by SAED can be as small as several hundred nanometers in size, it can examine samples which are too small for XRD.

The thin film and powder TEM samples were prepared differently. The thin film sample was shaped by focused ion beam incorporated in FEI xT Nova NanoLab 200, and then

lifted out by a glass needle and transferred onto a copper grid. The powder sample was first dispersed in ethanol by ultrasonication, and then dropped onto a copper grid. The copper grad containing the sample was analyzed by JEOL 2200FS and Phillips CM200 TEM system.

### 3.2.4 Atomic force microscopy

Atomic force microscopy (AFM) is a type of scanning probe microscopy (SPM) [140]. During the scanning, a probe fixed to the open end of a small spring-like cantilever is brought into contact with the sample surface, either in direct contact mode or tapping at a tiny distance above (tapping mode). The force that the sample imposes on the probe can be measured and used to create a three-dimensional topography of the sample surface. Although the resolution in horizontal x-y plane is moderate, the resolution at vertical z direction can achieve the order of an angstrom. In this work, Bruker Dimension ICON SPM is used to examine the surface roughness of the thin film sample.

### 3.2.5 Raman spectroscopy

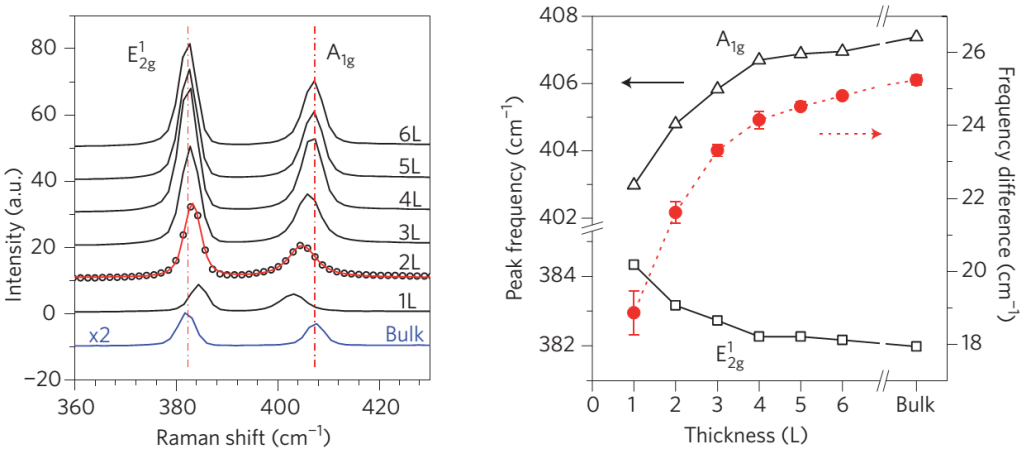


**Figure 3.5 Raman spectra of few-layer and bulk $MoS_2$ (left), and peak position for the $E^1_{2g}$ and $A^1_g$ modes as a function of layer number (right) [141].**

Raman spectroscopy is a technique used to detect vibrational, rotational, and other low-frequency modes in a material. It is based on inelastic scattering of a laser covering near ultraviolet, visible, and near infrared range. The laser energy alters after interacting with

molecular vibrations and rotations, offering a structural fingerprint specific to those modes of the system. Raman spectroscopy can be used to determine the thickness of few-layer $MoS_2$. As the thickness of $MoS_2$ decreases, the $E^1_{2g}$ vibration mode red-shifts while the $A_{1g}$ vibration mode blue-shifts, as shown in figure 3.5 [141]. In this work, Raman spectra were collected in the Renishaw InVia Raman microscope equipped with 3000 I/mm grating and 532 nm line of Ar ion laser.

### 3.2.6 Secondary ion mass spectrometry

Secondary-ion mass spectrometry (SIMS) is a technique used to identify the elemental composition of a specimen by applying a focused ion beam on sample surface and detecting the mass/charge ratios of rejected secondary ions with a mass spectrometer. It is very effective to examine the isotopic composition of an element as isotopes like carbon-12 and carbon-14 have different mass. SIMS is even more surface sensitive than XPS, only signals from a depth of 1-2 nm below the surface are collected. However, since ion beam can also etch the surface at the same time, making it possible to analyze the in-depth distribution of the elements. In this work, Cameca IMS 5FE7 system with oxygen ion source is used.

### 3.2.7 X-ray photoelectron spectroscopy

In X-ray photoelectron spectroscopy (XPS), core electrons are ejected from the material after absorbing photons with energy higher than the binding energy of the electron. The excess energy is converted to kinetic energy of ejected photoelectrons, which can be measured by an electron analyser. It is easy to calculate the binding energy if the energy of the incident photon and the work function of the spectrometer are known. XPS is very sensitive to the chemical state of an element. The shift of binding energy, also called chemical shift, as well as the shape of XPS peaks can be used to determine the local coordination in a material. In this work, Thermo ESCALAB250Xi X-ray photoelectron

spectrometer is used with a monochromatic Al Ka source (1486.68 eV). All binding energies were referenced to the C 1s peak at 284.85 eV.

### 3.2.8 X-ray absorption spectroscopy and X-ray magnetic circular dichroism

The X-ray absorption spectroscopy (XAS) tracks the absorption intensity as a function of the incident X-ray energy, which is tuned to a range of 0.1-100 keV that the core electrons of a certain element can be excited. Based on the principal quantum number n of the excited core electrons, the spectra are called K-, L-, M-edges for n=1, 2, 3, respectively. As the initial state of a core electron is well defined by quantum mechanics, the excitation must follow the selection rules. Generally, the most prominent features of the excitation are caused by electric-dipole transitions ($\Delta\ell = \pm 1$), for example, 1s to p-like final states for a K-edge XAS.

If the material is ferromagnetic, the X-ray absorption process becomes spin-dependent and can be detected by X-ray magnetic circular dichroism (XMCD). In XMCD, two XAS, one with left circularly polarized light and the other with right circularly polarized light, are measured in a magnetic field. Magnetic properties, such as the orbital and spin magnetic moments, can be obtained by analyzing the difference between two XAS spectra. In this work, XAS and XMCD were measured at Singapore synchrotron light source.

### 3.2.9 Superconducting quantum interference device

Superconducting quantum interference device (SQUID) is currently one of the most sensitive magnetometer employed to measure ultra-small magnetic fields with detection limit as low as $10^{-8}$ emu. The core of the SQUID is two parallel Josephson junctions. Each junction consists of two superconducting regions separated by a thin insulating barrier. Any change of magnetic flux through the SQUID can cause periodic voltage response. The periodicity of the voltage oscillation is equal to one flux quantum, $\Phi_0$, and is effective

to evaluate the magnetic flux change. In this work, we use Quantum design-XL-7 to measure the magnetization of the samples as a function of external magnetic field at different temperatures. During a typical test, the external magnetic field starts from highest point (50 kOe) and gradually decreases to lowest value (-50 kOe), and then restores to 50 kOe. If the sample is ferromagnetic, the result is a hysteresis loop in which magnetization quickly saturates at Ms with a nonzero coercivity.

### 3.2.10 Polarized neutron reflectometry

Polarized neutron reflectometry (PNR) is a technique well suited for measuring the nanostructure of magnetic thin films. The principle is similar to the complementary technique, X-ray reflectivity (XRR). The basic idea behind the technique is quite simple, a neutron beam is incident on a thin film with flat surface at a grazing angle and reflected in the specular direction (reflected angle is equal to incident angle). The reflected intensity is then measured as a function of the scattering vector $q_z=4\pi\sin(\theta)/\lambda$ ($\lambda$ is the neutron wavelength and $\theta$ is the angle of incidence). While XRR can only obtain the chemical compositional depth profile, PNR can provide additional magnetic information by polarization of incident neutrons.

Although reflected patterns contain structure and magnetic information of each layer above the substrate, such as thickness, density, interface roughness and magnetic moment, the exact mathematical relationship is very complicated, especially for thin films with multiple layers. Instead of direct calculation, the results must be extracted through mathematical analysis by manually fitting the parameters to get a simulated curve close enough to the measured data. In this work, PNR was measured in Australia Neutron Science Technology Organization (ANSTO) and Igor Pro 7 was used to fit the data.

### 3.2.11 Electron spin resonance

Electron spin resonance (ESR), also known as electron paramagnetic resonance (EPR), is the spectroscopic technique that unambiguously detects unpaired electrons in a material. Electron is a Dirac fermion with spin quantum number s=1/2. Under an external magnetic field with strength $B_0$, electrons align in the way with magnetic moments either parallel ($m_s$=-1/2) or antiparallel ($m_s$=1/2) to the field. Due to Zeeman effect, each electron has a specific energy proportional to $m_s$: $E=m_s g_e \mu_B B_0$, where $g_e$ is the g-factor for electrons. Thus, the splitting between the lower and higher energy state is $\Delta E=g_e \mu_B B_0$. Initially, more electrons stay in the lower energy level than in the upper level, but an unpaired electron can move from lower level to higher level by absorbing a photon with energy exact equals to $\Delta E$ ($h\nu=g_e \mu_B B_0$). In ESR, the sample is exposed to microwave irradiation with a fixed frequency while sweeping the external magnetic field. When the external magnetic field meets the resonance condition, there is a net absorption of energy which can be monitored by ESR. In the most cases, the first derivative of the absorption spectrum is used to analyze ESR result. In this work, Bruker EMX X-Band ESR spectrometer was used for the measurements.

# Chapter 4 Microstructures and Magnetic Properties of Co Doped $TiO_2$ Thin Film Prepared by Pulsed Laser Deposition

## 4.1 Overview

Diluted magnetic semiconductors (DMSs) have drawn a great deal of research attention over the course of past few decades, in the hope of the realization of a technology that can integrate logic semiconductors with magnetic information-storage capability. Traditional II-VI and III-V DMSs have a typical Curie temperature (Tc) much lower than room temperature. Diluted magnetic nitrides and oxides (DMNs and DMOs) have become a brand new research highlight after Tc above room temperature was predicted in these materials by Dietl [30].

$TiO_2$, with various crystal structures and properties, has great potential in applications including sensors, solar cells, photocatalyst, as well as spintronic devices [142-145]. Co-$TiO_2$ has demonstrated to be a remarkable promising DMS system with room-temperature ferromagnetism in both rutile and anatase forms in a variety of morphologies, such as thin films [146-148], nanoparticles [149], and nanorods [150]. However, even as researchers have struggled for years to clarify the origin of the ferromagnetism in the system, they failed to achieve a fully convincible explanation.

In previous studies of our group, 5 at% Co doped anatase $TiO_2$ epitaxial thin films are grown by PLD under different oxygen partial pressures ($10^{-4}$, $10^{-5}$, and $10^{-6}$ torr) [151]. From the hysteresis loops, the magnetic moments from Co are 1.03 and 0.93 $\mu_B$ for samples grown under $10^{-6}$ and $10^{-5}$ torr, while the magnetization of the $10^{-4}$ torr sample is negligible. Further depth-resolved LE-μSR measurement indicates the $10^{-6}$ torr sample is fully magnetic and controlled by oxygen vacancies.

The magnetic moment observed in Co-$TiO_2$ so far typically lays in the range of 0.01 and 1.7 $\mu_B$/Co (value of bulk Co metal), while higher saturation magnetization surpasseing 2 $\mu_B$/Co has only occasionally been reported. High magnetization materials are of importance for the applications of magnetic recording media, permanent magnet, transformer and bioapplications [152]. It is found that nanoclusters have shown enhanced magnetic moment compared with their bulk counterparts [153, 154].

However, due to the frustration of surface dangling spins, the Curie temperature of nanoclusters significantly decrease, which is unwelcome for practical applications [155, 156]. During the development of DMSs, giant magnetic moments have been occasionally witnessed in the systems with transition metal doping. For example, 7.5±0.5 $\mu_B$/Co was reported in Co doped $SnO_2$ grown by pulsed laser ablation [157], while a colossal magnetic moment of more than 4000 $\mu_B$ per Gd atom was achieved by Gd doped GaN grown directly on 6H-SiC (0001) substrates using reactive MBE with very low doping concentrations [158]. However, the mechanism for the high magnetic moments remains unsolved since in most studies, only magnetometer measurement is used and there is no direct evidence to link the observed high magnetic moment to the magnetic element.

In this work, we deposited 5 at% Co doped $TiO_2$ thin film on $LaAlO_3$ (001) (LAO) substrate by PLD equipped with a 248 nm KrF excimer laser. 5 at% Co doped $TiO_2$ target was prepared by first mixing $Co_3O_4$ and $TiO_2$ (99.99 % in purity) powders in a mortar. Afterward, the mixed powders were pressed into pellet and then sintered in a furnace at 1300 $^oC$ for 10 h in air. Prior to deposition, the LAO substrates were cleaned by alternative ultrasonication in acetone and ethanol for several times. The deposition was carried out at 650 $^oC$ and oxygen partial pressure of $10^{-5}$ torr. The laser fluence and deposition were

kept at ~2.5J/cm$^2$ and 5 Hz, and the final film thickness was controlled to be around 60 nm.

With the delicate control of deposition parameters, we achieve the microstructure of Co clusters embedded in $TiO_2$ matrix. XMCD measurement indicates that Co has a very high magnetic moment of 3.5 $\mu_B$. In addition, O edge contributes significantly to the overall magnetization, whereas, Ti edge shows a much weaker XMCD signal. PNR measurement supports the high magnetization of the films and a saturation magnetization as high as 106 emu/cm$^3$ has been achieved. We use first principles calculations to investigate metallic nanoclusters embedded in oxide semiconductor matrix by considering spin-orbit coupling. It is found that high magnetic moment (2.9 $\mu_B$/Co) can be obtained with clusters containing 14 atoms, agreeing well with experimental results. We have demonstrated that magnetic clusters embedded in oxide semiconductor matrix are able to show high magnetic moment above room temperature.

## 4.2 Microstructure study of Co doped $TiO_2$ thin film

Based on the results of numerous studies, Co can achieve either uniform or non-uniform distribution in $TiO_2$. The three possible states of Co are illustrated in figure 4.1. Clustering of metallic Co or coexistence of clustering and uniform doping are the microstructure of $TiO_2$ thin films commonly observed due to the difficulty to obtain uniform doping. For our PLD grown 5 at% Co doped $TiO_2$ thin films, it is found that the microstructures are strongly associated with deposition parameters. In our previous work, magnetic uniformity with Ms between 20-40 emu/cm$^3$ was achieved by the deposition with a laser fluence of 1.0-1.8 J/cm$^2$ under the oxygen partial pressure of $10^{-6}$ torr. Segregation of dopants starts to appear by increasing the oxygen partial pressure to $10^{-5}$ torr, leading to a decreased Ms around 20 emu/cm$^3$. However, we further discover that although thin

films deposited at higher laser fluence under same pressure ($10^{-5}$ torr) still show Co clusters, the Ms is enhanced more than 4 times. Therefore, in this work, we focus on Co-$TiO_2$ film deposited under this condition.

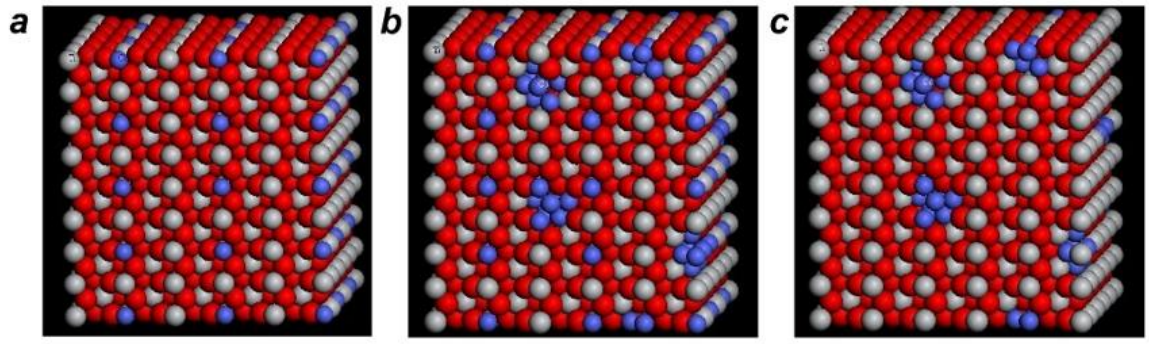


**Figure 4.1 Three possible states of Co with $TiO_2$ matrix: (a) substitution, (b) coexistence of clustering and uniform doping and (c) metallic Co clusters.**

Figure 4.2 shows the XRD pattern of 5 at% Co doped $TiO_2$ deposited under an oxygen partial pressure of $10^{-5}$ torr. Only two peaks can be observed in XRD, one is located around 37.8º and another tiny peak appears around 80.7º. This two peaks are identified as anatase (004) and anatase (008). Thus, the $TiO_2$ thin film shows pure anatase phase. For PLD with optimal parameters, the deposited materials tend to form a crystalline overlayer which has well-defined crystallographic orientations with respect to the crystal structure of the substrate. This process is called epitaxial growth. Because the substrate is served as a seed crystal, during initial stage of deposition, atoms of deposited film rearrange to match the lattice of substrate surface. LAO has a rhombohedral structure at room temperature (space group R-3c) with lattice *a* and *c* equal to 0.536 and 1.311 nm. However, it is more often represented as pseudocubic structure with a=0.3793 nm. Meanwhile, anatase is tetragonal with lattice parameters a=0.378 nm and c=0.951 nm. The lattice mismatch between anatase (001) and LAO (001) is only -0.26%. Thus, anatase is expected to grow on LAO with orientation relationships of $(001)_{anatase}||(001)_{LAO}$ in out-

of-plane direction and $[100]_{anatase}||[100]_{LAO}$ in in-plane direction, which is in agreement with the XRD result (out-of-plane).

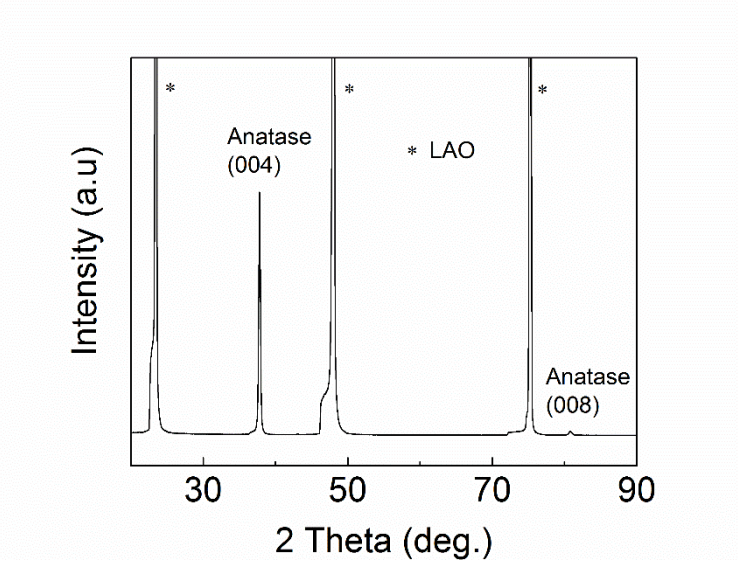


**Figure 4.2 XRD pattern of 5 at% Co doped $TiO_2$ thin film.**

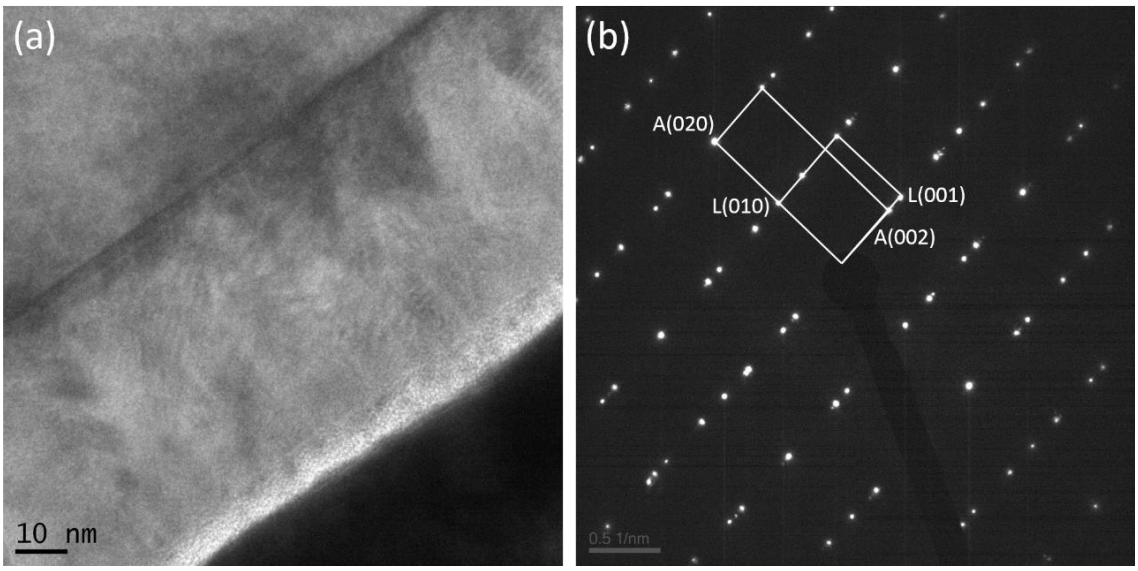


**Figure 4.3 (a) TEM image and (b) selected area diffraction of Co doped $TiO_2$ thin film.**

Figure 4.3(a) shows TEM micrograph of the thin film. It can be seen that the thickness of the film is around 60 nm. The SAED pattern shown in figure 4.3(b) reveal the perfect epitaxial structure of the thin film without any polycrystalline dots. Unlike XRD 2θ-ω scan which can only examine the epitaxial relationship in out-of-plane direction. SAED from TEM clearly shows that the in-plane orientation relationships between anatase $TiO_2$

thin film and LAO substrate is $[100]_{anatase}||[100]_{LAO}$ and $[010]_{anatase}||[010]_{LAO}$, agreeing well with the simulation result.

Nanoclusters with varied dimensions are observed near the interface by high-resolution TEM, as shown in figure 4.4(a). While large clusters with diameters close to 5 nm (marked by circles) are located at the interface, smaller nanocluster with size of just 1-2 nm can also be seen near the interface, as indicated by the arrows. EDS mapping was performed in order to evaluate the distribution of the nanoclusters in the entire film and the results are shown in figure 4.4(b) and (c). Ti and O are uniform in the entire film without precipitates. In contrast, Co is non-uniform in the whole area and most is segregated near the interface, which is consistent with the HRTEM result.

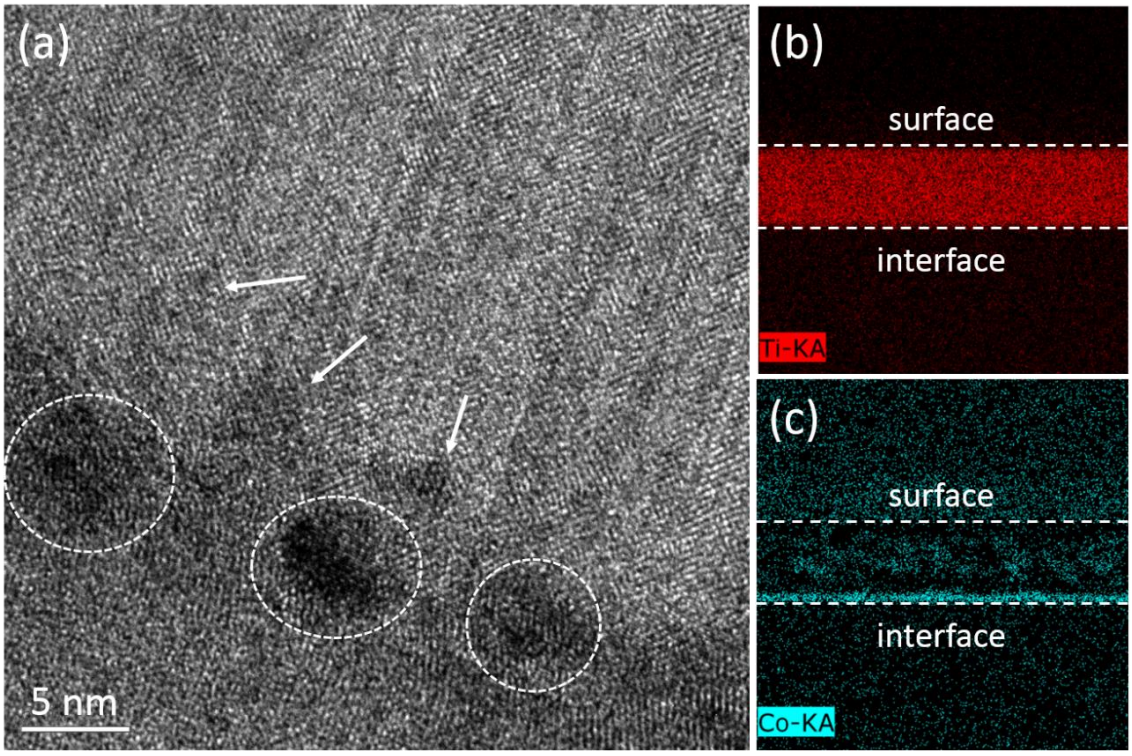


**Figure 4.4 (a) High resolution TEM image. EDS mapping of (b) Ti and (c) Co element, respectively.**

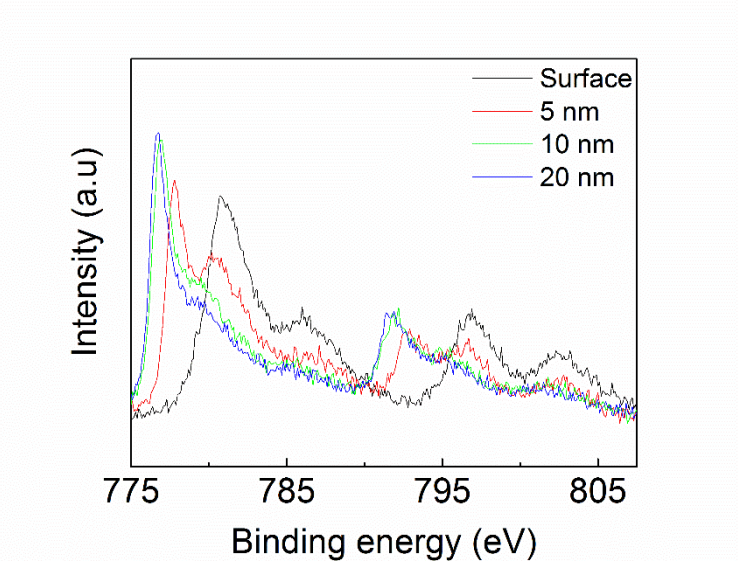


**Figure 4.5 XPS spectrum of Co edge (2p core-level).**

The presence of Co nanoclusters can be identified by XPS since Co valence state in the clusters should be $Co^0$. The XPS spectra of Co 2p core level at different depths are shown in figure 4.5. Because XPS can only collect signals of electrons that escape from the top 5 nm of the thin film, an argon ion beam was employed to etch the thin film to reveal the layers beneath surface. The weak satellite characteristics ascribed to $Co^{2+}$ are observed at the surface. However, the sharp $Co^0$ peak with binding energy of ~778.2 eV and significantly spin-orbit splitting ($\Delta_{metal}$=14.99eV) soon becomes dominant after etching. Only at shallow depth of 5 nm, Co shows a mixture of metallic and a tiny fraction of oxidized valence states. Below 10 nm from the surface, XPS only shows $Co^0$ state, indicating that the majority of Co in $TiO_2$ is metallic. Thus, the ionized state of Co in the surface layer may be caused by surface oxidation of the thin film. In order to further identify the valence state of Co dopants in $TiO_2$ thin film, XANES was performed in Singapore Light Synchrotron [159]. As shown in figure 4.6(a), compared with CoO and Co reference samples, the spectrum of Co in $TiO_2$ is much more similar to the latter, suggesting that Co mainly exists as metallic state. Fourier transformation, illustrated in

figure 4.6(b), further confirms that Co dopants in $TiO_2$ is $Co^0$ since it has the same Co-Co distance and coordination numbers as that of metallic Co.

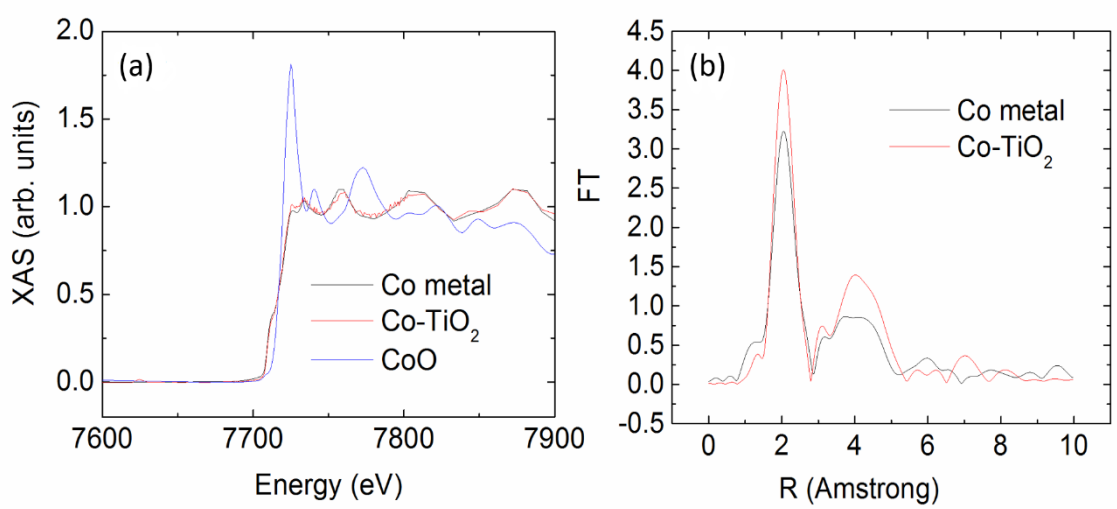


**Figure 4.6 (a) NEXAS of Co K edge in Co doped $TiO_2$ and two reference samples, Co metal and CoO. (b) Fourier transformation of reference Co metal and Co in Co doped $TiO_2$.**

## 4.3 Magnetic properties of Co doped $TiO_2$ thin film

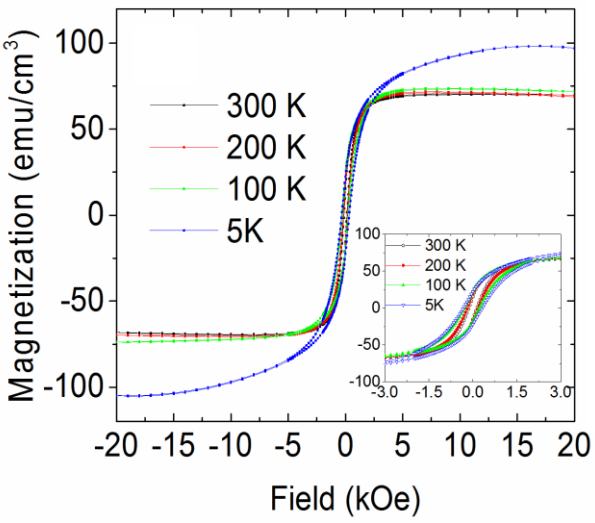


**Figure 4.7 Hysteresis loops measured at different temperatures.**

Figure 4.7 shows the M-H loops of Co doped $TiO_2$ thin film measured at different temperatures. The film shows a surprisingly high saturation magnetization of 70 emu/$cm^3$ at room temperature, which is even higher at 5 K (98 emu/$cm^3$). From the inset, the coercivity and remanence magnetization (~17 emu/$cm^3$) of the hysteresis loops confirm

the ferromagnetic ordering at room temperature. The fast increase in magnetization at 5 K suggests there may be some paramagnetic phases at room temperature. Given that the magnetization is entirely contributed by the 5 at% Co dopants, each Co atom has a magnetic moment of 4.73 $\mu_B$ at room temperature. It is known that bulk metallic Co has a magnetic moment of 1.72 $\mu_B$/Co, which is much lower than those observed in this work.

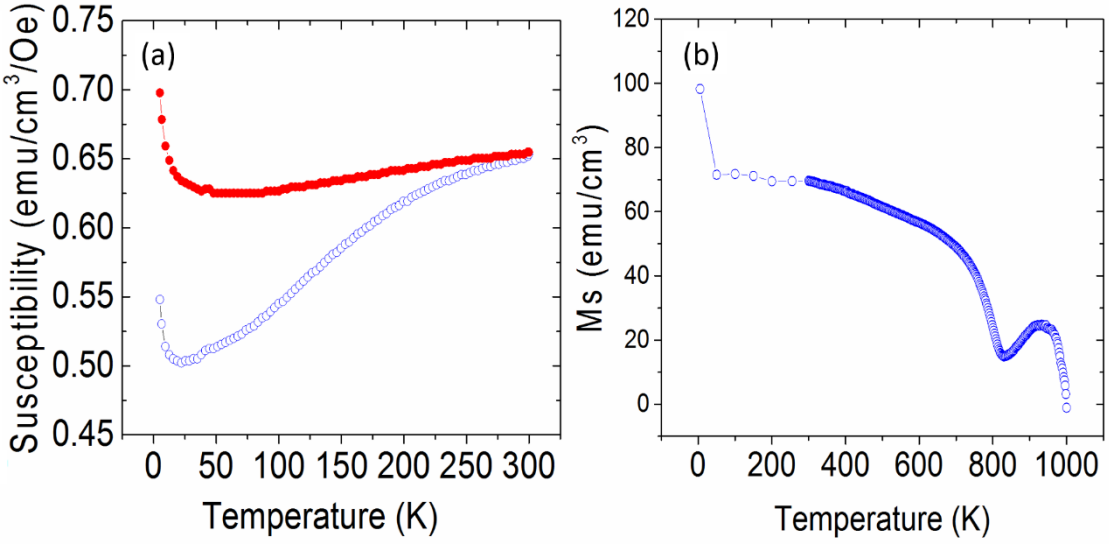


**Figure 4.8 (a) ZFC/FC curves of Co doped $TiO_2$ thin film. The magnetic field applied is 500 Oe. (b) Temperature dependence of magnetization that shows the Curie temperature.**

Figure 4.8(a) shows the ZFC and FC curves of the thin film. The relatively high magnetization at low temperature indicates the presence of paramagnetic orderings, consistent with hysteresis loop measurement. Superparamagnetism is frequently observed in systems with ultra-small magnetic nanoparticles (Fe, Co, Ni). For example, ion beam fabricated Co nanoparticles with size smaller than 3 nm lead to superparamagnetic behaviour in $SiO_2$ film while clusters above 7 nm only result in ferromagnetism [160]. Superparamagnetism can also be observed in Co ion-implanted $TiO_2$ thin film, which disappears after postannealing due to enlarged cluster size [161]. However, no superparamagnetic feature can be observed in the ZFC/FC curves, suggesting the estimation of nanocluster size from TEM may not accurate and the smaller nanoclusters are still above the critical diameter. In order to further understand the mechanism of the

ferromagnetism, Curie temperature was measured in a furnace attached to a SQUID system. Two critical temperatures, 800 and 1000 K, are observed in the curve (figure 4.8(b)). From analysis above, Co dopants in $TiO_2$ have complex compositions, including at least large and small nanoclusters in the interface and oxidation at shallow depth, which may have different critical temperatures. It should be noted that 1000 K is still much lower than the Curie temperature of bulk Co (1400 K), suggesting nanostructured Co can reduce the Curie temperature.

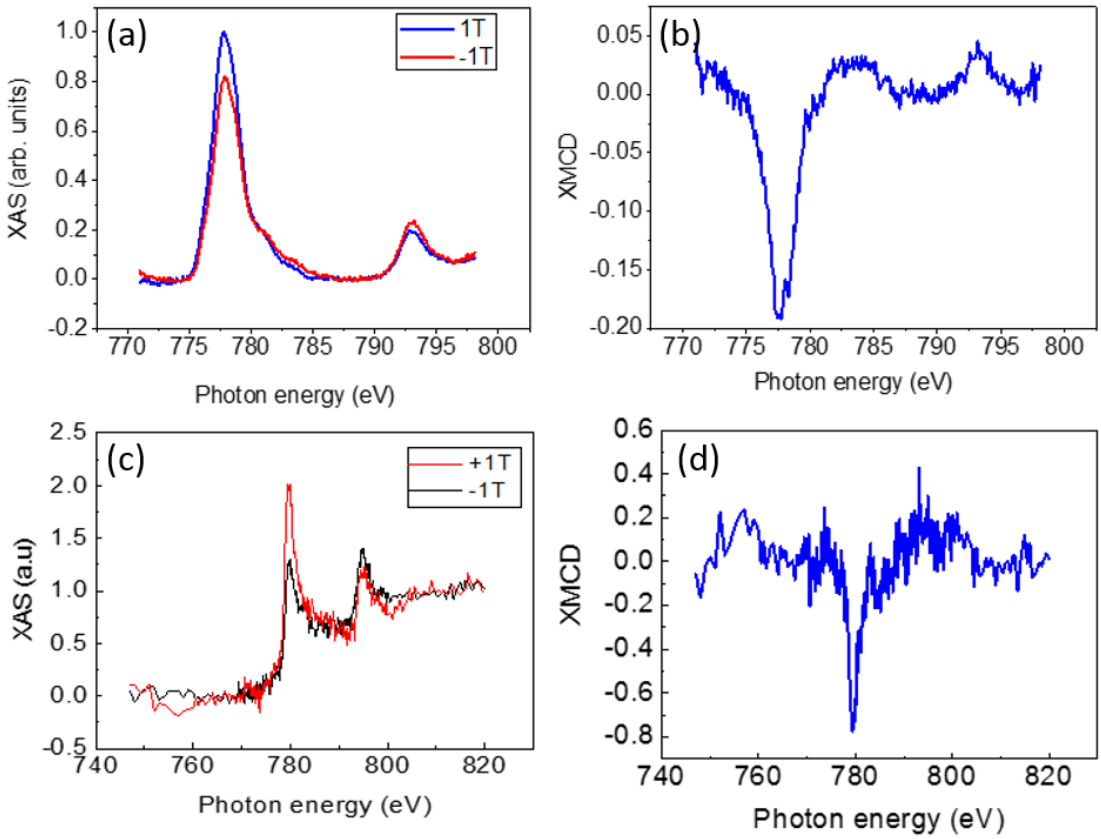


**Figure 4.9 XAS and XMCD spectra of Co L edge. The signals are collected by (a, b) total yield mode and (c, d) Florence mode.**

SQUID measurement can only provide the overall magnetization of the entire sample. To uncover if Co dopant alone contributes to the high magnetic moment, XMCD was employed to evaluate the individual moment contribution from each element in Co doped $TiO_2$ thin film. Figure 4.9(a) present the XAS spectra of Co L edge by applying a magnetic field of 1T and -1 T using the total yield mode and the correspond XMCD

results of Co are shown in figure 4.9(b). From sum rules [162], in the transition of XAS from 2p→3d, the lz sum rule can be written as: $\langle l_z \rangle = -2\frac{\int d\varepsilon(I_+ - I_-)}{\int d\varepsilon(I_+ + I_- + I_0)}$, where $\langle l_z \rangle$ is the average of the magnetic quantum number of the orbital angular momentum per 3d hole. $I_0$ is the XAS with the linearly polarized light whose polarization vector is parallel to the magnetization. The integration $\int_{j=3/2}(\int_{j=1/2})$ is taken over the whole $2p_{3/2}(2p_{1/2})$ absorption region. The $S_z$ sum rule is written as: $\langle S_Z \rangle + \frac{7}{2}\langle t_Z \rangle = -\frac{3}{2}\frac{\int_{j=3/2} d\varepsilon(I_+ - I_-) - 2\int_{j=1/2} d\varepsilon(I_+ - I_-)}{\int d\varepsilon(I_+ + I_- + I_0)}$, where $t_Z$ is the z component of the magnetic dipole operator $t = s - 3r(r \cdot s)/|r|^2$. The integration is taken only over the absorption region.

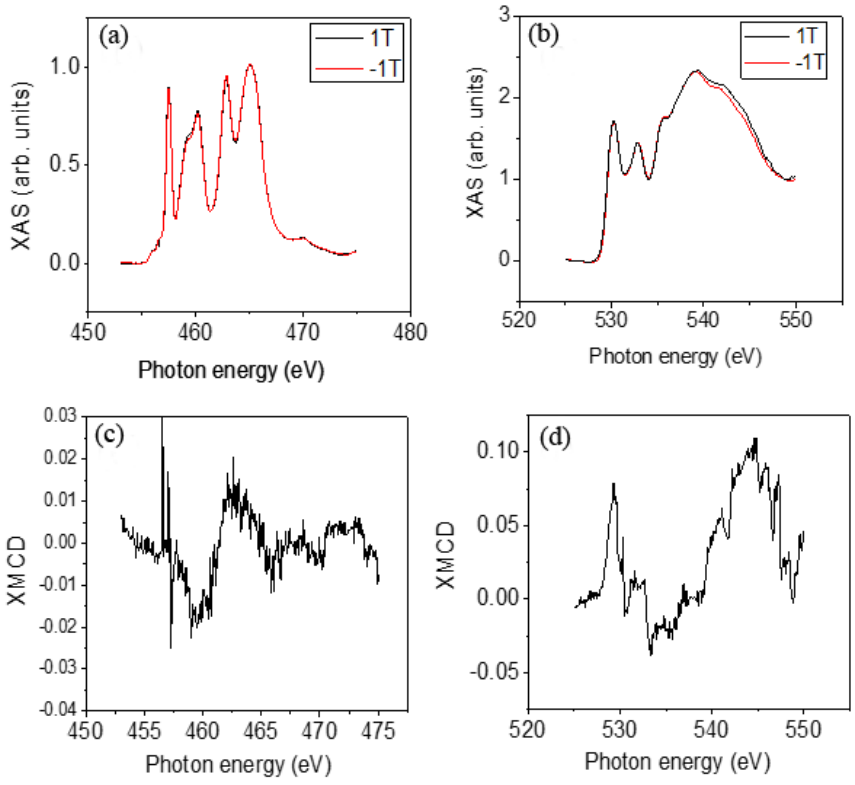


**Figure 4.10 XAS spectra of (a) Ti L edge and (b) O K edge. XMCD spectra of (c) Ti L edge and (d) O K edge. The XAS is collected by total yield mode.**

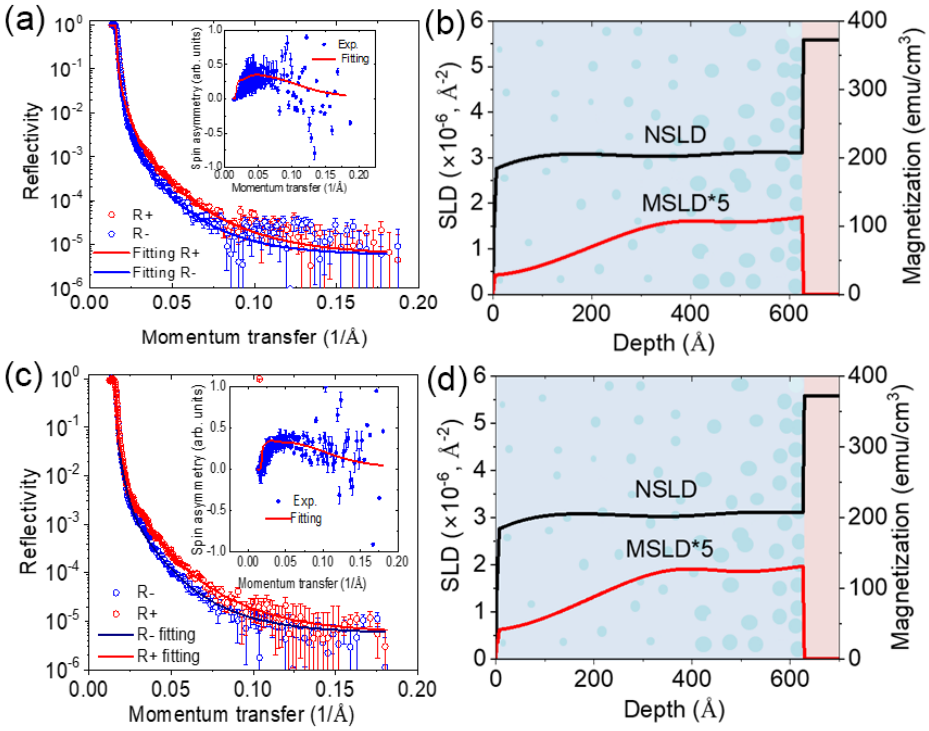


**Figure 4.11 PNR spectra of Co doped $TiO_2$ film. (a) Reflectivity versus moment transfer and (b) SLD curves at 300 K; (c) Reflectivity versus moment transfer and (d) SLD curves at 5 K.**

Considering the beam polarization is 0.9, the calculated orbital moment $\mu_L$ and spin moment $\mu_S$ are 0.62 and 0.96 $\mu_B$, respectively. The total magnetic moment (1.58 $\mu_B$) is much lower than that obtained from magnetic hysteresis loop measurement (4.73 $\mu_B$ at room temperature). The XAS signals in the total yield mode are mainly collected from surface and oxide based diluted magnetic semiconductors often have a dead layer on the surface, leading to an underestimated magnetic moment [163]. Hence, XMCD is further measured by the Florence mode, as shown in figure 4.9 (c). From the calculations based on sum rules, $\mu_S$=3.06 $\mu_B$ and $\mu_L$=0.43 $\mu_B$ (Using step function to remove the background). Hence, the total magnetic moment of Co is approximately 3.49 $\mu_B$. However, it is still much lower than that obtained from hysteresis loop measurement by SQUID. XAS and XMCD of Ti and O element were further measured and the results are shown in figure

4.10. While XMCD signal from Ti L edge is insignificant, a large XMCD response can be obtained from O K edge. Due to the lack of hole information, we can no longer calculate the magnetic moments of Ti L and O K edge by using sum rules, but they may contribute to the high magnetization of the thin film in addition to Co nanoclusters.

As discussed above, the Co doped $TiO_2$ thin film is not uniform, in which the formation of precipitation tends to take place in the interface and a magnetic dead layer may form in the surface. The absence of spatial uniformity has been reported in numerous studies, but how the unevenly distribution of dopants influence the magnetic properties remains unclear [163-166]. To identify the magnetization in the interface and the dead layer is critically important for understanding the magnetism in the film. In this work, the depth profile of the magnetism is evaluated by PNR.

Although the thickness of 60 nm is estimated from TEM image, the reflectivity curves shown in figure 4.11 (a) and (c) do not display clear oscillations, indicating the surface is very rough. We fitted the curves considering the thickness measured by TEM, saturation magnetization measured by SQUID, and microstructure identified by TEM and XPS. Figure 4.11 (b) and (d) are nuclear scattering length density (NSLD) and magnetic scattering length density (MSLD) at 300 and 5 K, respectively. Slightly lower NSLD in the surface is expected due to surface roughness. Interestingly, a sunken area appears at round 38 nm in NSLD curve, which corresponds the peak of MSLD, the area with the highest magnetization. The sunken area in NSLD suggests relatively high concentration of Co clusters since Co ($2.265\times10^{-6}/Å^2$) has a lower NSLD than that of $TiO_2$ ($2.684\times10^{-6}/Å^2$). From TEM and EDS mapping, in addition to the relatively large Co clusters located near the interface, there are also very small Co clusters distributed inside the film, which may be attributed to the magnetization peak. On the other hand, the surface area of the thin film present minor Ms from $Co^{2+}$, indicating that Co nanoclusters play a decisive role

in the high magnetization. The average Ms of the thin film obtained from MSLD is around 75 emu/cm$^3$ at 300 K and 99 emu/cm$^3$ at 5 K, well agreed with the SQUID results. Moreover, the highest Ms from the peak of MSLD reaches around 106 emu/cm$^3$.

## 4.4 First-principles calculations

In order to further understand the mechanism behind the high magnetic moment, we asked collaborators (Dr. Xiangyuan Cui and Prof. Simon P. Ringer) performed first-principles spin-polarised calculations under density functional theory (DFT). Considering the challenging nature of magnetic moment involved, especially the orbital contribution [167, 168], we employed different schemes for the electron exchange and correlation functionals, namely generalized gradient approximation (GGA) [169], the mean field approximation GGA+*U* (with a large Hubbard *U* parameter, *U*=6 eV for both Co-3d and Ti-3d [168, 170]) and the screened hybrid functional of Heyd, Scuseria and Ernzerhof (HSE) [171] (the Hartree-Fock mixing parameter is set to 0.2), as implemented in the VASP code [172]. The spin-orbit coupling (SOC) was included self-consistently. The cutoff energy of plane-wave basis set and the energy convergence criterion between two electronic steps were 500 eV and $10^{-4}$ eV, respectively. The first Brillouin zone was sampled by a *k*-mesh of 2 ×2 ×1 for the 3×3×1 anatase $TiO_2$ supercell containing 108 atoms. In anatase $TiO_2$, each Ti atom is coordinated to six O atoms, and each O atom to three Ti atoms. To construct the metallic clusters in $TiO_2$ supercell, we first removed some central adjacent Ti and O atoms and then filled some Co atoms. For instance, we removed one Ti atom and its six bonding O atoms, and filled with 6 or 7 Co atoms. To accommodate larger Co clusters (11Co, 14 Co and 15 Co), we further removed three or four Ti atoms. This leads to strong local structural distortion as revealed by internal atomic relaxation. Subsequently, the volume relaxation by keeping c/a constant and

lattice angles as 90 °was conducted. The specific numbers of removed and added atoms, and the relaxed lattice constants of the supercells are shown in Table 4.1. Atomic positions were optimized in all the calculations until the maximum force on each atom is less than 0.02 eV/Å.

Figure 4.12 illustrates the spin density of various Co nanoclusters along [100], [010] and [001] spin axis directions by HSE-SOC. It is to note that for 11Co, the HSE-SOC calculation did not converge. Calculations show that the easy spin axis for Co nanoclusters is along [001] direction with an isosurface value of 0.02 electron/$Å^3$, while isosurface value is 0.0001 electron/$Å^3$ for [100] and [010].

The calculated ground state spin and orbital contributions to the magnetic moments of metallic Co clusters in $TiO_2$ along the easy spin axis [001] direction by different methods are summarized in Table 4.2. It is evident that orbital polarization contributes sizably to the overall magnetic moment, consistent with experimental results. Moreover, it is seen that both spin moment and orbital moment calculated from GGA+U and HSE are substantially larger than those of from GGA. As expected, due to the constrained inter-atomic electron motion [173], the magnetic moments of the embedded metallic Co clusters are smaller than isolated Co clusters. However, as discussed afore, the isolated clusters have low Curie temperature and are unsuitable for practical applications [168]. For these three methods in our work considering spin-orbit coupling, both the spin and orbit moments give similar trends regarding the spin and orbital moments for the small clusters.

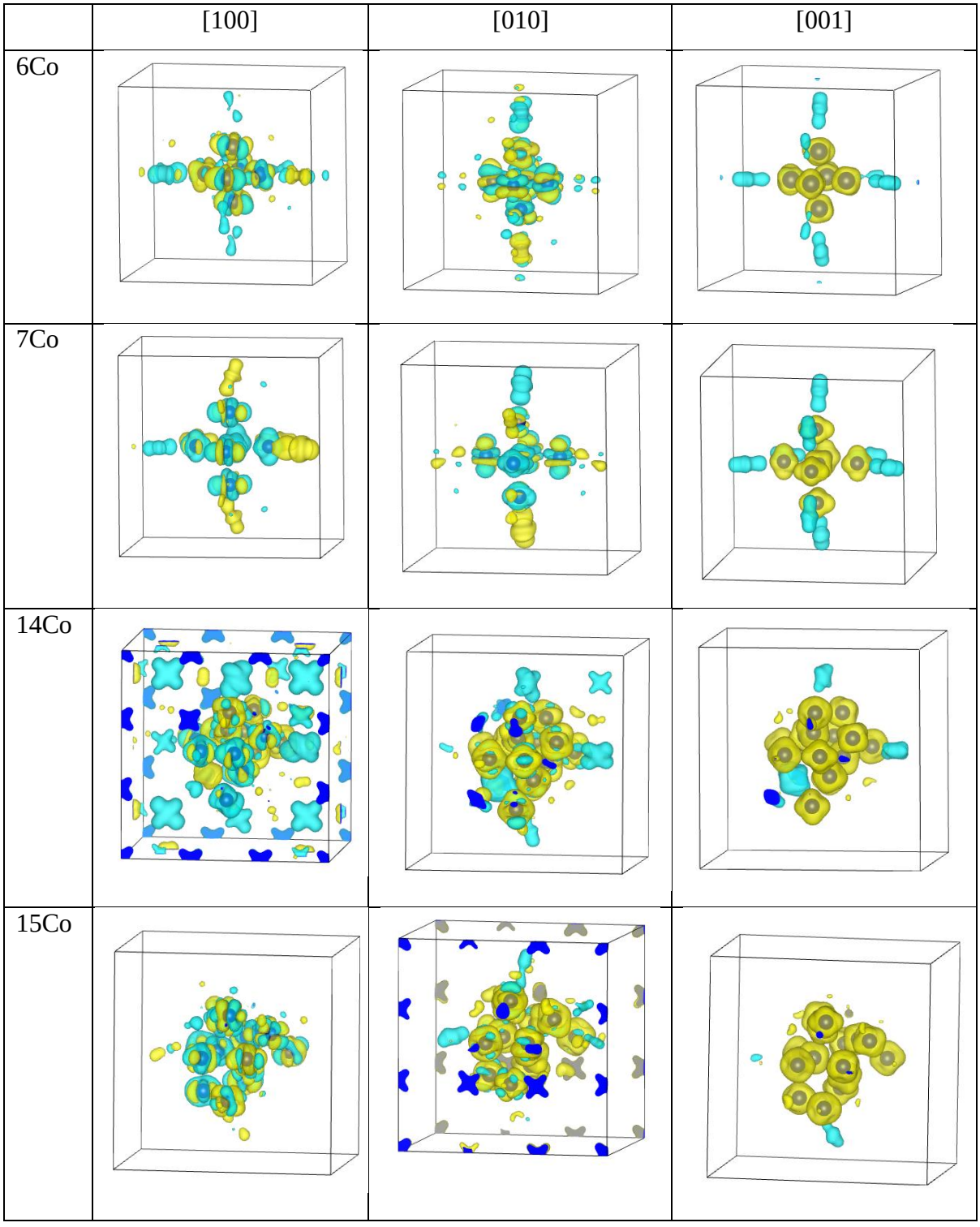


**Figure 4.12 The calculated spin density plots along different spin axis directions for various metallic Co clusters embedded in $TiO_2$ matrix (HSE-SOC). Yellow (blue) isosurfaces denote positive (negative) spin polarization. For simplicity, the Ti and O atoms are omitted.**

Based on the limited number of Co clusters considered, the magnetic moment seems to increase with the metallic Co cluster size for GGA calculation. However, for GGA+U+SOC calculation, the magnetic moment reaches maximum for 14 Co nanoclusters, which has the same trend as that calculated in Ref. [174]. For HSE-SOC method, the magnetic moment also reaches maximum for 14 Co atoms and 15 Co atoms. A general feature regarding the magnetic structure of these clusters is that while the magnetic interaction among Co atoms are always ferromagnetic, there are some antiferromagnetic ones between the Co clusters and their surrounding Ti and O atoms. Such a cancellation effect leads to the slightly decreased moments observed in the smaller clusters. However, from XMCD results, O edge shows relatively large moment, which may be from the oxygen atoms surrounding Ti vacancies.

**Table 4.1 Composition and lattice constants of different metallic Co clusters embedded in $TiO_2$ matrix (GGA).**

| Systems | Number of Ti atoms removed | Number of O atoms removed | a=b (Å) | c (Å) |
|---|---|---|---|---|
| 0 Co | 0 | 0 | 11.474 | 9.661 |
| 6 Co | 1 | 6 | 11.212 | 9.441 |
| 7Co | 1 | 6 | 11.578 | 9.749 |
| 11Co | 4 | 6 | 11.678 | 9.833 |
| 14Co | 5 | 6 | 11.822 | 9.954 |
| 15Co | 5 | 6 | 12.102 | 10.190 |

From the table, we can also see that the contribution of the orbital moment cannot be negligible. However, compared with XMCD measurement, the DFT calculated orbital moments are considerably smaller. Such an underestimation by DFT has been well documented in the literature [168, 175-177]. XMCD measurement shows that 5 at% Co

in $TiO_2$ has a magnetic moment as high as 3.5 $\mu_B$/atom, which is close to that calculated from GGA+U-SOC and HSE-SOC, but much higher than GGA-SOC. It is known that for transition metal or metal oxide, GGA calculated result is always underestimated. Hence, the first-principles calculations based on GGA+U+SOC and HSE+SOC support the possible high magnetic moments achieved in Co doped $TiO_2$ thin film.

**Table 4.2 Calculated average spin and orbital moments in $\mu_B$/atom along the easy spin axis [001].**

| systems | GGA-SOC | | GGA+U-SOC | | HSE-SOC | |
|---|---|---|---|---|---|---|
| | Spin moment ($\mu_B$) | Orbital moment ($\mu_B$) | Spin moment ($\mu_B$) | Orbital moment ($\mu_B$) | Spin moment ($\mu_B$) | Orbital moment ($\mu_B$) |
| 6Co | 1.21 | 0.14 | 2.24 | 0.21 | 1.89 | 0.17 |
| 7Co | 1.21 | 0.16 | 2.29 | 0.25 | 1.94 | 0.21 |
| 11Co | 1.41 | 0.19 | 2.48 | 0.27 | - | - |
| 14Co | 1.70 | 0.20 | 2.62 | 0.25 | 2.42 | 0.24 |
| 15Co | 1.94 | 0.19 | 2.61 | 0.22 | 2.44 | 0.22 |

We also performed the calculation without SOC. The calculated magnetic moments are listed in table 4.3. As one can see, for most clusters (all except 15 Co), GGA predicts slightly larger spin moments than GGA-SOC. In contrast, including the strong correlation effect in the embedded systems, both GGA+U and HSE consistently predict that the calculated spin moments are much larger when the SOC is included compared to the case when those without SOC for all the embedded clusters are considered. Hence, SOC is one of the factors to affect the magnetic properties of clusters.

To understand the mechanism of high Curie temperature in Co doped $TiO_2$, we performed further DFT calculations by comparing confined Co clusters embedded in $TiO_2$ matrix and free Co clusters. We studied free Co clusters under two states: One is to remove $TiO_2$

matrix and allow the Co clusters relax and the other is to freeze the atomic position of Co after removing $TiO_2$ matrix. By comparing the total energy of the different spin states by considering the diverse initial spin configurations, we observe that Co clusters embedded in $TiO_2$ matrix always leads to robust ferromagnetic ordering with high Curie temperature. In contrast to confined clusters, free Co clusters, either the relaxed and the fixed states, both show various energetically competitive local spin states besides ground states, suggesting that unstable states with low Curie temperatures. Therefore, it can be concluded that confinement effect in the Co clusters embedded in $TiO_2$ matrix is responsible for the high Curie temperature above room temperature. Compared to previous experimental results, Co clusters embedded in $TiO_2$ matrix actually have slightly lower magnetic moment compared to free Co clusters. Hence, the enhancement of magnetic moment comes from the nanostructure of Co itself. It is to note that Ti and O edge also contribute to the high magnetization. Nevertheless, the confinement effect induced high Curie temperature above room temperature may pave ways to achieve practical high magnetization materials if these nanoparticles are embedded in oxides. In addition, the embedded Co clusters are structurally, chemically and magnetically protected by the matrix, hence more stable magnetic properties, compared with free metallic clusters.

**Table 4.3 Calculated average spin moments in $\mu_B$/atom without spin-orbit coupling (SOC).**

| systems | GGA ($\mu_B$) | GGA+U ($\mu_B$) | HSE ($\mu_B$) |
|---|---|---|---|
| 6Co | 1.25 | 2.01 | 1.78 |
| 7Co | 1.27 | 2.21 | 1.85 |
| 11Co | 1.45 | 2.42 | 2.01 |
| 14Co | 1.79 | 2.51 | 2.22 |
| 15Co | 1.89 | 2.47 | 2.27 |

## 4.5 Conclusions

5 at% Co doped $TiO_2$ thin film was deposited on $LaAlO_3$ (001) substrate using a pulsed laser deposition system. XRD result indicates the film is pure anatase phase. Further SAED analysis suggests the orientation relationships between the anatase thin film and LAO substrate are $(001)_{anatase}||(001)_{LAO}$ in out-of-plane direction and $[100]_{anatase}||[100]_{LAO}$ in in-plane direction. Segregation of Co with different sizes are observed near the interface. Larger clusters with diameters around 5 nm are located close the interface, while 1-2 nm small nanoclusters are embedded inside the film. Both XPS and XAS confirm most Co exists as metallic $Co^0$ except a small amount of $Co^{2+}$ in the surface layer.

Assuming that all the magnetization comes from Co, SQUID measurement gives an extremely high magnetic moment of 4.73 $\mu_B$ per Co atom at room temperature, while the result calculated by XMCD is ~3.5 $\mu_B$/Co. Moreover, observed from XMCD, although Ti edge contributes little to the overall magnetization, the signal from O edge cannot be ignored. Further PNR measurement supports the high magnetization of the films and the highest saturation magnetization at the peak area is around 106 emu/$cm^3$.

First principles calculations by GGA+U and HSE support the high magnetic moment of Co when Co clusters are embedded in $TiO_2$ matrix considering spin-orbit coupling, though GGA method underestimates the magnetic moment. A 15-atom Co cluster can obtain a high magnetic moment of 2.9 $\mu_B$/Co, demonstrating that magnetic clusters embedded in oxide matrix are able to show high magnetic moment above room temperature.

# Chapter 5 Cluster-dependent Magnetism in Co-doped $TiO_2$ Thin Film

## 5.1 Overview

$TiO_2$, with various crystal and band structures, has great potential to serve as host material in diluted magnetic semiconductors. Doped with cobalt, Co-$TiO_2$ has demonstrated to be a remarkable promising DMS system with room-temperature ferromagnetism observed in both rutile and anatase thin films. However, after two decades of extensive research, several issues concerning the microstructure and magnetic properties of Co doped $TiO_2$ thin films are still not thoroughly understood.

The first issue is the solubility limit of Co in $TiO_2$. In the initial work of Matsumoto's group, the uniform distribution of Co can be achieved with concentration as high as 8% [56]. Several later studies further push the solubility limit up to 12% [60, 178]. However, the solubility limit in other reports are much lower. For example, PLD grown Co doped $TiO_2$ thin film in Shinde's group can only tolerate the solubility of Co up to 2%, while higher dopant concentrations clear lead to formation of Co clusters [74]. Based on current collective data from numerous studies, uniformly distributed Co in $TiO_2$ can be accomplished at least at low concentrations of less than 2-3% under certain growth conditions.

The second issue is the lack of clear relationship between the growth methods and film microstructure. In an early work, Chambers *et al.* investigated oxygen-plasma-assisted MBE grown Co doped anatase $TiO_2$ thin film at different growth rates and temperatures varied between 300 and 750 $^oC$ [58]. The epitaxial thin films with highest crystalline quality and most evenly dopant distribution are deposited at temperatures in the range of

550-600 $^{o}$C with a slow growth rate around 0.01 nm/s. In the case of higher deposition rate (~0.04 nm/s), rutile nanocrystals appear on the anatase thin film surface due to segregation of Co. Further alter growth conditions can cause all Co dopants segregate to nanoclusters [59].

The final problem is the uncertainty of the relationship of microstructure and magnetic properties, which often leads to contradictory results. For example, in ref.[59], the homogeneous Co doped anatase $TiO_2$ thin film shows no ferromagnetic properties, while tiny magnetic moment of ~0.1 $\mu_B$/Co was shown in ref.[72]. In contrast, our previous work discovered the magnetic uniformity with Ms of ~1.03 $\mu_B$/Co by deposition with a laser fluence of 1.0-1.8 J/cm$^2$ under the oxygen partial pressure of $10^{-6}$ torr [151]. Similarly, no consensus has been reached for Co doped rutile $TiO_2$, although many believe each Co atom possesses a magnetic moment of ~1 $\mu_B$/Co by low spin configuration. The typical magnetic moments observed in Co-$TiO_2$ so far range widely from 0.01 $\mu_B$/Co to 1.7 $\mu_B$/Co, suggesting immature understanding and control of ferromagnetism in the system.

In the last chapter, we achieve an ultrahigh magnetic moment of 4.73 $\mu_B$/Co at room temperature from metallic Co nanoclusters embedded in $TiO_2$ matrix. In order to further clarify how the film microstructure influences magnetic properties, we fabricated Co clusters doped $TiO_2$ thin film with different cluster sizes and distributions by delicate control of the growth parameters during PLD fabrication. We used the same 5 at% Co doped $TiO_2$ target but adopted $SrTiO_3$ (001) substrate this time. The lattice mismatch between anatase (001) and STO (001) is -3.1%, much larger than using LAO (001) (-0.26%), so the tendency of Co segregation is higher. The laser fluence and oxygen partial pressure were kept constant at ~3 J/cm$^2$ and $10^{-5}$ Torr. Two deposition rate and a wide range of substrate temperatures were selected for the growth of four films, as shown in

table 5.1. Results show that the magnetic moment of Co can exceed 2 $\mu_B$ even with cluster size larger than 20 nm. This work provides a new strategy to design high magnetization for heterogeneous DMSs with a nonrandom distribution of dopants.

**Table 5.1 Growth parameters of Co doped $TiO_2$ thin films.**

| Film number | Substrate temperature ($^oC$) | Deposition rate (nm/s) |
|---|---|---|
| 1 | 500 | 0.1 |
| 2 | 500 | 0.01 |
| 3 | 650 | 0.01 |
| 4 | 800 | 0.01 |

## 5.2 Results and discussion

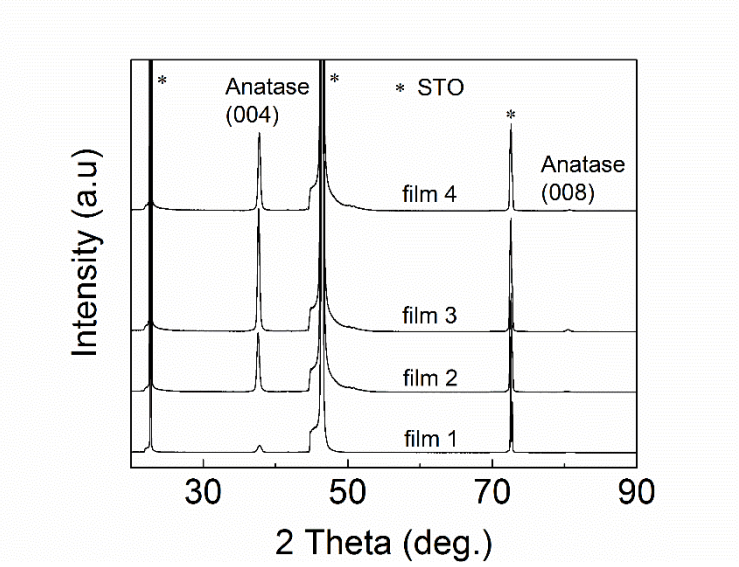


**Figure 5.1 XRD patterns of 5 at% Co doped $TiO_2$ films with different growth parameters.**

Figure 5.1 displays the XRD patterns of 5 at% Co doped TiO thin films deposited under various temperatures and speeds. Regardless of the difference in deposition temperature and rate, only diffraction peaks of anatase phase are observed in all the films. However, the intensity of (004) anatase peak of film 1 is almost 10 times lower than other three films, indicating high deposition rate can reduce the crystalline quality of $TiO_2$ films. The

peak becomes both higher and shaper with reduced growth rate and higher temperature, suggesting better degree of crystallinity under those conditions.

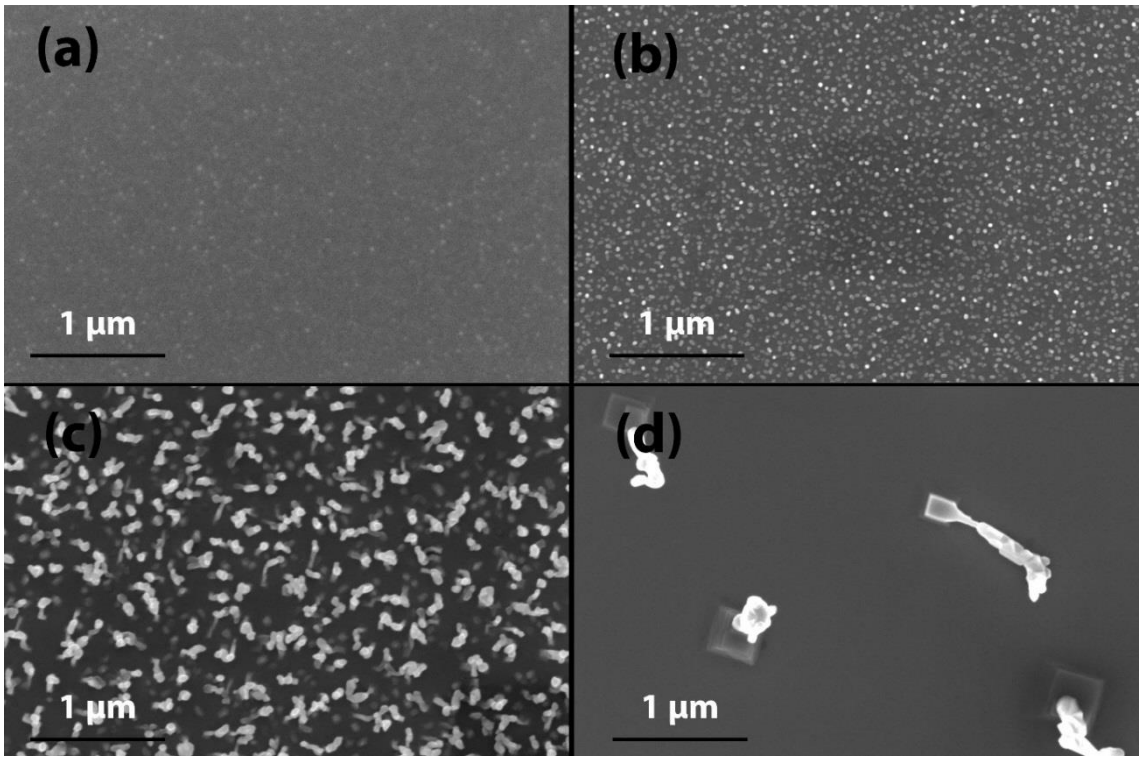


**Figure 5.2 SEM images of Co doped $TiO_2$ thin films, (a) film 1, (b) film 2, (c) film 3, and (d) film 4.**

Although all four films share the same crystalline structure, there are huge discrepancies among their surface morphologies. Only film 1 has a rather smooth surface, as shown in figure 5.2. With lower deposition rate, small nanoparticles with typical size of 30~40 nm begin to appear in film 2. As growth temperature rises, not only does the particle size remarkably enlarges, but the distance between neighbour particles becomes notably larger. The densely packed nanostructure vanishes when deposition temperature reaches 800 $^{o}$C as particles are separated by more than 1 micrometre and each particle is attached to a rectangular-shaped pyramid which should be the anatase grain. This sudden change of shape, from rectangular to irregular, is likely resulting from the change of surface energy due to Co aggregation at grain boundaries.

The surface morphology of the films is further demonstrated by AFM, as shown in figure 5.3. The root mean square (RMS) roughness of film 1 is smaller than 1 nm. The height of nanoparticles on film 2 and 3 lays in the range of 20-50 nm and 100-250 nm, respectively, while the particles on film 4 can even reach larger than 800 nm. It should be noted that this result is in direct contradiction to the conclusion in ref.[58], in which the epitaxial thin films with highest crystalline quality and most evenly Co distribution are deposited with a slow growth rate around 0.01 nm/s using MBE method. This total opposite tendency suggests the mechanism of film growth is very complex and may not have certain rules to guide the deposition.

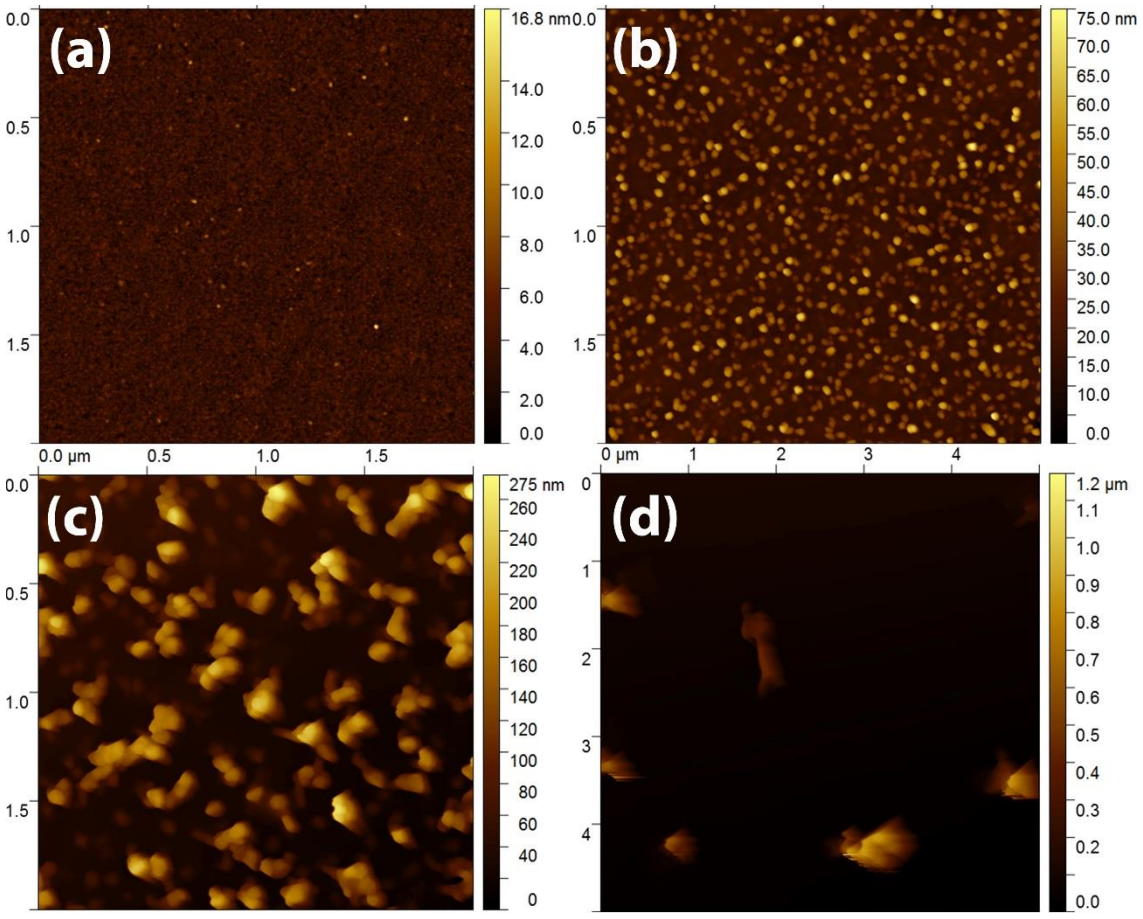


**Figure 5.3 AFM images of Co doped $TiO_2$ thin films, (a) film 1, (b) film 2, (c) film 3, and (d) film 4.**

Cross-section bright-field TEM images and SAED patterns of four thin films are presented in figure 5.4. In agreement with SEM and AFM, only film 1 has a rather smooth

surface. Film 2, 3 and 4 are mainly composed with a continuous anatase film plus various particles on top. SAED pattern of film 1 shows a polycrystalline feature, while the epitaxy gets better crystallinity when higher temperature and slower growing rate are applied.

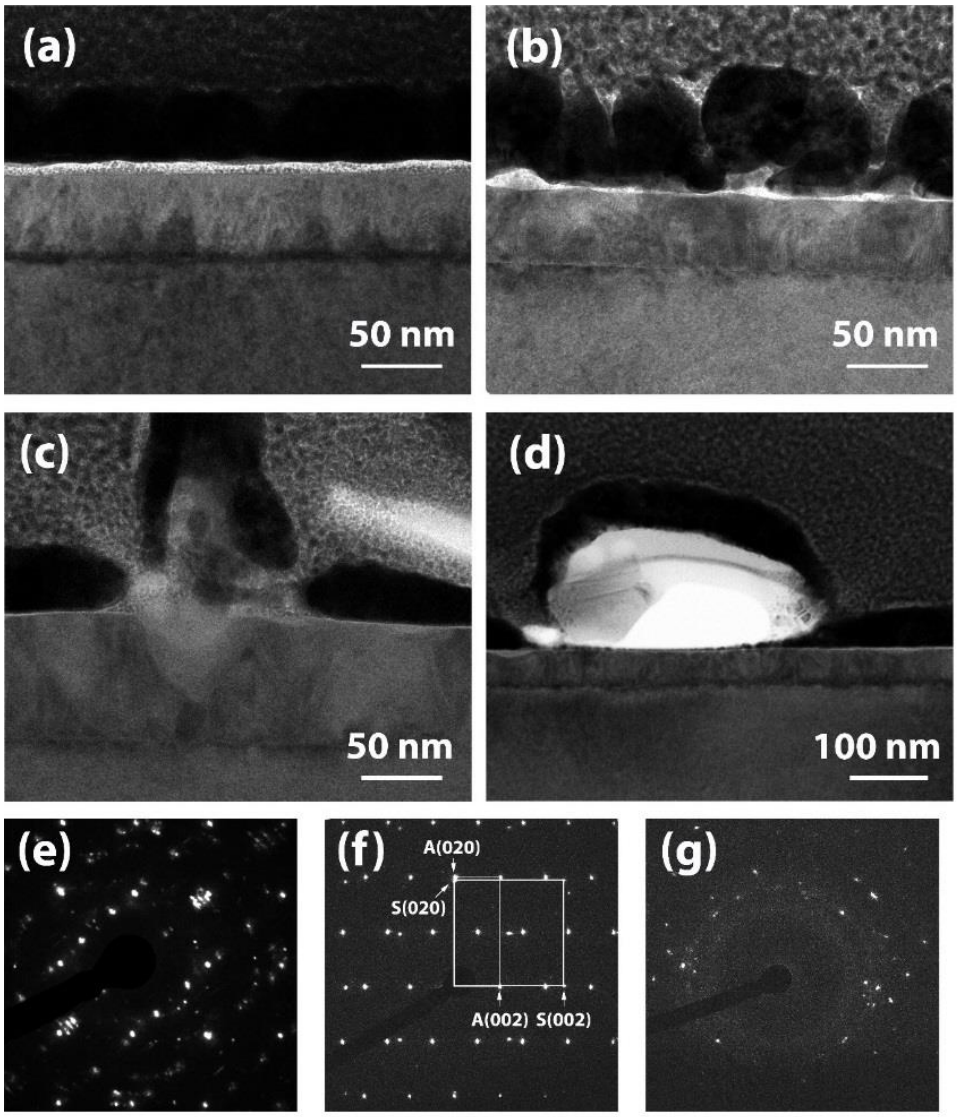


**Figure 5.4 TEM images of (a) film 1, (b) film 2, (c) film 3, and (d) film 4. SAED of (e) film 1, (f) the continuous film part of film 2, 3, and 4, and (g) the particles on the surface of film 3 and 4.**

From figure 5.4(f), the epitaxial relationship between film 2, 3, 4 and STO substrate are $[100]_{Anatase}||[100]_{STO}$, $[010]_{Anatase}||[010]_{STO}$ (in-plain), and $(001)_{Anatase}||(001)_{STO}$ (out-of-plain). We also observe that [020] Anatase and [020] STO do not overlap in SAED, which differs from the film grown on LAO substrate, as shown in figure 4.3. In epitaxial growth,

if the film is mismatched to the substrate, then the film is driven to match the substrate lattice in the lateral direction. Based on the degree of distortion, the film can be fully strained if the lateral film lattice is equal to the substrate, fully relaxed if the lattice parameters are identical to the bulk values, or in a partially strained intermediate state. Figure 5.5 displays the schematic diagram of strained and relaxed film. The lattice mismatch between anatase (001) and STO (001) is -3.1%, which is equal to the difference of [020] Anatase and [020] STO in figure 5.4(f), indicating the epitaxy is fully relaxed. SAED obtained from mere particles in film 3 and 4, as shown in figure 5.4(g), suggests the particles are polycrystals.

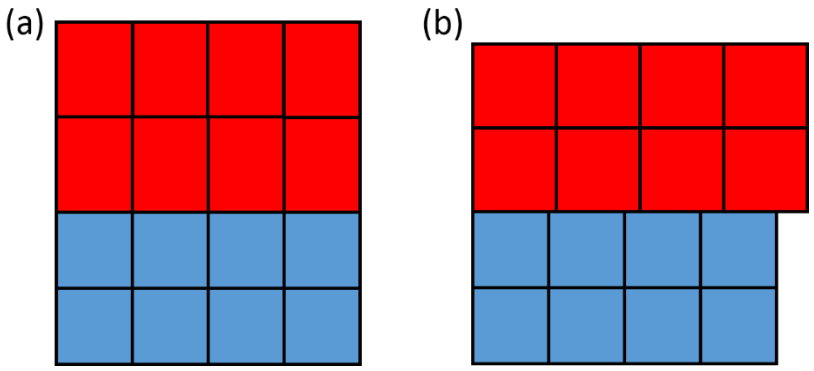


**Figure 5.5 A shematic diagram of (a) strained film and (b) relaxed film.**

The crystalline nature of films can be also obtained from the fast Fourier transform (FFT) of high-resolution TEM images, as shown in figure 5.6. While film 1 is polycrystalline, some regions (figure 5.6(b)) are better crystallized than others (figure 5.6(a)). Figure 5.6 (c) and (d) are places in film 2 near and away from the particle on the surface. It is observed both locations are single crystalline, but the points in the FFT of former area are not as sharp as those in the latter, indicating film structure near the particles suffers slight distortion. Both film 3 and film 4 are perfect single crystalline, as shown in figure 5.6 (e) and (f).

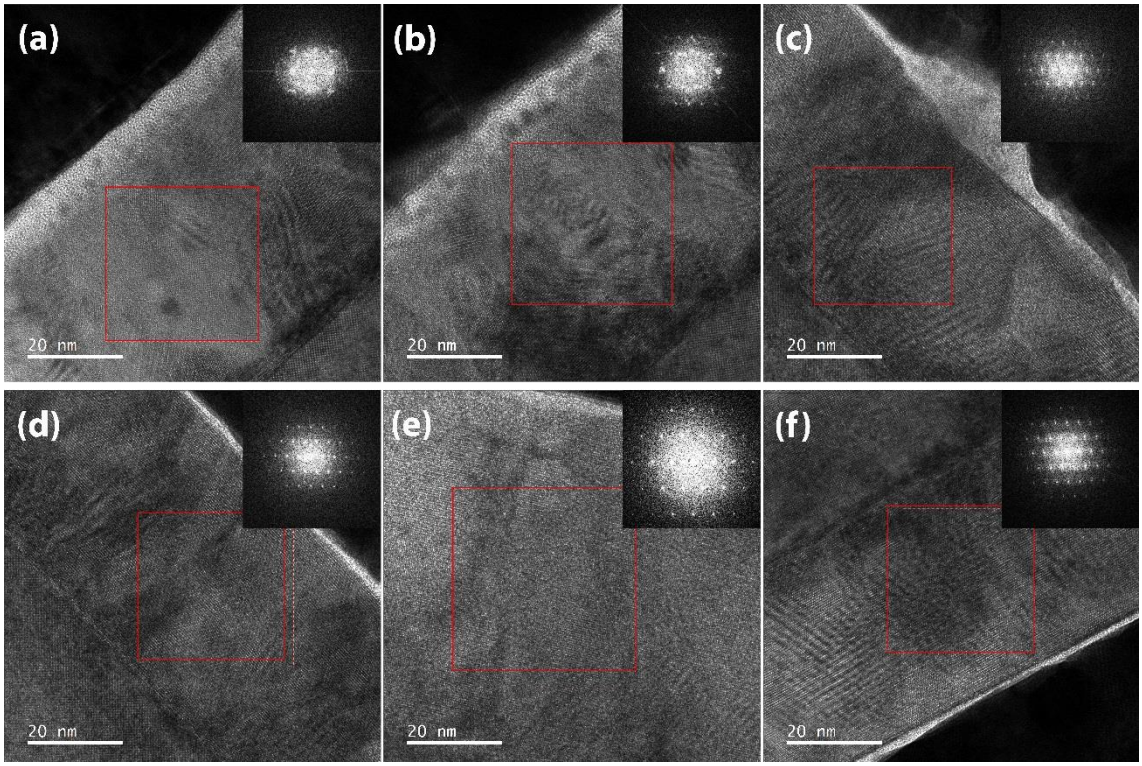


**Figure 5.6 HRTEM of Co doped $TiO_2$ thin films, insets are FFT images of the areas marked by red rectangular. (a) and (b) film 1, (c) and (d) film 2, (e) film 3, (f) film 4.**

EDS mapping and SIMS were carried out to examine the spatial distribution of the Co in the films, as shown in figure 5.7. Co tends to aggregate as nanoclusters near the interface in film 1, confirming by the intensity maximum near the interface in SIMS. In film 2, Co nanoclusters tend to grow bigger and migrate toward surface. Large clusters can be observed in the vicinity of the particles on film surface, while some nanoclusters still remain near the interface, as two peaks can be seen in the SIMS of film 2. Nearly all Co elements are blended into the surface particles in film 3, except for a minority of smaller clusters within the film near the particles. Therefore, the SIMS intensity in film 3 quickly reaches the maximum near the surface. Co can be hardly detected through EDS in film 4 (The red dots in figure 5.7(d) are from noises in gold and other elements). From cross-section view of TEM and SEM images, there is a hole inside nearly all the particles in film 4. This might be caused by evaporation of Co due to long-time exposure on the surface at high temperature, which explains the absence of Co dopants in EDS. In addition,

the extremely low SIMS intensity of film 4 also suggests Co may have been evaporated during deposition, at least to some extent. The schematic of film growth is illustrated in figure 5.8. In an early work, Chambers *et al.* investigated oxygen-plasma-assisted MBE grown Co doped anatase $TiO_2$ thin film at different growth rates and temperatures [58]. The epitaxial thin films with highest crystalline quality and most evenly dopant distribution were deposited at temperatures between 550-600 $^oC$ with a slow growth rate around 0.01 nm/s. However, similar parameters lead to Co segregation in our work, suggesting film growth is extremely sensitive to the equipment.

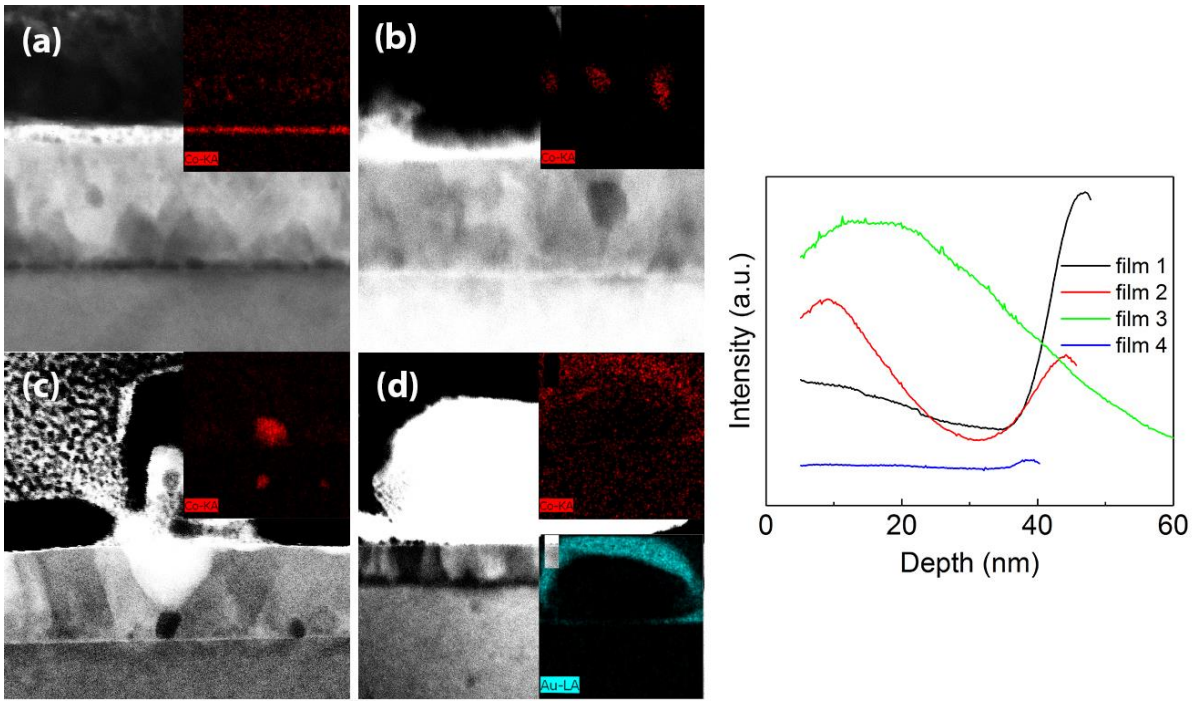


**Figure 5.7 ESD mapping of Co in the thin films (left). (a) film 1, (b) film 2, (c) film 3, (d) film 4. SIMS depth profiles for Co (right).**

The valence state of Co is of vital importance to the film's magnetic performance. Co 2p core-level XPS collected at the surface of film 2-4 show the characteristic peaks which can be ascribed to the 2+ valence state (Figure 5.9(a)), with strong satellite peaks and a spin-orbit splitting of ~16.0 eV. The Co 2p peaks of film 1 shifts to lower binding energy. In addition, the spectrum has a smaller spin-orbit splitting (~15.3 eV) and decreased satellite to main peak intensity ratio. These features indicate the appearance of $Co^{3+}$ ions

in film 1. As the cobalt precursor in the target is $Co_3O_4$, this suggests the growth condition of film 1 can prevent the reduction of $Co_3O_4$ at the surface. The peak intensity of film 4 is considerably lower than the other three, which is consistent with partial evaporation assumption. However, XPS can only collect signals of electrons that escape from the top layer of the films, resulting in a quite shallow characterization depth. To unveil the valence state of Co dopants in deeper layers, an argon ion beam was used to etch the films for 90 s to reach ~20 nm below original surface. The XPS spectra, as presented in figure 5.9(b), show totally different features compared to those taken at the surface. The sharp $Co^0$ peak is highly consistent with Co metal nanoclusters in $TiO_2$ grown on LAO investigated in last chapter. Therefore, $Co^{2+}$ can only be observed at the very surface, likely due to surface oxidation. Moreover, the clear $Co^0$ signal from film 4 suggests Co dopants cannot be totally evaporated.

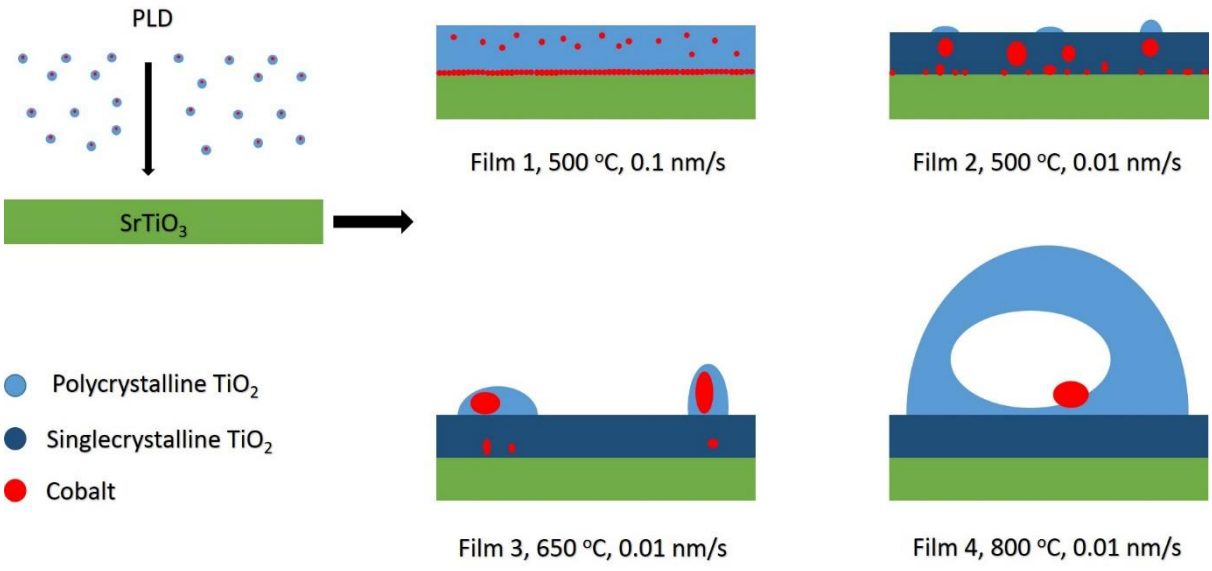


**Figure 5.8 Schematic of film growth during PLD.**

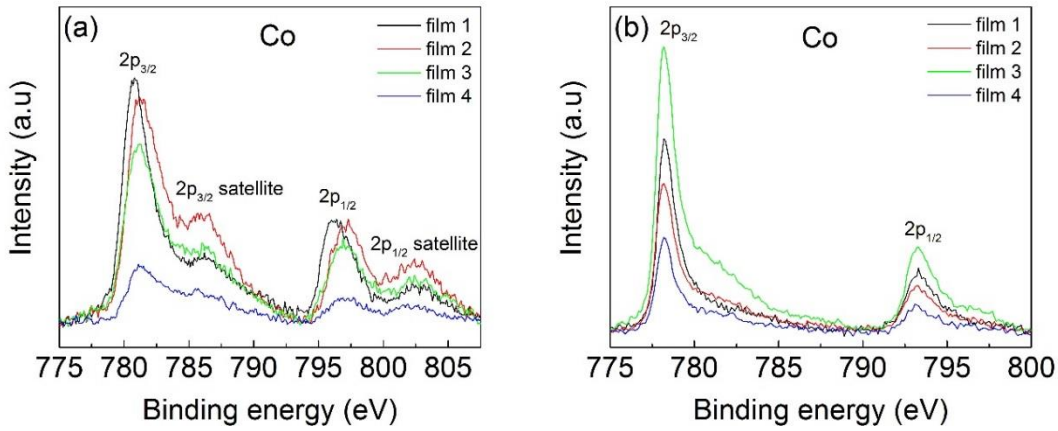


**Figure 5.9 XPS spectra of Co doped $TiO_2$ thin films: (a) original surface, (b) after 90s ion-beam etching.**

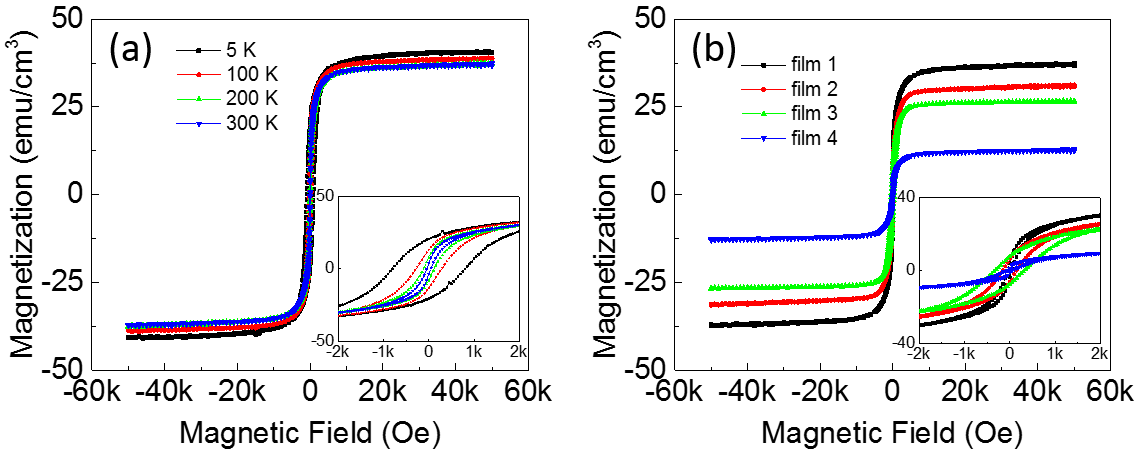


**Figure 5.10 (a) M-H loops of film 1 measured at different temperatures. (b) M-H loops of four thin films measured at room temperature.**

The hysteresis loops of film 1 measured at various temperatures are shown in figure 5.10(a). The film shows obvious ferromagnetic features with a Ms of 40.5 emu/cm$^3$ at 5 K. The ferromagnetic ordering is further confirmed by the coercivity of the M-H loops, as shown in the inset. Increasing the temperature does not lead to a dramatic drop in Ms, which remains mostly at the same level of 36.9 emu/cm$^3$ above 200 K. The persisted Ms to 300 K suggests the Tc of the film is above room temperature. Considering the entire magnetic moment is contributed by Co, the dopant has a magnetic moment of 2.49 $\mu_B$/Co at room temperature. Figure 5.10(b) shows the hysteresis loops of different films at room

temperature, with the Ms constantly decreases from film 1 to 4. Despite the reduced Ms, film 2 and 3 have significantly enlarged coercivity compared to film 1, as shown in the inset of figure 5.10(b). The coercivity of film 3 measured at low temperature is even larger, reaching ~1k Oe.

It is well acknowledged that the presence of Co clusters gives rise to ferromagnetism persisted to above room temperature in inhomogeneous films. It is further confirmed with recent polarized neutrons reflectometry results that magnetization merely originates from Co-rich regions and shares similar in-depth pattern to Co concentration [179]. However, magnetic moments induced by Co nanoclusters can hardly reach above 2.5 $\mu_B$/Co regardless of the states of the clusters, including Co clusters embedded in Cu and $SiO_2$ matrixes, and free-standing clusters measured via molecular beam deflection [153, 180]. With very small sizes (fewer than 30 atoms), Co shows atom-like magnetic moments (~2.4 $\mu_B$/Co), which decrease toward the bulk limit with increased cluster size. According to first principles calculation, magnetic moments of free Co clusters can vary based on different geometries, but all below 2.6 $\mu_B$/Co [181, 182]. Other Co nanostructures, such as nanowire arrays, generate similar magnetic moments [183]. Magnetic moments between 3-4 $\mu_B$/Co have only been reported in ultra-small free Co nanoclusters with less than 20 atoms at extremely low temperature, contributed from extra unquenched orbital moments [184-186]. However, such moments are significantly reduced with increased cluster size and temperature. Furthermore, whether the enhanced moments can persist after dispersing in a matrix remains doubtful as interactions between ultra-small magnetic particles frequently lead to superparamagnetic or spin-glass behaviours [160, 187]. The magnetic moments observed in our Co-doped $TiO_2$ (2.49 $\mu_B$/Co in film 1) is consistent with previous studies. Furthermore, although most Co clusters observed in film 2 have diameters in the range of 10-20 nm, the film still shows a Ms higher than 2 $\mu_B$/Co,

indicating the Ms may be more sensitive to the distribution of Co clusters than the mere size. The thin films can only maintain high magnetic moments when Co clusters are distributed inside the films, demonstrated by the sharp drop of Ms in film 4. Moreover, it is believed a variety of defects, such as $Ti^{3+}$ ions and oxygen vacancies, can also induce magnetic moments [149, 188, 189]. Thus, the high magnetization is likely attributed to the combination of Co nanoclusters and various defects.

## 5.3 Conclusions

Controllable formation of Co nanoclusters embedded in $TiO_2$ are achievable through pulsed laser deposition on $SrTiO_3$ (001) substrate. The film is polycrystalline with high deposition rate at 500 $^oC$, in which Co segregates into small clusters at the interface. When grown at slow rate and high temperatures, fully relaxed epitaxial films are obtained. Meanwhile, the Co nanoclusters increase in size with increasing temperature and move toward surface, causing the formation of nano- and even micro- particles on the surface. XPS result suggests that the Co dopants mainly exist as $Co^0$, which is consistent with the film grown on LAO. SQUID measurement shows a highest magnetic moment of 2.49 $\mu_B$/Co at room temperature. Although the magnetic properties are sensitive to the size and distribution of Co nanoclusters, large magnetization can still be achieved by Co nanoclusters with size bigger than 20 nm. A part of the high magnetic moments may originate from Ti and O defects.

# Chapter 6 Defect Engineering and Magnetic Properties of TMDCs

## 6.1 Overview

2D materials with atomic thickness have attracted considerable attention since the discovery of graphene, the monolayer counterpart of graphite. Currently, graphene is still the most eminent 2D material due to its extraordinary electrical mobility at room temperature (larger than $1\times10^5$ $cm^2V^{-1}s^{-1}$), Young's modulus of 1 TPa and intrinsic strength of 130 GPa [190, 191]. However, the lack of nonzero bandgap seriously limits its application in logical circuits where a high on/off current ratio is required [192]. Although several techniques, such as chemical doping or strain modulated bilayer graphene, have been proposed to manually introduce a bandgap into graphene, these modifications inevitably yield either low electrical conductivity or complex design [193, 194]. Inspired by graphene, there has been renewed interest in materials with layered structure, including transition metal dichalcogenides (TMDs), transition metal oxides (TMOs), boron nitride and silicene, *etc* [195-198].

Using top-down or bottom-up approaches to fabricate 2D TMDs similar to those of graphene, 2D TMDs can be synthesized via a wide variety of methods, including mechanical and chemical exfoliation, chemical solution deposition, chemical and physical vapor deposition. TMD materials have demonstrated outstanding performances in the field of hydrogen evolution reaction, energy storage, diagnostic imaging, electronic and optoelectronic devices, leading to extensive studies involving both theoretical and experimental research [199-202]. However, the magnetic properties of layered TMDs remain less explored compared to the electronic and optical properties. Theoretical

studies based on first-principles calculations reveal a nonmagnetic ground state of perfect crystalline $MoS_2$ [120, 203]. Ferromagnetism can be introduced into $MoS_2$ by strain, the formation of vacancies, zigzag edges in nanoribbons, doping with transition metals, and edge passivation [204-207]. While some simulations are straightforward, others are very complex. For example, the magnetic moment of zigzag $MoS_2$ nanoribbons decreases when only one edge is passivated with C, but increases with passivation of both edges [208].

The vast majority of studies related to TMDs so far focus on $MoS_2$. Compared to $MoS_2$, $WS_2$ has advantages over thermal stability and electrical properties. Like $MoS_2$, $WS_2$ nanosheets also display room-temperature ferromagnetism [209]. First-principles simulations indicate the magnetic state of $WS_2$ can be modulated by defects and transition metal doping [210-213]. Recently, robust valley polarization and valley polarization coherence, due to giant spin-orbit coupling and spin-valley coupling, have been observed in bilayer $WS_2$, making it a promising candidate for spintronics and valleytronics devices [214].

Rare earth element has played important roles in the properties of magnetic materials for its strong spin-orbit coupling [215, 216]. Nd is a well-known rare earth element that can effectively tailor the electrical and magnetic properties of semiconductors like ZnO and $TiO_2$ [217-219]. Evidence indicates that Nd-doped ZnO nanoparticles show enhanced photoluminescence and ferromagnetic properties compared to bare ZnO [220]. Moreover, high coercivity and magnetization have been observed in Nd doped ZnO nanowires [221]. So far, however, there is no theoretical or experimental work of Nd doped TMDC materials.

In this work, demonstrations were made to manipulate the magnetic properties of TMDCs

by defect engineering. Firstly, vacancies were introduced into $WS_2$ powders by heat treatment. $WS_2$ powders (99.9%) were purchased from Zaibang Chemical Industry CO., LTD, China. Annealing was carried out in a tube furnace and alumina crucible was used to transfer $WS_2$ powders into the center of the furnace. The furnace was purged by forming gas (5% Hydrogen, 95% Argon) for half an hour prior to annealing, then it was heated up to annealing temperature (400 $^oC$, 700 $^oC$ and 1000 $^oC$) by a rate of 5 $^oC$/min with continuous gas flow of 50 sccm. The annealing time was 1 h and the annealed samples were labeled as 400-$WS_2$, 700-$WS_2$, and 1000-$WS_2$. In the second part, Nd with different concentrations was doped into $MoS_2$ single crystals. The ion implantation took place at GNS Science, New Zealand. A low-energy ion implanter was used with a voltage of 30 keV at a fluence of $5\times10^{14}$, $1\times10^{15}$, $4.8\times10^{15}$ Nd-ions/$cm^2$. The projected range was set to ~12.6 nm and the average concentrations of Nd over 50 nm are 0.5, 1, 5 at%, respectively. It was found that annealing and ion implantation both lead to enhanced ferromagnetism by the formation of defects. Defect density, which is strongly dependent on annealing temperature and Nd dose, plays a crucial role in the magnetic behaviors of $WS_2$ and $MoS_2$.

## 6.2 Magnetic properties of annealed $WS_2$ powders

The XRD patterns of pristine and annealed $WS_2$ samples are presented in figure 6.1. The shape of the patterns indicates a mixture of hexagonal 2H phase ($P6_3/mmc$) and the rhombohedral 3R phase (R3mH). Analysis of phase content was carried out via Rietveld refinement approach built in HighScore Plus software. The proportions of 2H phase in four $WS_2$ samples vary from 45.8% to 47.2%, almost identical. This suggests annealing has little impact on the composition of $WS_2$ powder. The SEM images of the pristine and annealed $WS_2$ powders are shown in figure 6.2. It reveals that annealing process has little

impact on the powder morphology. All samples consist of micro-sized particles accumulated by various forms of nanostructured $WS_2$. Thin $WS_2$ nanosheets and irregular nanoparticles can be observed in the samples, as well as nanorods with a width of around 500 nm and length of several micrometers.

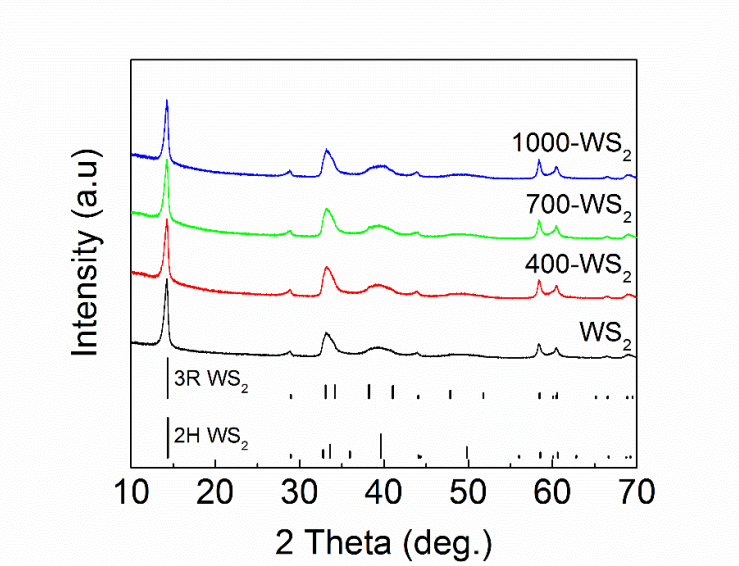


**Figure 6.1 XRD spectra $WS_2$ powders annealed at different temperatures.**

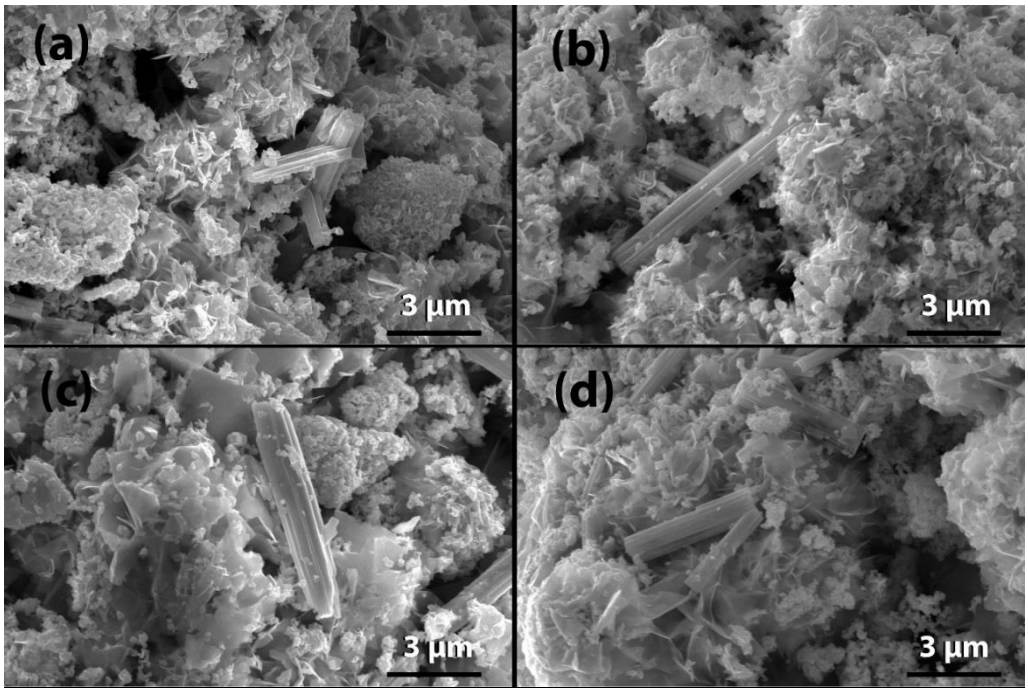


**Figure 6.2 SEM images of $WS_2$ powders, (a) pristine $WS_2$, (b) 400-$WS_2$, (c) 700-$WS_2$, (d) 1000-$WS_2$.**

Raman spectroscopy has emerged as a powerful non-destructive method to explore various properties of 2D TMDs such as $MoS_2$ and $WS_2$. For example, the layer numbers, as well as doping conditions of 2D flakes, can be derived from peak shifts of the first-order $E^1_{2g}$ and $A_{1g}$ optical modes [222]. As presented in figure 6.3, $WS_2$ powders have two dominated Raman peaks. The peak at ~420 $cm^{-1}$ corresponds to out-of-plane vibrational $A_{1g}$ mode, whereas the peak at ~350 $cm^{-1}$ is the result of the overlapping of in-plane vibrational $E^1_{2g}$ mode and longitudinal acoustic 2LA mode. The thickness $WS_2$ can be identified by analysing the frequency differences between the $A_{1g}$ and $E^1_{2g}$ modes. In our case, the frequency difference of 70 $cm^{-1}$ matches the value of bulk $WS_2$ [223]. Previous studies also suggest that $A_{1g}$ mode of $MoS_2$ shows blue/red shift by p/n-type doping while the $E^1_{2g}$ mode remains at the same position [224, 225]. Annealing can induce sulfur vacancies due to sulfur decomposition at high temperatures, which introduce unpaired electrons and n-type doping [226]. Tiny red shifts can be seen from $A_{1g}$ modes in 400-$WS_2$ (419.98 $cm^{-1}$) and 700-$WS_2$ (419.91 $cm^{-1}$) compared to pristine $WS_2$ (420.23 $cm^{-1}$) and 1000-$WS_2$ (420.33 $cm^{-1}$) as shown in figure 6.3(b), but the shifts are too small to confirm the n-doping effect.

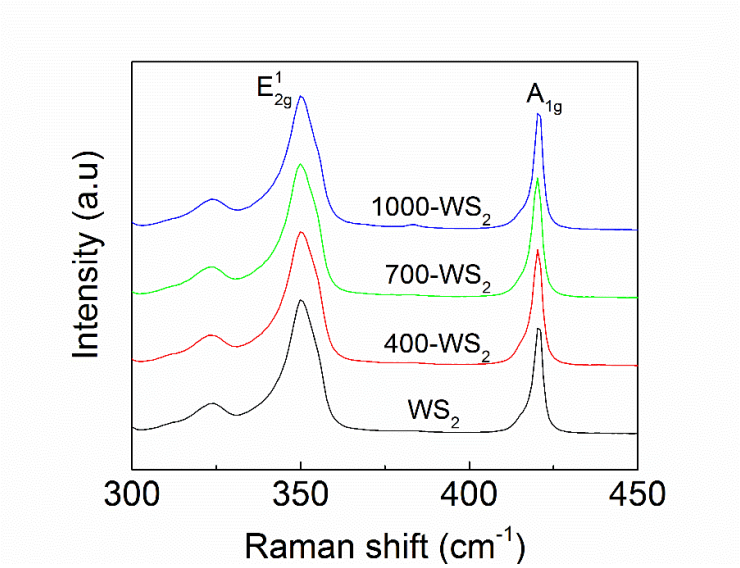


**Figure 6.3 Raman spectra of $WS_2$ powders.**

XPS is sensitive to chemical composition and stoichiometry of $WS_2$ powders. The binding energy profiles for W 4f are illustrated in figure 6.4(a). Three peaks observed at 33.6, 35.8, and 39.4 eV of untreated $WS_2$ powders are attributed to the W $4f_{7/2}$, W $4f_{5/2}$, and W $5p_{3/2}$, respectively. The positions of these peaks demonstrate a 4+ valence state of W from pure $WS_2$ phase, which is consistent with other reports for $WS_2$ crystals [227]. Compared to pristine $WS_2$ powder, all annealed powders exhibit certain peak shift. 400-$WS_2$ and 700-$WS_2$ display a shift to the lower binding energy side. It is an evidence of the redistribution of localized charges due to the formation of sulfur vacancies, which agrees with studies of sulfur vacancies in $MoS_2$ [228]. Recent studies have shown that hydrogen annealing below certain temperature can lead to both micrometer and nanometer-scale holes, while large cracks and even sample decomposition are expected at high temperature [229]. These may explain the back-shift of W4f peaks of 1000-$WS_2$. From figure 6.4(b), a similar trend can be observed for S $2p_{1/2}$ and S $2p_{3/2}$ doublet with binding energy of ~163.3 and ~164.4 eV. Furthermore, an increase of vacancy density in annealing samples is also demonstrated by ESR spectra. As shown in figure 6.5, the paramagnetic signals around $g \approx 1.977$ in ESR first increase and reach the maximum by 700-$WS_2$, then drop to bottom. The ESR result provides further proof of the existence of sulfur vacancies as anion vacancies can provide unpaired electrons [230]. The low ESR intensity of 1000-$WS_2$ indicates annealing at 1000 $^oC$ has negative effects on sulfur vacancy generation, possibly caused by structure disruption, which agrees with XPS results.

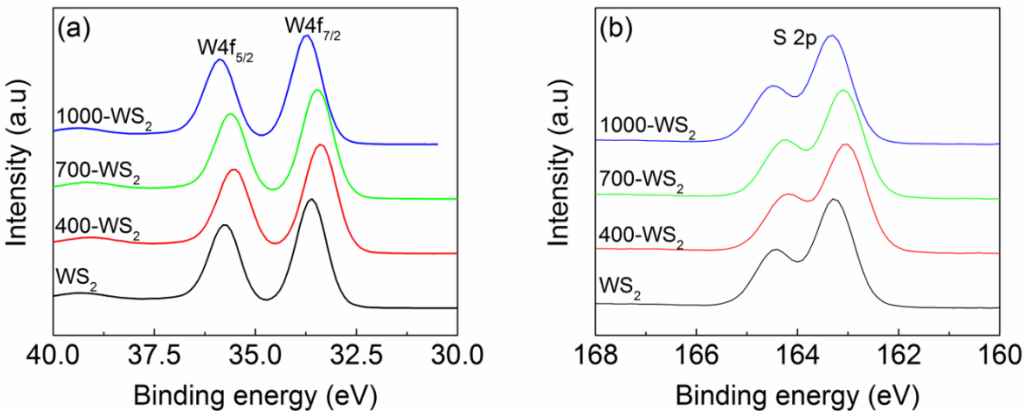


**Figure 6.4 XPS core-level spectra of (a) W4f and (b) S2p.**

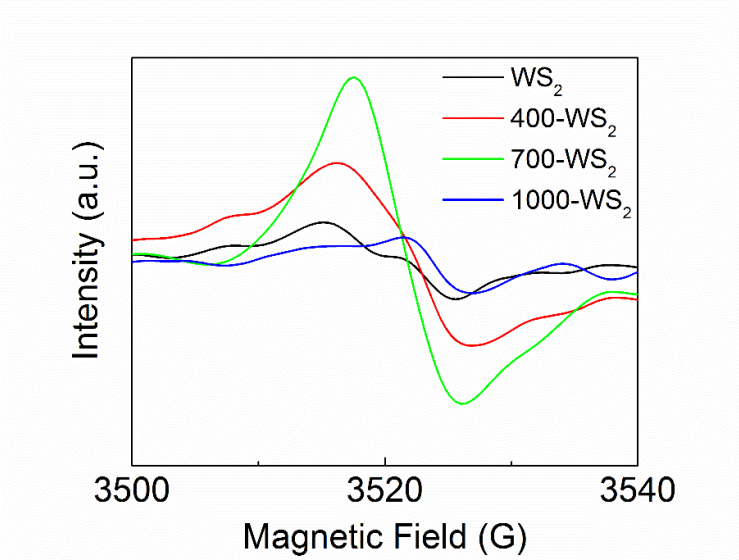


**Figure 6.5 Room-temperature EPR spectra of $WS_2$ samples.**

The magnetization versus applied field (M-H) loops of different $WS_2$ powders are shown in figure 6.6. Unlike bulk $WS_2$ crystals with merely diamagnetic nature, all $WS_2$ powders present clear additional ferromagnetic features at 5 K. The ferromagnetism can be attributed to various dangling bonds or vacancies. Further first-principles calculations indicate that the ferromagnetic ordering can be realized in the 2D network of dangling bonds, and collapses if the dangling bonds are saturated by H ions [231]. After annealing, the magnetization of $WS_2$ powders significantly increases, with the highest magnetization achieved by 700-$WS_2$ taken at 5 K as shown in figure 6.6(e). Although diamagnetic signals dominate the magnetic response when the temperature reaches above 50 K, ferromagnetic hysteresis loop can still be observed above the diamagnetic background up to room temperature. After deducing the diamagnetic part, the ferromagnetic loops of four powders measured at room temperature are illustrated in figure 6.6(f). 700-$WS_2$ still

shows the highest saturation magnetization (Ms) with ~0.002 emu/g. 1000-$WS_2$ seems to possess the second-best room-temperature Ms, but its zero coercivity indicates non-ferromagnetic phase.

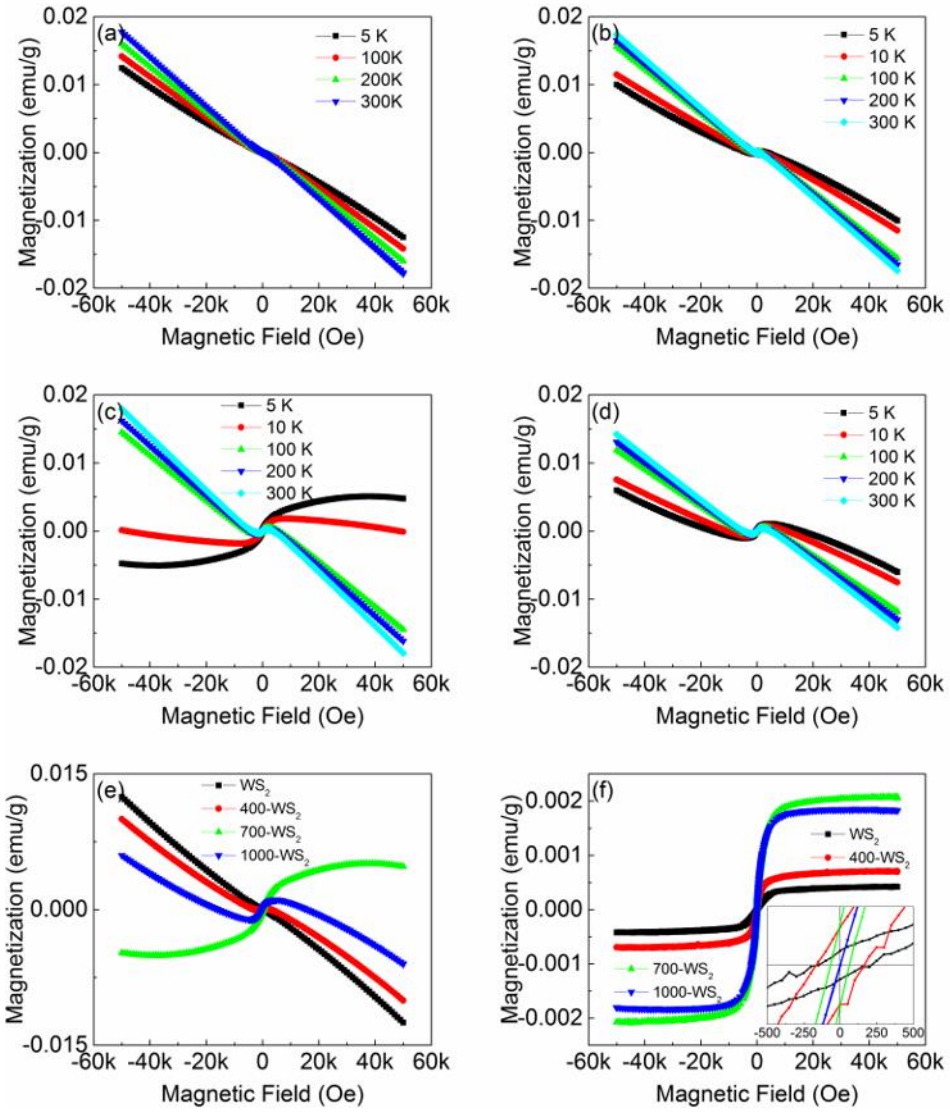


**Figure 6.6 M-H measurement of (a) original $WS_2$, (b) 400-$WS_2$, (c) 700-$WS_2$ and (d) 1000-$WS_2$ measured at different temperatures. (e) M-H loops of different $WS_2$ powders measured at 5 K. (f) Hysteresis loops obtained by deducting the diamagnetic signal, measured at 300 K. The inset is the loops in a small field range.**

According to first-principles calculations, the ferromagnetism arising from nanostructured TMDs is mainly contributed by defects, either point defects like vacancies or one-dimensional defects such as edges and grain boundaries. In several studies of defect-induced ferromagnetism in $MoS_2$ [106, 232], authors claimed that the induced

ferromagnetic ordering is due to the exchange interactions between sulfur vacancy and the $Mo^{4+}$ 4d bandgap state. For $WS_2$, while simple vacancies like single tungsten and sulfur vacancies ($V_W$ and $V_S$) are non-magnetic, a number of complex vacancies, such as three-tungsten vacancy ($V_{3W}$), six-sulfur vacancy ($V_{6S}$) and 1W+2S vacancy ($V_{1W+2S}$), show ferromagnetic behaviours caused by the S p states and W d states near vacancy defects [233].

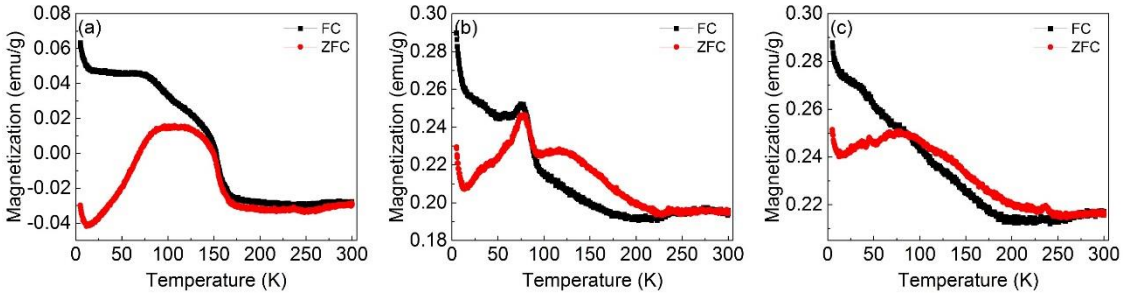


**Figure 6.7 ZFC and FC curves of (a) 400-$WS_2$, (b) 700-$WS_2$ and (c) 1000-$WS_2$. The magnetic field applied is 500 Oe.**

From XPS and ESR, annealing below 1000 $^oC$ can increase the density of vacancies, leading to higher magnetization. Further increase in annealing temperature can disrupt $WS_2$ structure and destroy ferromagnetic ordering. Figure 6.7 displays zero field cooling (ZFC) and field cooling (FC) curves of annealed $WS_2$ powders. The relatively high magnetization below 15 K suggests the presence of paramagnetic phase. It is obvious there is a phase transition around 75 K for all samples, although it is unreported in previous studies. $WS_2$ annealed at various temperatures show totally different curve features near the transition point. ZFC/FC curves of 400-$WS_2$ show a broad transition range between 75 and 150 K. ZFC/FC curves of 700-$WS_2$ and 1000-$WS_2$ intercross near the critical temperature and FC curve continues to decrease below ZFC curve. This negative irreversible magnetization is often observed in random-field systems [234]. The defects and impurities are the sources of random field. In the model, even weak random fields can destroy long-range order. For $WS_2$ annealed at high temperatures, $WS_2$ tends

to decompose into small nanosheets and create massive defects like edges and boundaries, which has drastic effects on phase transitions. The random field generated from the defects compete with the long range ferromagnetic order. Imry and Ma first suggested the possibility that the ordered state could be broken up into certain sized domains [235]. The absence of long-range ferromagnetic ordering has later been explained by domain wall pinning in metastable states [236]. This might be the cause for the disappearance of ferromagnetism in 1000-$WS_2$, but the exact random field induced disordering mechanism in a disordered ferromagnet is still under debate. Moreover, hydrogen passivation may have some impacts on the magnetization as hydrogen adsorption can be observed on $MoS_2$ and $WS_2$ [237, 238]. However, theoretical studies have predicted extremely complex magnetic properties of $WS_2$ nanoribbons with edge hydrogenation [239]. Therefore, we have not taken hydrogen passivation into consideration.

## 6.3 Magnetic properties of Nd-doped $MoS_2$ single crystals

Figure 6.8(a) displays the XRD patterns of pure and Nd-doped $MoS_2$ with various Nd concentrations. All diffraction peaks of the pure $MoS_2$ crystal have indexes parallel to the [001] orientation of hexagonal $MoS_2$ (P63/mmc), showing a perfect single crystal structure. No peaks of any other impurities are detected for 0.5 at% and 1 at% Nd-doped $MoS_2$, indicating that no secondary Nd phases are generated during ion implantation. An extremely weak peak emerges at $22.16^o$ for 5 at% Nd-doped $MoS_2$ with intensity of 32 compared to $1.56 \times 10^6$ of the main peak, which may belong to the (002) diffraction peak of $NdS_2$.

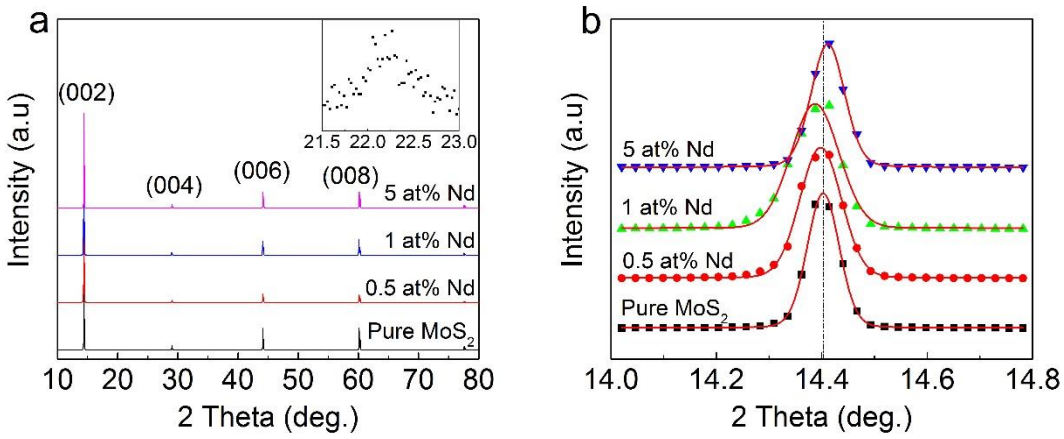


**Figure 6.8 (a) XRD patterns of undoped and Nd-doped $MoS_2$ crystals. The inset shows $NdS_2$ peak in 5 at% Nd-doped $MoS_2$. (b) Enlarged (002) diffraction peaks.**

(002) diffraction peaks of 0.5 at% and 1 at% Nd-doped $MoS_2$ shift towards lower diffraction angle as compared to undoped $MoS_2$ crystal (As shown in figure 6.8(b). All peaks are fitted using a pseudo-Voigt function), demonstrating a lattice constant expansion. The enlargement of the lattice parameters is caused by the ionic radius difference between dopant and matrix atoms. Because $Nd^{3+}$ (0.98 Å) has a larger radius than $Mo^{4+}$ (0.65 Å), the expansion suggests that $Nd^{3+}$ ions replace the $Mo^{4+}$ lattice or stay in interstitial sites. Although the (002) diffraction peak of 5 at% Nd-doped $MoS_2$ has the highest diffraction angle, its lattice parameter *a* (3.172 Å) obtained through refinement is still slightly larger than 0.5 at% Nd-doped $MoS_2$ (3.168 Å) and pure $MoS_2$ (3.167 Å) but less than that of 1 at% Nd-doped $MoS_2$ (3.186 Å). The abnormal lattice parameters of 5 at% Nd-doped $MoS_2$ in contrast to its highest dopant concentration can be explained by the secondary Nd phase and abundant surface vacancies which may distort unit cells. Another intriguing finding is that the expansion of unit cell is anisotropic. The relative variation along c-axis is less than one tenth of that along a-axis, suggesting the cell is mainly stretched in the preferred in-plane direction during the doping.

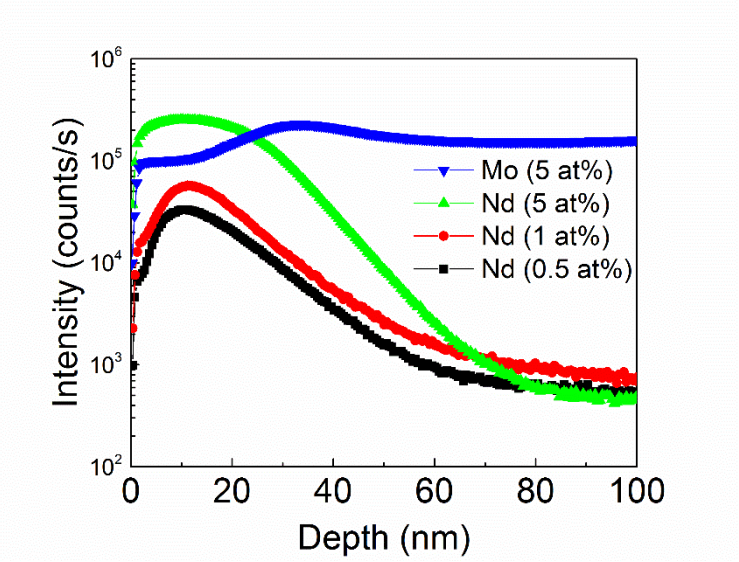


**Figure 6.9 SIMS depth profiles for Nd element in three doped crystals and Mo in 5 at% Nd-doped $MoS_2$.**

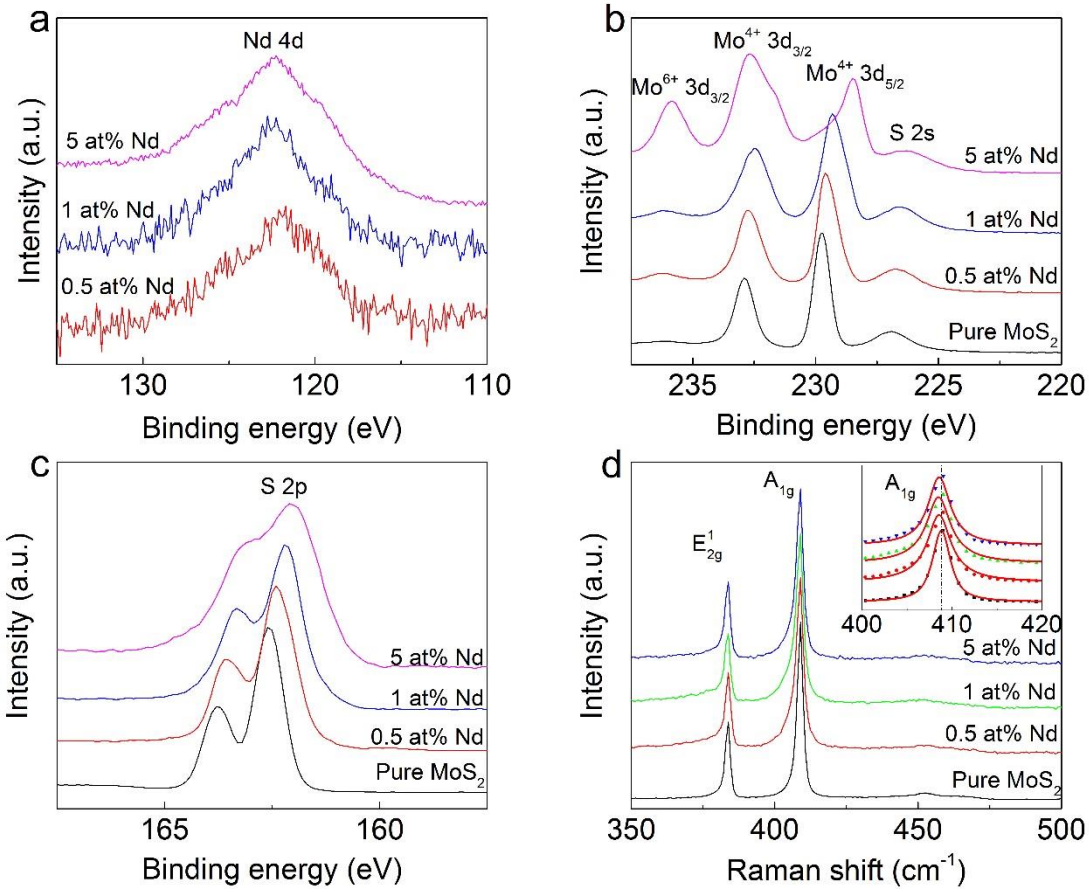


**Figure 6.10 XPS core-level spectra of (a) Nd 4d, (b) Mo 3d and S 2s and (c) S 2p for pure and Nd-doped $MoS_2$ crystals. (d) Raman spectra of $MoS_2$. The inset is enlarged $A_{1g}$ modes with peak fittings.**

The distribution of Nd dopants in $MoS_2$ is examined by SIMS, as presented in figure 6.9.

Rather than uniformly distributed within the top 50 nm, the depth profiles can be approximated as Gaussian function with the centre located around 12.6 nm, which is well agreed with the projected range. However, this also means most Nd dopants only accumulate in a restrict space with near double concentration than the original design. Take 5 at% Nd-doped $MoS_2$ for example, the concentration can reach 10 at% within the top 20 nm. Such high concentration may be the cause for the formation of secondary phase.

During the ion implantation, some defects are inevitably introduced into $MoS_2$ crystals because the energy of Nd implantation (30 keV) is far above the formation energies of various kinds of defects, especially the sulfur vacancy with a formation energy as low as ~6.0 eV [122]. Therefore, we investigated the $MoS_2$ crystals before and after ion implantation via XPS to identify possible defects. The first concern is to determine the valence of Nd element. However, high-resolution scan finds no trace of Nd on the surface of 0.5 at% Nd-doped $MoS_2$. Distinct Nd 4d core-level signal with concentration of 1.1 at% can only be observed after 30s ion-beam etching to reach depth below 10 nm, confirming the Gaussian distribution of Nd from SIMS (figure 6.10(a)). From XPS, 1 at% Nd-doped $MoS_2$ also displays higher Nd concentration (1.4 at%) after etching than the original surface (0.64 at%). 5 at% Nd-doped $MoS_2$ is an exception. Its original surface has an unexpectedly higher dopant concentration (19.1 at%) than post-etching (18.3 at%) and both values considerably exceed the estimation from SIMS. This suggests doping with heavy dose can even cause Mo ions to escape from surface, supported by the SIMS depth profile of Mo in 5 at% Nd-doped $MoS_2$, in which the intensity of top 10 nm is only ~60% compared with that of 100 nm. The peak position of Nd around 122.1 eV in 0.5 at% Nd-doped $MoS_2$ indicates Nd mainly exists as $Nd^{3+}$ ions [240, 241]. However, binding energy decreases with increased doping concentration, to ~122.9 eV for 5 at% Nd-doped $MoS_2$,

which suggests the possible formation of $Nd^{4+}$ ions and agrees with the appearance of $NdS_2$ in XRD pattern.

Figure 6.10(b) and (c) show the high-resolution Mo 3d and S 2p core-level XPS spectra. The characteristic peaks of $Mo^{4+}$ $3d_{3/2}$ and $Mo^{4+}$ $3d_{5/2}$ doublet of pure $MoS_2$ locate at 232.9 eV and 229.7 eV, which shift to the lower binding energy side after Nd doping. The peak shifts of $Mo^{4+}$ $3d_{3/2}$ and $Mo^{4+}$ $3d_{5/2}$ orbitals for 0.5 at% Nd-doped $MoS_2$ are around 0.2 eV and 0.3 eV, respectively, and further shifts can be observed for $MoS_2$ crystals with higher dopant concentration. In previous studies, it is proposed that the $Mo^{4+}$ $3d_{5/2}$ and $Mo^{4+}$ $3d_{3/2}$ peaks can be split into two parts: one part of intrinsic $MoS_2$ and another part of $MoS_2$ containing sulfur vacancies [242]. The spectra of vacancy-containing $MoS_2$ appear at lower binding energies compared to the intrinsic $MoS_2$ part due to the redistribution of charges localized on the more electronegative sulfur atoms to the first neighbouring atoms (Coulomb screening effect) [228]. Therefore, the peak shifts to the lower binding energy side can be considered as a sign of sulfur vacancies. The XPS spectra of $S^{2-}$ $2p_{3/2}$, $2p_{1/2}$, and 2s have similar feature to Mo 3d, with the peaks to the lower binding energy region as the dopant concentration increases. The sulfur deficiency is further confirmed by the calculation of atomic ratio of S/Mo obtained from XPS spectra. The S/Mo ratio decreases from 2.24 in pure $MoS_2$ single crystals to 1.82 and 1.80 in 0.5 and 1 at% Nd-doped $MoS_2$, which further drops to mere 1.09 in 5 at% Nd-doped $MoS_2$.

In addition to peak shift, a prominent peak at ~235.7 eV shown up in figure 6.10(b) is attributed to the $Mo^{6+}$ state. Although $Mo^{6+}$ also contains double peaks like $Mo^{4+}$, the $3d_{5/2}$ peak at lower binding energy is entirely covered by the $Mo^{4+}$ $3d_{3/2}$ peak when $Mo^{6+}$ ions only occupy a small proportion, like in 0.5 and 1 at% Nd-doped $MoS_2$. This $Mo^{6+}$ peak has been observed in previous reports, which is explained by absorption of oxygen [242, 243]. The loss of Mo atoms on the surface may be another cause for the strong $Mo^{6+}$

peak observed in 5 at% Nd-doped $MoS_2$.

Raman spectroscopy has emerged as a powerful non-destructive means to examine the structure of $MoS_2$. As shown in figure 6.10(d), the peak at ~383.47 $cm^{-1}$ corresponds to $E^1_{2g}$ mode due to the displacement of Mo and sulfur atoms within the basal plane, whereas the $A_{1g}$ mode at ~408.82 $cm^{-1}$ originates from the vibration perpendicular to the basal plane. Several studies suggest that $A_{1g}$ mode of $MoS_2$ is considerably sensitive to doping while the $E^1_{2g}$ mode is almost inert. A p/n-type doping can cause $A_{1g}$ peak to blue/red shift because of strong electron-phonon coupling [224, 225]. From Raman spectra, a small red shift of ~0.3 $cm^{-1}$ can be observed for $A_{1g}$ mode of Nd-doped $MoS_2$ crystals, indicating n-type doping. Theoretically, $Nd^{3+}$ substitutional doping should be p-type while sulfur vacancies are n-type. Therefore, sulfur vacancies have a greater impact on the electronic structures of $MoS_2$ than $Nd^{3+}$ ions. Moreover, full width at half maximum (FWHM) of $A_{1g}$ peak increases from 2.4 for pure $MoS_2$ crystal to 3.0-3.3 for Nd-doped $MoS_2$, suggesting decreasing crystallinity caused by surface defects.

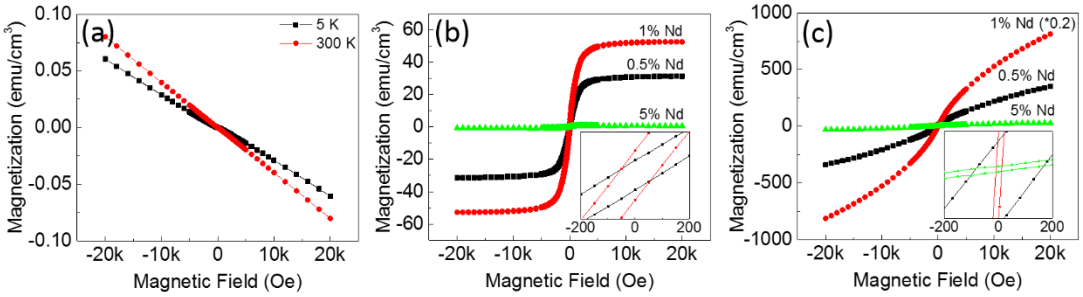


**Figure 6.11 (a) M-H loops of pure $MoS_2$ measured at 5 K and 300 K. Hysteresis loops of Nd-doped $MoS_2$ after deducting the diamagnetic signals, measured at (b) 300K and (c) 5 K. The inset is the loop in a small field range.**

To investigate the magnetic properties of the Nd-doped $MoS_2$ crystals, SQUID measurements were performed at various temperatures. Figure 6.11 shows the magnetization versus magnetic field (*M–H*) curves of Nd-doped $MoS_2$ crystals at 300 and 5 K. Pure $MoS_2$ crystal exhibits sole diamagnetic feature at both temperatures. For the Nd

doped $MoS_2$, the magnetization should only come from doping area since pure $MoS_2$ crystal does not make any contribution to the ferromagnetism. After deducting the diamagnetic signal from pure $MoS_2$, the M-H loops of Nd-doped $MoS_2$ samples are shown in figure 6.11(b). Room-temperature ferromagnetism in Nd-doped $MoS_2$ except 5 at% is confirmed by evident coercivities shown in the inset. The Ms of 0.5 and 1 at% Nd-doped $MoS_2$ at room temperature are ~33.6 and 28.3 $\mu_B$/Nd, given that all the magnetic moments are contributed from Nd dopants. At 5 K, both 0.5 and 1 at% Nd-doped $MoS_2$ show strong ferromagnetic plus paramagnetic signals, supported by the non-saturated M-H loop at relatively high magnetic field in figure 6.11(c). For 5 at% Nd-doped $MoS_2$, a small hysteresis loop can be observed at 5 K, suggesting that a tiny amount of ferromagnetic ordering remains.

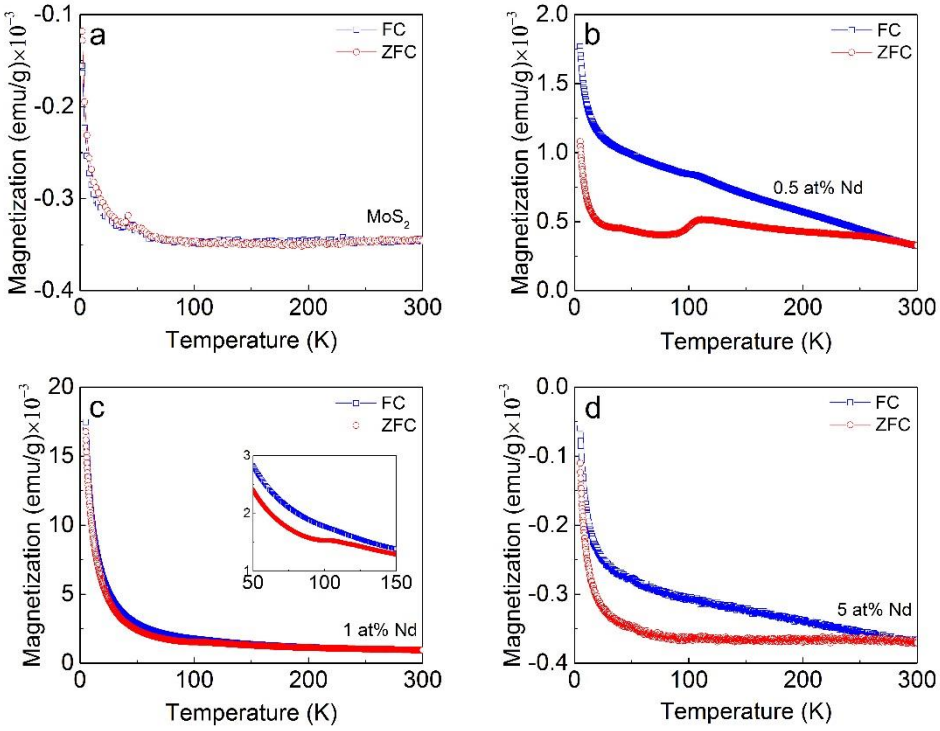


**Figure 6.12 ZFC and FC curves of $MoS_2$ with different dopant concentrations. (a) pure; (b) 0.5 at%; (c) 1 at%; and (d) 5 at% Nd-doped $MoS_2$. The inset in (c) presents the same curves in (c) in the range of 50 K to 150 K. The applied field for ZFC and FC measurement is 500 Oe.**

Although neither theoretical nor experimental studies about Nd-doped TMDs systems

have been reported so far, several works on Nd-doped transition metal oxides has been published [218, 220, 244]. Strong ferromagnetic ordering is reported in the above literatures, ascribed to the strong spin-orbit coupling of rare earth elements. Figure 6.12 illustrates the zero field cooling (ZFC) and field cooling (FC) curves of all samples, which further confirms pure $MoS_2$ crystals do not make any contribution to the ferromagnetism. As shown in figure 6.12(a), there is no divergence between ZFC and FC curves from 5 to 300 K. It is to note the magnetization of the ZFC and FC curves is negative, due to the diamagnetic nature of the sample. In addition, the hump at around 50 K is associated with the signal from oxygen. For 0.5 at% Nd-doped $MoS_2$, there is an obvious separation between ZFC and FC curves (figure 6.12(b)) and the divergence reaches temperature close to 300 K, suggesting that weak ferromagnetic ordering with relatively high Curie temperature exists in the sample, which is consistent with M-H loop measurement. A transition temperature at around 110 K can be clearly seen in both ZFC and FC curves, which is associated with defective $MoS_2$ having a phase transformation at this temperature, as previously reported [207]. For 1 at% Nd-doped $MoS_2$, ZFC and FC appears to overlap due to the high magnetization at low temperature caused by paramagnetism. However, the enlarged part shown in the inset clearly shows similar feature to 0.5 at% Nd doped sample. For 5 at% Nd-doped $MoS_2$, only weak ferromagnetism is observed and the strong diamagnetic signal from undoped $MoS_2$ part dominates.

The observed ferromagnetic behaviour of Nd-doped $MoS_2$ crystals may be originated from the exchange coupling of sulfur vacancies with $Nd^{3+}$ ions, which is often explained by the bound magnetic polarons (BMP) [80]. It is suggested the sulfur vacancies in Nd-doped $MoS_2$ can create localized electrons because of the redistribution of the localized charges. The localized electrons can polarize surrounding magnetic $Nd^{3+}$ ions, leading to

the formation of magnetic polarons [244]. When the density of magnetic polarons increases, the areas of magnetic polarons eventually overlap and induce the spin-spin interaction between $Nd^{3+}$ magnetic ions, giving rise to the long-range ferromagnetism in Nd-doped $MoS_2$ crystals, as illustrated in figure 6.13. Moreover, $Nd^{3+}$ ions may not be the only contributor to the colossal magnetic moment of ~30 $\mu_B$/Nd. Sulfur vacancies and other defects within the magnetic polarons may also contribute to the high magnetic moment. In this case, 5% Nd doping should exhibit the highest saturation magnetization since it possesses the highest concentration of defects due to ion implantation. On the contrary, it shows the weakest ferromagnetism among the three samples. Hence, the high magnetic moment is not originated from sulfur or Mo vacancies but from more complex $Nd^{3+}$ related defects. $Nd^{3+}$ should play the dominant roles for the giant magnetic moment. The maxima of ZFC/FC curves around ~110 K is probably also caused by the magnetic polarons since the phase transformation may affect the distribution of dopants inside $MoS_2$. Some isolated magnetic polarons in particular regions may only be able to remain ferromagnetic ordering at the temperature below 110 K. A similar curve feature can be observed in graphene, explained by the coexistence of ferromagnetic and antiferromagnetic states [245].

When the concentration of Nd dopants exceeds certain threshold, antiferromagnetic ordering replaces ferromagnetic ordering as neighbour magnetic $Nd^{3+}$ ions are close enough to create antiferromagnetic pairs for reducing system energy. In the samples of 0.5 and 1 at% Nd-doped $MoS_2$, ferromagnetic ordering dominates. However, when the doping concentration reaches 5 at%, Nd dopants segregate and form $NdS_2$ secondary phase due to the non-uniform distribution. The BMP model is no longer valid at this situation. Hence, diamagnetic signals dominate. However, unlike the overlapped ZFC/FC curves in pure $MoS_2$, the divergence in 5 at% Nd-doped $MoS_2$ indicates weak

ferromagnetism remains in the sample. The source of the weak ferromagnetism may be from the region with relatively lower doping concentration.

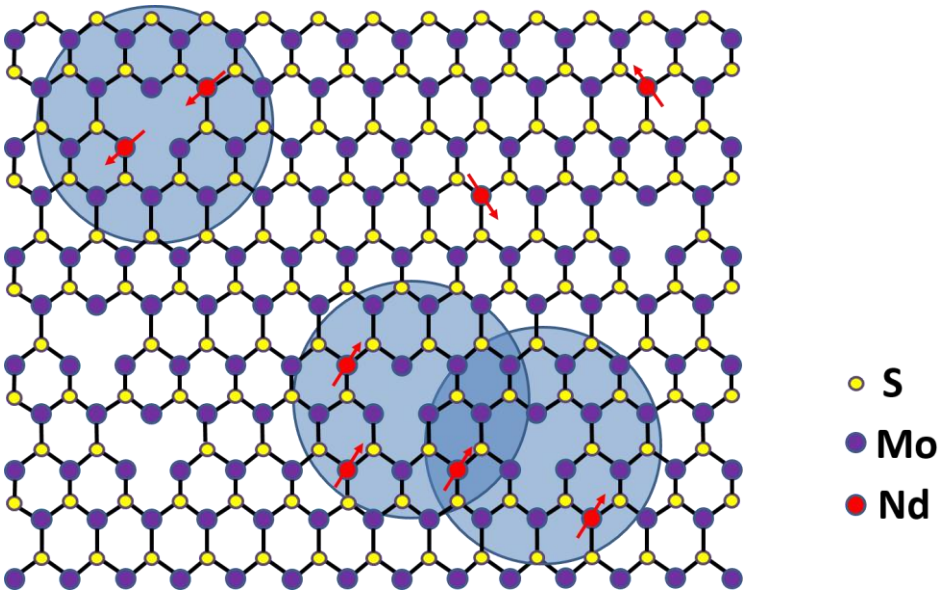


**Figure 6.13 A schematic diagram of bound magnetic polarons model for Nd-doped $MoS_2$ system. The radius represents a hydrogenic orbital confined by an electron associated with sulfur vacancies.**

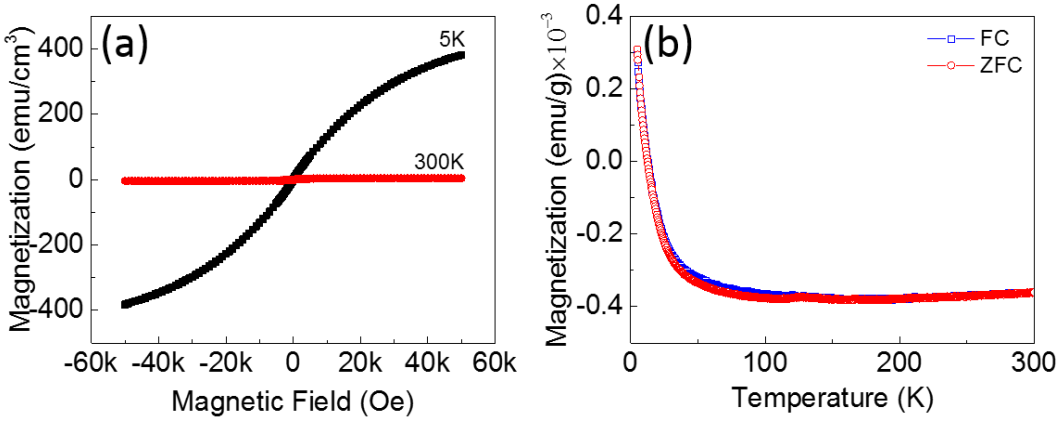


**Figure 6.14 (a) M-H loops (after deducting the diamagnetic signals) and (b) ZFC and FC curves of post annealed 0.5 at% Nd-doped $MoS_2$. The magnetic field applied is 500 Oe.**

A post annealing procedure frequently, if not always, follows ion implantation which aims to remove lattice stress and repair defects such as interstitials. To see whether it has any effect on the magnetic properties of Nd-doped $MoS_2$, we performed a quick annealing (10 min) for 0.5 at% Nd-doped $MoS_2$ at 400 $^oC$ under forming gas (95%Ar,5% $H_2$). The M-H and ZFC/FC curves of post-annealed sample are presented in figure 6.14, indicating

that the room-temperature ferromagnetism disappears after annealing. Due to the high energy of ion implantation, vacancy generation is thought to be non-equilibrium, random and isolated. However, thermal treatments like annealing can prompt the formation of vacancy clusters with different configurations, such as vacancy lines, according to both theoretical and experimental studies [246, 247]. The diffusion of Nd dopants and sulfur vacancies destroys the formation of magnetic polarons, leading to the vanishing of ferromagnetism.

## 6.4 Conclusions

In summary, annealing of $WS_2$ powders was performed to explore how defects affect the magnetic properties. It is found that annealing can effectively change the density of sulfur vacancies, which increases with increased annealing temperature but diminishes at 1000 $^oC$. The annealed powders show ferromagnetic ordering with Tc above room temperature, in addition to the existence of paramagnetic phases at low temperature. The highest saturation magnetization of ~0.002 emu/g is achieved by the $WS_2$ powder annealed at 700 $^oC$ with the highest volume of vacancies, suggesting vacancies play a significant role in enhanced magnetization. The magnetism of 2D TMDs can be modulated via defects engineering, which offers valuable guides for the magnetic performance in potential spintronic devices.

Doping of Nd into $MoS_2$ crystals was successfully carried out by ion implantation. The microstructure and magnetic properties of Nd doped $MoS_2$ crystals were studied systematically. Results reveal that Nd dopants are at a trivalent chemical state as $Nd^{3+}$ ions without the formation of secondary phase at low doping concentrations. Meanwhile, sulfur vacancies are also introduced into the samples by Nd doping. Giant magnetic moment has been observed in the samples with 0.5 at% and 1 at% Nd. The

ferromagnetism in Nd doped $MoS_2$ crystals can be explained by the BMP model, in which magnetic polarons are created by the exchange coupling of sulfur vacancies and magnetic $Nd^{3+}$ ions.

# Chapter 7 Conclusions and Future Work

In this dissertation, the magnetic properties of a variety of diluted magnetic semiconductors, including $TiO_2$ based, $MoS_2$ based and $WS_2$ based materials, were studied. Firstly, we prepared 5 at% Co doped $TiO_2$ thin film on $LaAlO_3$ (001) substrate by pulsed laser deposition. XRD pattern shows a pure anatase phase with (001) plane parallel to the substrate surface. SAED analysis confirms the orientation relationships between the anatase thin film and LAO substrate is $(001)_{anatase}||(001)_{LAO}$ in out-of-plane direction and further indicates in-plane orientation relationships are $[100]_{anatase}||[100]_{LAO}$ and $[010]_{anatase}||[010]_{LAO}$. Co nanoclusters with different sizes are observed near the interface from high-resolution TEM image. Larger clusters with diameters around 5 nm are located close the interface, while 1-2 nm small nanoclusters are embedded inside the film. Except a small amount of oxidized Co in the surface layer, most Co dopants exist as metallic $Co^0$.

An ultra-high magnetic moment of 3.5 $\mu_B$/Co at room temperature was obtained from Co doped anatase $TiO_2$ thin film through XMCD measurements, given that all the magnetization come only from Co. In addition, XMCD measurement suggests the contribution from oxygen cannot be ignored. PNR measurement further indicates that the nanoreigns near the interface with higher Co concentration generate higher magnetization and the highest saturation magnetization at the peak area is around 106 emu/$cm^3$. To clarify the mechanism of observed magnetic moment, first-principles calculations were performed considering spin-orbit coupling. Results show that that the easy spin axis for Co nanoclusters lays along [001] direction. A Co cluster containing 15 atoms can obtain a high magnetic moment of 2.9 $\mu_B$ per Co atom, demonstrating that magnetic Co nanoclusters embedded in $TiO_2$ matrix are able to show high magnetic moment above room temperature.

To further investigate the relationship between microstructure and magnetic properties of Co doped $TiO_2$ system, a series of thin films were prepared on $SrTiO_3$ (001) substrate under different temperatures and growth rates. It was found deposition parameters have great impact on both size and distribution of Co nanoclusters, as well as the crystallinity of the anatase thin film. Only polycrystalline film can be obtained at 500 $^oC$ with high deposition rate, in which Co segregates into small clusters at the interface. Higher temperatures and slow growth rate lead to fully relaxed epitaxial thin films. In the meantime, Co clusters become larger in size and move to the surface. SQUID measurements show a highest magnetic moment of 2.5 $\mu_B$/Co at room temperature. Moreover, large magnetization exceeding 2 $\mu_B$/Co can be achieved by Co nanoclusters with size bigger than 20 nm.

The second half of this dissertation was to study the magnetic properties of two transition metal dichalcogenides, $WS_2$ and $MoS_2$. Firstly, $WS_2$ powders were annealed to increase the concentration of defects. XPS and ESR results indicate that density of sulfur vacancies significantly increases with increased annealing temperature below 1000 $^oC$. All annealed powders show room-temperature ferromagnetism. The highest saturation magnetization of ~0.002 emu/g is achieved by the $WS_2$ powder annealed at 700 $^oC$ with the highest volume of vacancies, suggesting vacancies play a significant role in enhanced magnetization. In the following work, Nd was doped into $MoS_2$ crystals by ion implantation. Results reveal that Nd dopants are existed as $Nd^{3+}$ ions without the formation of secondary phase at low doping concentrations. Meanwhile, Nd doping can introduce sulfur vacancies or even Mo vacancies at the surface. Giant magnetic moment around 30 $\mu_B$/Nd has been observed in the samples with 0.5 at% and 1 at% Nd doped samples. The ferromagnetism in Nd doped $MoS_2$ crystals can be explained by the BMP model, in which magnetic polarons are created by the exchange coupling of sulphur

vacancies and magnetic $Nd^{3+}$ ions.

This dissertation has demonstrated the great potential of TMDs in advanced magnetic semiconductors with the accomplishment of simultaneous high Curie temperature and high magnetic moment. Moreover, the dopants in $TiO_2$ and $MoS_2$ are structurally, chemically and magnetically protected by the matrix, and hence offer more stable magnetic properties. However, within the framework of this thesis, it is impossible to cover all the magnetic properties of $TiO_2$-based and TMDCs based DMSs. In order to fully clarify the exact mechanism of ferromagnetism in the DMSs, further research work needs to be done in the future. In Co-$TiO_2$ grown on LAO, a large XMCD response has been obtained from O K edge in addition to Co L edge, suggesting O element is another source for the high magnetization. However, how O contributes to the magnetic moment remains unclear in this work. A number of previous reports suggest O vacancy, one of the most crucial and supposed to be the prevalent defect in many metal oxides, is able to induce ferromagnetism in $TiO_2$ even without extra magnetic dopants. The existence of O vacancy in the Co-doped $TiO_2$ thin film and the relation of concentration with magnetic properties need to be further investigated. Since O vacancy alters the electronic structure of $TiO_2$, it can be detected by methods like electron spin resonance and UV/visible light absorption. In addition to high magnetization, magnetic properties that can be tuned through extra fields are of great interest. Based on our previous study, relatively high deposition rate and low partial oxygen pressure lead to a more spatially uniform distribution of Co dopant. This work has identified that temperature is also a critical factor for the distribution of magnetic dopants. A magnetic phase diagram for Co-doped $TiO_2$ or other oxide based diluted magnetic semiconductors as functions of partial oxygen pressure and temperature can be drawn in the future by the variation of experiment parameters. Additionally, the choice of matrix material to embed Co should not be limited

to only $TiO_2$. Whether Co can maintain the high magnetization when switching $TiO_2$ to other semiconducting oxides is worth studying. Furthermore, dopants are not limited to Co either. Fe, Ni and other transition metals may be employed as the dopants. For Co-$TiO_2$ grown on STO, further complementary techniques in addition to STEM needs to be carried out to evaluate the exact size of Co nanoclusters. The impact of growth parameters on the concentration and magnetization of defects like O vacancies may also be an interesting topic. It is shown that higher temperature and slower growth rate lead to larger cluster size. The establishment of an exact mathematical relation between cluster size or saturation magnetization and growth parameters can be further investigated. The $TiO_2$ epitaxial thin film obtained on STO in this work is fully relaxed with no strain. As magnetic properties have been manipulated through strain engineering in numerous reports, preparation of fully or partially strained $TiO_2$ thin films and the variation of the magnetic properties can be the next step of the research. For $WS_2$ powders, annealing is not the only method to induce vacancies. The magnetic properties can be discussed with the samples treated by other approaches, such as plasma treatment. In addition, more magnetic properties like the Curie temperature need to be further investigated. Heat treatment can also be applied to other TMD materials such as $MoSe_2$ to study the impact of anion on magnetic properties. For Nd-doped $MoS_2$, the exact mechanism behind the astonishingly huge magnetic moment of Nd needs further investigation. First-principles spin-polarised calculations under density functional theory with different schemes for the electron exchange and correlation functional can be employed for the discussion. For the minimization of semiconductor devices, few-layer or monolayer $MoS_2$ will serve as matrix material in the future work. Chemical vapor deposition is currently one of the most promising methods to realize the growth of 2D TMDCs with large-scale, uniform thickness and usually regular shapes. 2D $MoS_2$ can be synthesized using Mo and sulfur

powders as precursors and then doped with a variety of transition and rare earth metals. The fabrication of electronic devices should then be followed through photolithography or e-beam lithography and several semiconducting properties such as the carrier type and density need further examination. Moreover, the possible magnetic modulation of the device through external fields needs to be tested, as well as a number of fundamental magnetic properties like the Curie temperature. The materials can also seek applications in certain fields such as nanomotor and sensors.

# References


1. Wolf, S., D. Awschalom, R. Buhrman, J. Daughton, S. Von Molnar, M. Roukes, A.Y. Chtchelkanova, and D. Treger, *Spintronics: a spin-based electronics vision for the future.* science, 2001. **294**(5546): p. 1488-1495.
2. Baibich, M.N., J.M. Broto, A. Fert, F.N. Vandau, F. Petroff, P. Eitenne, G. Creuzet, A. Friederich, and J. Chazelas, *Giant magnetoresistance of (001) Fe/(001) Cr magnetic superlattices.* Physical Review Letters, 1988. **61**(21): p. 2472-2475.
3. Dieny, B., V.S. Speriosu, S.S.P. Parkin, B.A. Gurney, D.R. Wilhoit, and D. Mauri, *Giant magnetoresistance in soft ferromagnetic multilayers.* Physical Review B, 1991. **43**(1): p. 1297-1300.
4. Reiss, G., H. Brueckl, A. Huetten, J. Schotter, M. Brzeska, M. Panhorst, D. Sudfeld, A. Becker, P.B. Kamp, and A. Puehler, *Magnetoresistive sensors and magnetic nanoparticles for biotechnology.* Journal of Materials Research, 2005. **20**(12): p. 3294-3302.
5. Granig, W., M. Weinberger, C. Reidl, M. Bresch, M. Strasser, and G. Pircher, *Integrated GMR angle sensor for electrical commutated motors including features for safety critical applications.* Procedia Engineering, 2010. **5**: p. 1384-1387.
6. Freitas, P.P., S. Cardoso, R. Ferreira, V.C. Martins, A. Guedes, F.A. Cardoso, J. Loureiro, R. Macedo, R.C. Chaves, and J. Amaral. *Optimization and integration of magnetoresistive sensors*. in *Spin*. 2011. World Scientific.
7. Rifai, D., A. Abdalla, K. Ali, and R. Razali, *Giant magnetoresistance sensors: A review on structures and non-destructive eddy current testing applications.* Sensors, 2016. **16**(3): p. 298.
8. Ennen, I., D. Kappe, T. Rempel, C. Glenske, and A. Hütten, *Giant magnetoresistance: Basic concepts, microstructure, magnetic interactions and applications.* Sensors, 2016. **16**(6): p. 904.
9. Apalkov, D., B. Dieny, and J. Slaughter, *Magnetoresistive random access memory.* Proceedings of the IEEE, 2016. **104**(10): p. 1796-1830.
10. Bhatti, S., R. Sbiaa, A. Hirohata, H. Ohno, S. Fukami, and S. Piramanayagam, *Spintronics based random access memory: a review.* Materials Today, 2017. **20**(9): p. 530-548.

11. Schliemann, J., J.C. Egues, and D. Loss, *Nonballistic spin-field-effect transistor.* Physical review letters, 2003. **90**(14): p. 146801.
12. Wang, B., J. Wang, and H. Guo, *Quantum spin field effect transistor.* Physical Review B, 2003. **67**(9): p. 092408.
13. Holub, M. and P. Bhattacharya, *Spin-polarized light-emitting diodes and lasers.* Journal of Physics D: Applied Physics, 2007. **40**(11): p. R179.
14. Farshchi, R., M. Ramsteiner, J. Herfort, A. Tahraoui, and H. Grahn, *Optical communication of spin information between light emitting diodes.* Applied Physics Letters, 2011. **98**(16): p. 162508.
15. Ho, S.-C., *Introduction of All-electric Spin Field-Effect Transistor*, in *Contemporary Topics in Semiconductor Spintronics*. 2017, World Scientific. p. 159-185.
16. Wunderlich, J., B.-G. Park, A.C. Irvine, L.P. Zârbo, E. Rozkotová, P. Nemec, V. Novák, J. Sinova, and T. Jungwirth, *Spin Hall effect transistor.* Science, 2010. **330**(6012): p. 1801-1804.
17. Dietl, T., *A ten-year perspective on dilute magnetic semiconductors and oxides.* Nature materials, 2010. **9**(12): p. 965.
18. Sadowski, J., P. Dluzewski, S. Kret, E. Janik, E. Lusakowska, J. Kanski, A. Presz, F. Terki, S. Charar, and D. Tang, *GaAs : Mn nanowires grown by molecular beam epitaxy of (Ga,Mn)As at MnAs segregation conditions.* Nano Letters, 2007. **7**(9): p. 2724-2728.
19. Ohno, H., *Making nonmagnetic semiconductors ferromagnetic.* Science, 1998. **281**(5379): p. 951-956.
20. Nazmul, A.M., S. Sugahara, and M. Tanaka, *MBE growth, structural, and transport properties of Mn δ-doped GaAs layers.* Journal of crystal growth, 2003. **251**(1-4): p. 303-310.
21. van Schilfgaarde, M. and O.N. Mryasov, *Anomalous exchange interactions in III-V dilute magnetic semiconductors.* Physical Review B, 2001. **63**(23): p. 233205.
22. Sato, K., H. Katayama-Yoshida, and P.H. Dederichs, *High Curie temperature and nano-scale spinodal decomposition phase in dilute magnetic semiconductors.* Japanese Journal of Applied Physics Part 2-Letters & Express Letters, 2005. **44**(28-32): p. L948.

23. Kodzuka, M., T. Ohkubo, K. Hono, F. Matsukura, and H. Ohno, *3DAP analysis of (Ga,Mn)As diluted magnetic semiconductor thin film.* Ultramicroscopy, 2009. **109**(5): p. 644-648.
24. Richardella, A., P. Roushan, S. Mack, B. Zhou, D.A. Huse, D.D. Awschalom, and A. Yazdani, *Visualizing Critical Correlations Near the Metal-Insulator Transition in $Ga_{1-x}Mn_xAs$.* Science, 2010. **327**(5966): p. 665-669.
25. Okabayashi, J., A. Kimura, O. Rader, T. Mizokawa, A. Fujimori, T. Hayashi, and M. Tanaka, *Core-level photoemission study of $Ga_{1-x}Mn_xAs$.* Physical Review B, 1998. **58**(8): p. R4211.
26. Okabayashi, J., A. Kimura, T. Mizokawa, A. Fujimori, T. Hayashi, and M. Tanaka, *Mn 3d partial density of states in $Ga_{1-x}Mn_xAs$ studied by resonant photoemission spectroscopy.* Physical Review B, 1999. **59**(4): p. R2486.
27. Zener, C., *Interaction between the d shells in the transition metals.* Physical Review, 1951. **81**(3): p. 440.
28. Dietl, T., A. Haury, and Y.M. d'Aubigné, *Free carrier-induced ferromagnetism in structures of diluted magnetic semiconductors.* Physical Review B, 1997. **55**(6): p. R3347.
29. Dietl, T., J. Cibert, D. Ferrand, and Y.M. d'Aubigné, *Carrier-mediated ferromagnetic interactions in structures of magnetic semiconductors.* Materials Science and Engineering: B, 1999. **63**(1-2): p. 103-110.
30. Dietl, T., H. Ohno, F. Matsukura, J. Cibert, and D. Ferrand, *Zener model description of ferromagnetism in zinc-blende magnetic semiconductors.* Science, 2000. **287**(5455): p. 1019-1022.
31. Popescu, F., Y. Yildirim, G. Alvarez, A. Moreo, and E. Dagotto, *Critical temperatures of the two-band model for diluted magnetic semiconductors.* Physical Review B, 2006. **73**(7): p. 075206.
32. Timm, C. and A. MacDonald, *Anisotropic exchange interactions in III-V diluted magnetic semiconductors.* Physical Review B, 2005. **71**(15): p. 155206.
33. Sawicki, M., D. Chiba, A. Korbecka, Y. Nishitani, J.A. Majewski, F. Matsukura, T. Dietl, and H. Ohno, *Experimental probing of the interplay between ferromagnetism and localization in (Ga, Mn)As.* Nature Physics, 2010. **6**(1): p. 22.
34. Jungwirth, T., K. Wang, J. Mašek, K. Edmonds, J. König, J. Sinova, M. Polini, N. Goncharuk, A. MacDonald, and M. Sawicki, *Prospects for high temperature*

*ferromagnetism in (Ga, Mn)As semiconductors.* Physical Review B, 2005. **72**(16): p. 165204.

35. Olejník, K., M. Owen, V. Novák, J. Mašek, A. Irvine, J. Wunderlich, and T. Jungwirth, *Enhanced annealing, high Curie temperature, and low-voltage gating in (Ga, Mn)As: A surface oxide control study.* Physical Review B, 2008. **78**(5): p. 054403.
36. Wang, M., R. Campion, A. Rushforth, K. Edmonds, C. Foxon, and B. Gallagher, *Achieving high curie temperature in (Ga, Mn)As.* Applied Physics Letters, 2008. **93**(13): p. 132103.
37. Chen, L., S. Yan, P. Xu, J. Lu, W. Wang, J. Deng, X. Qian, Y. Ji, and J. Zhao, *Low-temperature magnetotransport behaviors of heavily Mn-doped (Ga, Mn)As films with high ferromagnetic transition temperature.* Applied Physics Letters, 2009. **95**(18): p. 182505.
38. Chen, L., X. Yang, F. Yang, J. Zhao, J. Misuraca, P. Xiong, and S. von Molnár, *Enhancing the Curie temperature of ferromagnetic semiconductor (Ga, Mn) As to 200 K via nanostructure engineering.* Nano letters, 2011. **11**(7): p. 2584-2589.
39. Nazmul, A.M., S. Kobayashi, S. Sugahara, and M. Tanaka, *Electrical and optical control of ferromagnetism in III-V semiconductor heterostructures at high temperature (∼ 100 K).* Japanese journal of applied physics, 2004. **43**(2A): p. L233.
40. Chiba, D., F. Matsukura, and H. Ohno, *Electric-field control of ferromagnetism in (Ga, Mn)As.* Applied Physics Letters, 2006. **89**(16): p. 162505.
41. Chiba, D., A. Werpachowska, M. Endo, Y. Nishitani, F. Matsukura, T. Dietl, and H. Ohno, *Anomalous Hall effect in field-effect structures of (Ga, Mn)As.* Physical review letters, 2010. **104**(10): p. 106601.
42. Nishitani, Y., D. Chiba, M. Endo, M. Sawicki, F. Matsukura, T. Dietl, and H. Ohno, *Curie temperature versus hole concentration in field-effect structures of Ga1−xMnxAs.* Physical Review B, 2010. **81**(4): p. 045208.
43. Oiwa, A., Y. Mitsumori, R. Moriya, T. Słupinski, and H. Munekata, *Effect of Optical Spin Injection on Ferromagnetically Coupled Mn Spins in the III-V Magnetic Alloy Semiconductor (Ga, Mn)As.* Physical review letters, 2002. **88**(13): p. 137202.

44. Aoyama, J., S. Kobayashi, and H. Munekata, *All-optical 90-degree switching of magnetization in a ferromagnetic $Ga_{0.98}Mn_{0.02}As$ microbar.* Journal of Applied Physics, 2010. **107**(9): p. 09C301.

45. Rudolph, A., M. Soda, M. Kiessling, T. Wojtowicz, D. Schuh, W. Wegscheider, J. Zweck, C. Back, and E. Reiger, *Ferromagnetic GaAs/GaMnAs Core−Shell Nanowires Grown by Molecular Beam Epitaxy.* Nano letters, 2009. **9**(11): p. 3860-3866.

46. King, C., J. Zemen, K. Olejník, L. Horák, J. Haigh, V. Novák, A. Irvine, J. Kučera, V. Holý, and R. Campion, *Strain control of magnetic anisotropy in (Ga, Mn)As microbars.* Physical Review B, 2011. **83**(11): p. 115312.

47. Hümpfner, S., K. Pappert, J. Wenisch, K. Brunner, C. Gould, G. Schmidt, L. Molenkamp, M. Sawicki, and T. Dietl, *Lithographic engineering of anisotropies in (Ga, Mn)As.* Applied Physics Letters, 2007. **90**(10): p. 102102.

48. Young, D.K., E. Johnston-Halperin, D. Awschalom, Y. Ohno, and H. Ohno, *Anisotropic electrical spin injection in ferromagnetic semiconductor heterostructures.* Applied physics letters, 2002. **80**(9): p. 1598-1600.

49. Van Dorpe, P., Z. Liu, W. Van Roy, V. Motsnyi, M. Sawicki, G. Borghs, and J. De Boeck, *Very high spin polarization in GaAs by injection from a (Ga, Mn)As Zener diode.* Applied physics letters, 2004. **84**(18): p. 3495-3497.

50. Van Dorpe, P., W. Van Roy, J. De Boeck, G. Borghs, P. Sankowski, P. Kacman, J. Majewski, and T. Dietl, *Voltage-controlled spin injection in a (Ga, Mn)As/(Al, Ga)As Zener diode.* Physical Review B, 2005. **72**(20): p. 205322.

51. Kohda, M., T. Kita, Y. Ohno, F. Matsukura, and H. Ohno, *Bias voltage dependence of the electron spin injection studied in a three-terminal device based on a (Ga, Mn)As/n+-GaAs Esaki diode.* Applied physics letters, 2006. **89**(1): p. 012103.

52. Ciorga, M., A. Einwanger, U. Wurstbauer, D. Schuh, W. Wegscheider, and D. Weiss, *Electrical spin injection and detection in lateral all-semiconductor devices.* Physical Review B, 2009. **79**(16): p. 165321.

53. Pappert, K., S. Hümpfner, C. Gould, J. Wenisch, K. Brunner, G. Schmidt, and L.W. Molenkamp, *A non-volatile-memory device on the basis of engineered anisotropies in (Ga, Mn)As.* Nature Physics, 2007. **3**(8): p. 573.

54. Mark, S., P. Dürrenfeld, K. Pappert, L. Ebel, K. Brunner, C. Gould, and L. Molenkamp, *Fully electrical read-write device out of a ferromagnetic semiconductor.* Physical review letters, 2011. **106**(5): p. 057204.

55. Ogale, S.B., *Dilute doping, defects, and ferromagnetism in metal oxide systems.* Advanced materials, 2010. **22**(29): p. 3125-3155.

56. Matsumoto, Y., M. Murakami, T. Shono, T. Hasegawa, T. Fukumura, M. Kawasaki, P. Ahmet, T. Chikyow, S.-y. Koshihara, and H. Koinuma, *Room-temperature ferromagnetism in transparent transition metal-doped titanium dioxide.* Science, 2001. **291**(5505): p. 854-856.

57. Toyosaki, H., T. Fukumura, Y. Yamada, K. Nakajima, T. Chikyow, T. Hasegawa, H. Koinuma, and M. Kawasaki, *Anomalous Hall effect governed by electron doping in a room-temperature transparent ferromagnetic semiconductor.* Nature materials, 2004. **3**(4): p. 221.

58. Chambers, S.A., C.M. Wang, S. Thevuthasan, T. Droubay, D.E. McCready, A.S. Lea, V. Shutthanandan, and C. Windisch Jr, *Epitaxial growth and properties of MBE-grown ferromagnetic Co-doped $TiO_2$ anatase films on $SrTiO_3$ (001) and $LaAlO_3$ (001).* Thin Solid Films, 2002. **418**(2): p. 197-210.

59. Chambers, S.A., T. Droubay, C.M. Wang, A.S. Lea, R. Farrow, L. Folks, V. Deline, and S. Anders, *Clusters and magnetism in epitaxial Co-doped $TiO_2$ anatase.* Applied physics letters, 2003. **82**(8): p. 1257-1259.

60. Park, W.K., R.J. Ortega-Hertogs, J.S. Moodera, A. Punnoose, and M. Seehra, *Semiconducting and ferromagnetic behavior of sputtered Co-doped $TiO_2$ thin films above room temperature.* Journal of applied Physics, 2002. **91**(10): p. 8093-8095.

61. Balagurov, L., S.O. Klimonsky, S. Kobeleva, A. Orlov, N.S. Perov, and D. Yarkin, *On the origin of ferromagnetism in semiconducting $TiO_{2-\delta}$: Co oxide.* Journal of Experimental and Theoretical Physics Letters, 2004. **79**(2): p. 98-99.

62. Yang, H.S. and R.K. Singh, *Growth and properties of Co-doped $TiO_2$ thin films grown on buffered Si substrate.* Journal of applied physics, 2004. **95**(11): p. 7192-7194.

63. Ueno, K., T. Fukumura, H. Toyosaki, M. Nakano, and M. Kawasaki, *Anomalous Hall effect in anatase $Ti_{1-x}Co_xO_{2-\delta}$ at low temperature regime.* Applied physics letters, 2007. **90**(7): p. 072103.

64. Higgins, J., S. Shinde, S. Ogale, T. Venkatesan, and R. Greene, *Hall effect in cobalt-doped $TiO_{2-\delta}$.* Physical Review B, 2004. **69**(7): p. 073201.

65. Ueno, K., T. Fukumura, H. Toyosaki, M. Nakano, T. Yamasaki, Y. Yamada, and M. Kawasaki, *Anomalous Hall effect in anatase $Ti_{1-x}Co_xO_{2-\delta}$ above room temperature.* Journal of Applied Physics, 2008. **103**(7): p. 07D114.

66. Yamada, Y., H. Toyosaki, A. Tsukazaki, T. Fukumura, K. Tamura, Y. Segawa, K. Nakajima, T. Aoyama, T. Chikyow, and T. Hasegawa, *Epitaxial growth and physical properties of a room temperature ferromagnetic semiconductor: Anatase phase $Ti_{1-x}Co_xO_2$.* Journal of applied physics, 2004. **96**(9): p. 5097-5102.

67. Toyosaki, H., T. Fukumura, Y. Yamada, and M. Kawasaki, *Evolution of ferromagnetic circular dichroism coincident with magnetization and anomalous Hall effect in Co-doped rutile $TiO_2$.* Applied Physics Letters, 2005. **86**(18): p. 182503.

68. Fukumura, T., H. Toyosaki, K. Ueno, M. Nakano, and M. Kawasaki, *Role of charge carriers for ferromagnetism in cobalt-doped rutile $TiO_2$.* New Journal of physics, 2008. **10**(5): p. 055018.

69. Mamiya, K., T. Koide, A. Fujimori, H. Tokano, H. Manaka, A. Tanaka, H. Toyosaki, T. Fukumura, and M. Kawasaki, *Indication of intrinsic room-temperature ferromagnetism in $Ti_{1-x}Co_xO_{2-\delta}$ thin film: An x-ray magnetic circular dichroism study.* Applied physics letters, 2006. **89**(6): p. 062506.

70. Quilty, J., A. Shibata, J.-Y. Son, K. Takubo, T. Mizokawa, H. Toyosaki, T. Fukumura, and M. Kawasaki, *Signature of Carrier-Induced Ferromagnetism in $Ti_{1-x}Co_xO_{2-\delta}$: Exchange Interaction between High-Spin $Co^{2+}$ and the Ti 3d Conduction Band.* Physical review letters, 2006. **96**(2): p. 027202.

71. Matsumura, T., D. Okuyama, S. Niioka, H. Ishida, T. Satoh, Y. Murakami, H. Toyosaki, Y. Yamada, T. Fukumura, and M. Kawasaki, *X-ray anomalous scattering of diluted magnetic oxide semiconductors: Possible evidence of lattice deformation for high temperature ferromagnetism.* Physical Review B, 2007. **76**(11): p. 115320.

72. Kim, J., J. Park, B. Park, H. Noh, S. Oh, J. Yang, D. Kim, S. Bu, T. Noh, and H. Lin, *Ferromagnetism Induced by Clustered Co in Co-Doped Anatase $TiO_2$ Thin Films.* Physical review letters, 2003. **90**(1): p. 017401.

73. Ogale, S., D. Kundaliya, S. Mehraeen, L.-f. Fu, S. Zhang, A. Lussier, J. Dvorak, N. Browning, Y. Idzerda, and T. Venkatesan, *Chemical inhomogeneity and*

*mixed-state ferromagnetism in diluted magnetic semiconductor Co:$TiO_2$.* Chemistry of Materials, 2008. **20**(4): p. 1344-1352.

74. Shinde, S., S. Ogale, S.D. Sarma, J. Simpson, H. Drew, S. Lofland, C. Lanci, J. Buban, N. Browning, and V. Kulkarni, *Ferromagnetism in laser deposited anatase $Ti_{1-x}Co_xO_{2-\delta}$ films.* Physical Review B, 2003. **67**(11): p. 115211.
75. Yao, X., T. Zhou, Y. Gai, T. Chong, and J. Wang, *Binding state and microstructure analyses of Co-doped $TiO_2$ thin film.* Journal of applied physics, 2004. **95**(11): p. 7375-7377.
76. Kim, D., J. Yang, Y. Kim, T. Noh, S. Bu, S. Baik, Y. Kim, Y. Park, S. Pearton, and J. Kim, *Effects of high-temperature postannealing on magnetic properties of Co-doped anatase $TiO_2$ thin films.* Physical Review B, 2005. **71**(1): p. 014440.
77. Griffin, K.A., A. Pakhomov, C.M. Wang, S.M. Heald, and K.M. Krishnan, *Cobalt-doped anatase $TiO_2$: A room temperature dilute magnetic dielectric material.* Journal of applied physics, 2005. **97**(10): p. 10D320.
78. Pereira, L., *Experimentally evaluating the origin of dilute magnetism in nanomaterials.* Journal of Physics D: Applied Physics, 2017. **50**(39): p. 393002.
79. Shinde, S., S. Ogale, J. Higgins, H. Zheng, A. Millis, V. Kulkarni, R. Ramesh, R. Greene, and T. Venkatesan, *Co-occurrence of superparamagnetism and anomalous Hall effect in highly reduced cobalt-doped rutile $TiO_{2-\delta}$ films.* Physical Review Letters, 2004. **92**(16): p. 166601.
80. Coey, J., M. Venkatesan, and C. Fitzgerald, *Donor impurity band exchange in dilute ferromagnetic oxides.* Nature materials, 2005. **4**(2): p. 173.
81. Torrance, J., M. Shafer, and T. McGuire, *Bound magnetic polarons and the insulator-metal transition in EuO.* Physical Review Letters, 1972. **29**(17): p. 1168.
82. Angelescu, D. and R. Bhatt, *Effective interaction Hamiltonian of polaron pairs in diluted magnetic semiconductors.* Physical Review B, 2002. **65**(7): p. 075211.
83. Durst, A.C., R. Bhatt, and P. Wolff, *Bound magnetic polaron interactions in insulating doped diluted magnetic semiconductors.* Physical Review B, 2002. **65**(23): p. 235205.
84. Zhao, T., S. Shinde, S. Ogale, H. Zheng, T. Venkatesan, R. Ramesh, and S.D. Sarma, *Electric field effect in diluted magnetic insulator anatase Co: $TiO_2$.* Physical review letters, 2005. **94**(12): p. 126601.
85. Yamada, Y., K. Ueno, T. Fukumura, H. Yuan, H. Shimotani, Y. Iwasa, L. Gu, S. Tsukimoto, Y. Ikuhara, and M. Kawasaki, *Electrically induced ferromagnetism*

*at room temperature in cobalt-doped titanium dioxide.* Science, 2011. **332**(6033): p. 1065-1067.

86. Toyosaki, H., T. Fukumura, K. Ueno, M. Nakano, and M. Kawasaki, *$Ti_{1-x}Co_xO_{2-\delta}/AlO_x/Fe_{0.1}Co_{0.9}$ magnetic tunnel junctions with varied $AlO_x$ thickness.* Journal of applied physics, 2006. **99**(8): p. 08M102.
87. Toh, R.J., Z. Sofer, J. Luxa, D. Sedmidubsky, and M. Pumera, *3R phase of $MoS_2$ and $WS_2$ outperforms the corresponding 2H phase for hydrogen evolution.* Chemical Communications, 2017. **53**(21): p. 3054-3057.
88. Splendiani, A., L. Sun, Y.B. Zhang, T.S. Li, J. Kim, C.Y. Chim, G. Galli, and F. Wang, *Emerging photoluminescence in monolayer $MoS_2$.* Nano Letters, 2010. **10**(4): p. 1271-1275.
89. Coleman, J.N., M. Lotya, A. O'Neill, S.D. Bergin, P.J. King, U. Khan, K. Young, A. Gaucher, S. De, R.J. Smith, I.V. Shvets, S.K. Arora, G. Stanton, H.-Y. Kim, K. Lee, G.T. Kim, G.S. Duesberg, T. Hallam, J.J. Boland, J.J. Wang, J.F. Donegan, J.C. Grunlan, G. Moriarty, A. Shmeliov, R.J. Nicholls, J.M. Perkins, E.M. Grieveson, K. Theuwissen, D.W. McComb, P.D. Nellist, and V. Nicolosi, *Two-dimensional nanosheets produced by liquid exfoliation of layered materials.* Science, 2011. **331**(6017): p. 568-571.
90. Zhou, K.G., N.N. Mao, H.X. Wang, Y. Peng, and H.L. Zhang, *A mixed-solvent strategy for efficient exfoliation of inorganic graphene analogues.* Angewandte Chemie-International Edition, 2011. **50**(46): p. 10839-10842.
91. Smith, R.J., P.J. King, M. Lotya, C. Wirtz, U. Khan, S. De, A. O'Neill, G.S. Duesberg, J.C. Grunlan, G. Moriarty, J. Chen, J. Wang, A.I. Minett, V. Nicolosi, and J.N. Coleman, *Large-scale exfoliation of inorganic layered compounds in aqueous surfactant solutions.* Advanced Materials, 2011. **23**(34): p. 3944-3948.
92. Xi, Y., M.I. Serna, L.X. Cheng, Y. Gao, M. Baniasadi, R. Rodriguez-Davila, J. Kim, M.A. Quevedo-Lopez, and M. Minary-Jolandan, *Fabrication of $MoS_2$ thin film transistors via selective-area solution deposition methods.* Journal of Materials Chemistry C, 2015. **3**(16): p. 3842-3847.
93. Matte, H.S.S.R., A. Gomathi, A.K. Manna, D.J. Late, R. Datta, S.K. Pati, and C.N.R. Rao, *$MoS_2$ and $WS_2$ analogues of graphene.* Angewandte Chemie-International Edition, 2010. **49**(24): p. 4059-4062.

94. Zhan, Y., Z. Liu, S. Najmaei, P.M. Ajayan, and J. Lou, *Large-area vapor-phase growth and characterization of $MoS_2$ atomic layers on a $SiO_2$ substrate.* Small, 2012. **8**(7): p. 966-971.

95. Lin, Y.C., W.J. Zhang, J.K. Huang, K.K. Liu, Y.H. Lee, C.T. Liang, C.W. Chu, and L.J. Li, *Wafer-scale $MoS_2$ thin layers prepared by $MoO_3$ sulfurization.* Nanoscale, 2012. **4**(20): p. 6637-6641.

96. Wang, X., H. Feng, Y. Wu, and L. Jiao, *Controlled synthesis of highly crystalline $MoS_2$ flakes by chemical vapor deposition.* Journal of the American Chemical Society, 2013. **135**(14): p. 5304-5307.

97. Ma, L., D.N. Nath, E.W. Lee, II, C.H. Lee, M. Yu, A. Arehart, S. Rajan, and Y. Wu, *Epitaxial growth of large area single-crystalline few-layer $MoS_2$ with high space charge mobility of 192 $cm^2V^{-1}s^{-1}$.* Applied Physics Letters, 2014. **105**(7): p. 072105.

98. Novoselov, K.S., D. Jiang, F. Schedin, T.J. Booth, V.V. Khotkevich, S.V. Morozov, and A.K. Geim, *Two-dimensional atomic crystals.* Proceedings of the National Academy of Sciences of the United States of America, 2005. **102**(30): p. 10451-10453.

99. Radisavljevic, B., A. Radenovic, J. Brivio, V. Giacometti, and A. Kis, *Single-layer $MoS_2$ transistors.* Nature Nanotechnology, 2011. **6**(3): p. 147-150.

100. Bao, W.Z., X.H. Cai, D. Kim, K. Sridhara, and M.S. Fuhrer, *High mobility ambipolar $MoS_2$ field-effect transistors: Substrate and dielectric effects.* Applied Physics Letters, 2013. **102**(4): p. 042104.

101. Lin, M.W., Kravchenko, II, J. Fowlkes, X.F. Li, A.A. Puretzky, C.M. Rouleau, D.B. Geohegan, and K. Xiao, *Thickness-dependent charge transport in few-layer $MoS_2$ field-effect transistors.* Nanotechnology, 2016. **27**(16): p. 165203.

102. Sun, X., J. Dai, Y. Guo, C. Wu, F. Hu, J. Zhao, X. Zeng, and Y. Xie, *Semimetallic molybdenum disulfide ultrathin nanosheets as an efficient electrocatalyst for hydrogen evolution.* Nanoscale, 2014. **6**(14): p. 8359-8367.

103. Feng, J., X. Sun, C. Wu, L. Peng, C. Lin, S. Hu, J. Yang, and Y. Xie, *Metallic few-layered $VS_2$ ultrathin nanosheets: High two-dimensional conductivity for in-plane supercapacitors.* Journal of the American Chemical Society, 2011. **133**(44): p. 17832-17838.

104. Zeng, Z., T. Sun, J. Zhu, X. Huang, Z. Yin, G. Lu, Z. Fan, Q. Yan, H.H. Hng, and H. Zhang, *An effective method for the fabrication of few-layer-thick inorganic*

*nanosheets.* Angewandte Chemie-International Edition, 2012. **51**(36): p. 9052-9056.

105. Eda, G., T. Fujita, H. Yamaguchi, D. Voiry, M. Chen, and M. Chhowalla, *Coherent atomic and electronic heterostructures of single-layer $MoS_2$.* Acs Nano, 2012. **6**(8): p. 7311-7317.
106. Cai, L., J. He, Q. Liu, T. Yao, L. Chen, W. Yan, F. Hu, Y. Jiang, Y. Zhao, T. Hu, Z. Sun, and S. Wei, *Vacancy-induced ferromagnetism of $MoS_2$ nanosheets.* Journal of the American Chemical Society, 2015. **137**(7): p. 2622-2627.
107. Noh, J.Y., H. Kim, and Y.S. Kim, *Stability and electronic structures of native defects in single-layer $MoS_2$.* Physical Review B, 2014. **89**(20): p. 205417.
108. Santosh, K.C., R.C. Longo, R. Addou, R.M. Wallace, and K. Cho, *Impact of intrinsic atomic defects on the electronic structure of $MoS_2$ monolayers.* Nanotechnology, 2014. **25**(37): p. 375703.
109. Addou, R., L. Colombo, and R.M. Wallace, *Surface defects on natural $MoS_2$.* Acs Applied Materials & Interfaces, 2015. **7**(22): p. 11921-11929.
110. Komsa, H.-P. and A.V. Krasheninnikov, *Native defects in bulk and monolayer $MoS_2$ from first principles.* Physical Review B, 2015. **91**(12): p. 125304.
111. Najmaei, S., J. Yuan, J. Zhang, P. Ajayan, and J. Lou, *Synthesis and defect investigation of two-dimensional molybdenum disulfide atomic layers.* Accounts of Chemical Research, 2015. **48**(1): p. 31-40.
112. Gao, D., M. Si, J. Li, J. Zhang, Z. Zhang, Z. Yang, and D. Xue, *Ferromagnetism in freestanding $MoS_2$ nanosheets.* Nanoscale Research Letters, 2013. **8**: p. 129.
113. Yang, Z., D. Gao, J. Zhang, Q. Xu, S. Shi, K. Tao, and D. Xue, *Realization of high Curie temperature ferromagnetism in atomically thin $MoS_2$ and $WS_2$ nanosheets with uniform and flower-like morphology.* Nanoscale, 2015. **7**(2): p. 650-658.
114. Sun, B., Q.L. Li, and P. Chen, *Room-temperature ferromagnetism of single-crystalline $MoS_2$ nanowires.* Micro & Nano Letters, 2014. **9**(7): p. 468-470.
115. Ataca, C. and S. Ciraci, *Functionalization of single-layer $MoS_2$ honeycomb structures.* Journal of Physical Chemistry C, 2011. **115**(27): p. 13303-13311.
116. Li, Y., Z. Zhou, S. Zhang, and Z. Chen, *$MoS_2$ nanoribbons: High stability and unusual electronic and magnetic properties.* Journal of the American Chemical Society, 2008. **130**(49): p. 16739-16744.

117. Zhang, Z., X. Zou, V.H. Crespi, and B.I. Yakobson, *Intrinsic magnetism of grain boundaries in two-dimensional metal dichalcogenides.* ACS nano, 2013. **7**(12): p. 10475-10481.

118. Gao, N., Y. Guo, S. Zhou, Y. Bai, and J. Zhao, *Structures and magnetic properties of $MoS_2$ grain boundaries with antisite defects.* The Journal of Physical Chemistry C, 2017. **121**(22): p. 12261-12269.

119. Zhou, W., X. Zou, S. Najmaei, Z. Liu, Y. Shi, J. Kong, J. Lou, P.M. Ajayan, B.I. Yakobson, and J.C. Idrobo, *Intrinsic structural defects in monolayer molybdenum disulfide.* Nano Letters, 2013. **13**(6): p. 2615-2622.

120. Fan, X.L., Y.R. An, and W.J. Guo, *Ferromagnetism in transitional metal-doped $MoS_2$ monolayer.* Nanoscale Research Letters, 2016. **11**: p. 154-163.

121. Wang, Y., S. Li, and J. Yi, *Electronic and magnetic properties of Co doped $MoS_2$ monolayer.* Scientific Reports, 2016. **6**: p. 24153.

122. Cheng, Y.C., Z.Y. Zhu, W.B. Mi, Z.B. Guo, and U. Schwingenschloegl, *Prediction of two-dimensional diluted magnetic semiconductors: Doped monolayer $MoS_2$ systems.* Physical Review B, 2013. **87**(10): p. 100410.

123. Xu, W.-b., P. Li, S.-s. Li, B.-j. Huang, C.-w. Zhang, and P.-j. Wang, *A novel optical property induced by MO, S vacancy and V-doped in monolayer $MoS_2$.* Physica E-Low-Dimensional Systems & Nanostructures, 2015. **73**: p. 83-88.

124. Chen, Y., D.O. Dumcenco, Y. Zhu, X. Zhang, N. Mao, Q. Feng, M. Zhang, J. Zhang, P.-H. Tan, and Y.-S. Huang, *Composition-dependent Raman modes of $Mo_{1-x}W_xS_2$ monolayer alloys.* Nanoscale, 2014. **6**(5): p. 2833-2839.

125. Gong, Y., Z. Liu, A.R. Lupini, G. Shi, J. Lin, S. Najmaei, Z. Lin, A.L. Elias, A. Berkdemir, G. You, H. Terrones, M. Terrones, R. Vajtai, S.T. Pantelides, S.J. Pennycook, J. Lou, W. Zhou, and P.M. Ajayan, *Band gap engineering and layer-by-layer mapping of selenium-doped molybdenum disulfide.* Nano Letters, 2014. **14**(2): p. 442-449.

126. Xiang, Z., Z. Zhang, X. Xu, Q. Zhang, Q. Wang, and C. Yuan, *Room-temperature ferromagnetism in Co doped $MoS_2$ sheets.* Physical Chemistry Chemical Physics, 2015. **17**(24): p. 15822-15828.

127. Li, B., L. Huang, M. Zhong, N. Huo, Y. Li, S. Yang, C. Fan, J. Yang, W. Hu, Z. Wei, and J. Li, *Synthesis and transport properties of large-scale alloy $Co_{0.6}Mo_{0.84}S_2$ bilayer nano sheets.* Acs Nano, 2015. **9**(2): p. 1257-1262.

128. Suh, J., T.E. Park, D.Y. Lin, D. Fu, J. Park, H.J. Jung, Y. Chen, C. Ko, C. Jang, Y. Sun, R. Sinclair, J. Chang, S. Tongay, and J. Wu, *Doping against the native propensity of $MoS_2$: degenerate hole doping by cation substitution.* Nano Letters, 2014. **14**(12): p. 6976-6982.

129. Wang, W., A. Narayan, L. Tang, K. Dolui, Y. Liu, X. Yuan, Y. Jin, Y. Wu, I. Rungger, S. Sanvito, and F. Xiu, *Spin-valve effect in NiFe/$MoS_2$/NiFe junctions.* Nano Letters, 2015. **15**(8): p. 5261-5267.

130. Li, H., J. Shao, D. Yao, and G. Yang, *Gate-voltage-controlled spin and valley polarization transport in a normal/ferromagnetic/normal $MoS_2$ junction.* Acs Applied Materials & Interfaces, 2014. **6**(3): p. 1759-1764.

131. Yan, W., O. Txoperena, R. Llopis, H. Dery, L.E. Hueso, and F. Casanova, *A two-dimensional spin field-effect switch.* Nature communications, 2016. **7**: p. 13372.

132. Rashidian Vaziri, M., F. Hajiesmaeilbaigi, and M. Maleki, *Monte Carlo simulation of the subsurface growth mode during pulsed laser deposition.* Journal of Applied Physics, 2011. **110**(4): p. 043304.

133. Willmott, P. and J. Huber, *Pulsed laser vaporization and deposition.* Reviews of Modern Physics, 2000. **72**(1): p. 315.

134. Schey, B., T. Bollmeier, M. Kuhn, W. Biegel, and B. Stritzker, *Large area deposition of $YBa_2Cu_3O_{7-x}$ films by pulsed laser ablation.* Review of scientific instruments, 1998. **69**(2): p. 474-476.

135. Rashidian Vaziri, M., F. Hajiesmaeilbaigi, and M. Maleki, *Microscopic description of the thermalization process during pulsed laser deposition of aluminium in the presence of argon background gas.* Journal of Physics D Applied Physics, 2010. **43**: p. 425205.

136. Venables, J., G. Spiller, and M. Hanbucken, *Nucleation and growth of thin films.* Reports on progress in physics, 1984. **47**(4): p. 399.

137. Giacovazzo, C., H.L. Monaco, G. Artioli, D. Viterbo, G. Ferraris, and C. Giacovazzo, *Fundamentals of crystallography*. Vol. 7. 2002: Oxford University Press Oxford.

138. Goldstein, J.I., D.E. Newbury, J.R. Michael, N.W. Ritchie, J.H.J. Scott, and D.C. Joy, *Scanning electron microscopy and X-ray microanalysis*. 2017: Springer.

139. Horiuchi, S., *Fundamentals of high-resolution transmission electron microscopy*. Vol. 54. 1994: North-Holland Amsterdam.

140. Voigtländer, B., *Scanning probe microscopy*. 2015: Springer.

141. Lee, C., H. Yan, L.E. Brus, T.F. Heinz, J. Hone, and S. Ryu, *Anomalous lattice vibrations of single- and few-layer $MoS_2$.* Acs Nano, 2010. **4**(5): p. 2695-2700.

142. Bao, S.J., C.M. Li, J.F. Zang, X.Q. Cui, Y. Qiao, and J. Guo, *New nanostructured $TiO_2$ for direct electrochemistry and glucose sensor applications.* Advanced Functional Materials, 2008. **18**(4): p. 591-599.

143. Mor, G.K., K. Shankar, M. Paulose, O.K. Varghese, and C.A. Grimes, *Use of highly-ordered $TiO_2$ nanotube arrays in dye-sensitized solar cells.* Nano letters, 2006. **6**(2): p. 215-218.

144. Nakamura, I., N. Negishi, S. Kutsuna, T. Ihara, S. Sugihara, and K. Takeuchi, *Role of oxygen vacancy in the plasma-treated $TiO_2$ photocatalyst with visible light activity for NO removal.* Journal of Molecular Catalysis A: Chemical, 2000. **161**(1-2): p. 205-212.

145. Murugan, P., R. Belosludov, H. Mizuseki, T. Nishimatsu, T. Fukumura, M. Kawasaki, and Y. Kawazoe, *$TiO_2$ (rutile) doped with double impurities for fabricating spintronic devices—a combinatorial computational approach.* Measurement Science and Technology, 2004. **16**(1): p. 242.

146. Roberts, K.G., M. Varela, S. Rashkeev, S.T. Pantelides, S.J. Pennycook, and K.M. Krishnan, *Defect-mediated ferromagnetism in insulating Co-doped anatase $TiO_2$ thin films.* Physical review B, 2008. **78**(1): p. 014409.

147. Shinde, S.R., S.B. Ogale, J.S. Higgins, H. Zheng, A.J. Millis, V.N. Kulkarni, R. Ramesh, R.L. Greene, and T. Venkatesan, *Co-occurrence of superparamagnetism and anomalous Hall effect in highly reduced cobalt-doped rutile $TiO_2$-delta films.* Physical Review Letters, 2004. **92**(16): p. 166601.

148. Matsumoto, Y., M. Murakami, T. Shono, T. Hasegawa, T. Fukumura, M. Kawasaki, P. Ahmet, T. Chikyow, S. Koshihara, and H. Koinuma, *Room-temperature ferromagnetism in transparent transition metal-doped titanium dioxide.* Science, 2001. **291**(5505): p. 854-856.

149. Santara, B., B. Pal, and P.K. Giri, *Signature of strong ferromagnetism and optical properties of Co doped $TiO^2$ nanoparticles.* Journal of Applied Physics, 2011. **110**(11): p. 114322.

150. Bryan, J.D., S.A. Santangelo, S.C. Keveren, and D.R. Gamelin, *Activation of high-Tc ferromagnetism in $Co^{2+}$:$TiO^2$ and $Cr^{3+}$:$TiO^2$ nanorods and nanocrystals by grain boundary defects.* Journal of the American Chemical Society, 2005. **127**(44): p. 15568-15574.

151. Saadaoui, H., X. Luo, Z. Salman, X.Y. Cui, N.N. Bao, P. Bao, R.K. Zheng, L.T. Tseng, Y.H. Du, T. Prokscha, A. Suter, T. Liu, Y.R. Wang, S. Li, J. Ding, S.P. Ringer, E. Morenzoni, and J.B. Yi, *Intrinsic ferromagnetism in the diluted magnetic semiconductor Co: $TiO_2$.* Physical Review Letters, 2016. **117**(22): p. 227202.

152. Gutfleisch, O., M.A. Willard, E. Bruck, C.H. Chen, S.G. Sankar, and J.P. Liu, *Magnetic materials and devices for the 21st century: Stronger, lighter, and more energy efficient.* Advanced Materials, 2011. **23**(7): p. 821-842.

153. Billas, I.M.L., A. Chatelain, and W.A. Deheer, *Magnetism from the atom to the bulk in iron, cobalt, and nickel clusters.* Science, 1994. **265**(5179): p. 1682-1684.

154. Billas, I.M.L., J.A. Becker, A. Chatelain, and W.A. Deheer, *Magnetic moments of iron clusters with 25 to 700 atoms and their dependence on temperature.* Physical Review Letters, 1993. **71**(24): p. 4067-4070.

155. Ji, N., V. Lauter, X.W. Zhang, H. Ambaye, and J.P. Wang, *Strain induced giant magnetism in epitaxial $Fe_{16}N_2$ thin film.* Applied Physics Letters, 2013. **102**(7): p. 072411.

156. Donati, F., S. Rusponi, S. Stepanow, C. Wackerlin, A. Singha, L. Persichetti, R. Baltic, K. Diller, F. Patthey, E. Fernandes, J. Dreiser, Z. Sljivancanin, K. Kummer, C. Nistor, P. Gambardella, and H. Brune, *Magnetic remanence in single atoms.* Science, 2016. **352**(6283): p. 318-321.

157. Ogale, S.B., R.J. Choudhary, J.P. Buban, S.E. Lofland, S.R. Shinde, S.N. Kale, V.N. Kulkarni, J. Higgins, C. Lanci, J.R. Simpson, N.D. Browning, S. Das Sarma, H.D. Drew, R.L. Greene, and T. Venkatesan, *High temperature ferromagnetism with a giant magnetic moment in transparent Co-doped $SnO_2$-delta.* Physical Review Letters, 2003. **91**(7): p. 077205.

158. Dhar, S., O. Brandt, M. Ramsteiner, V.F. Sapega, and K.H. Ploog, *Colossal magnetic moment of Gd in GaN.* Physical Review Letters, 2005. **94**(3): p. 037205.

159. Du, Y.H., Y. Zhu, S.B. Xi, P. Yang, H.O. Moser, M.B.H. Breese, and A. Borgna, *XAFCA: a new XAFS beamline for catalysis research.* Journal of Synchrotron Radiation, 2015. **22**: p. 839-843.

160. Klimenkov, M., J. von Borany, W. Matz, D. Eckert, M. Wolf, and K.H. Muller, *Structure and magnetic properties of Co nanoclusters fabricated by ion beam synthesis in $SiO_2$ films.* Applied Physics a-Materials Science & Processing, 2002. **74**(4): p. 571-575.

161. Kim, D., J. Yang, Y. Kim, D.-W. Kim, T. Noh, S. Bu, Y.-W. Kim, Y. Park, S. Pearton, and Y. Jo, *Superparamagnetism in Co-ion-implanted anatase $TiO_2$ thin films and effects of postannealing.* Applied physics letters, 2003. **83**(22): p. 4574-4576.

162. Chen, C.T., Y.U. Idzerda, H.J. Lin, N.V. Smith, G. Meigs, E. Chaban, G.H. Ho, E. Pellegrin, and F. Sette, *Experimental confirmation of the x-ray magnetic circular-dichroism sum-rules for iron and cobalt.* Physical Review Letters, 1995. **75**(1): p. 152-155.

163. Singh, V.R., K. Ishigami, V.K. Verma, G. Shibata, Y. Yamazaki, T. Kataoka, A. Fujimori, F.H. Chang, D.J. Huang, H.J. Lin, C.T. Chen, Y. Yamada, T. Fukumura, and M. Kawasaki, *Ferromagnetism of cobalt-doped anatase $TiO_2$ studied by bulk- and surface-sensitive soft x-ray magnetic circular dichroism.* Applied Physics Letters, 2012. **100**(24): p. 242404.

164. Krasienapibal, T.S., T. Fukumura, and T. Hasegawa, *The recovery of a magnetically dead layer on the surface of an anatase $(Ti,Co)O_2$ thin film via an ultrathin $TiO_2$ capping layer.* Electronics, 2017. **6**(1): p. 23.

165. Parkin, S.S.P., R. Sigsbee, R. Felici, and G.P. Felcher, *Observation of magnetic dead layers at the surface of iron-oxide films.* Applied Physics Letters, 1986. **48**(9): p. 604-606.

166. Luo, W.D., S.J. Pennycook, and S.T. Pantelides, *Magnetic "dead" layer at a complex oxide interface.* Physical Review Letters, 2008. **101**(24): p. 247204.

167. Nikolaev, S.A. and I.V. Solovyev, *Orbital magnetization of insulating perovskite transition-metal oxides with a net ferromagnetic moment in the ground state.* Physical Review B, 2014. **89**(6): p. 064428.

168. Peters, L., I. Di Marco, O. Granas, E. Sasioglu, A. Altun, S. Rossen, C. Friedrich, S. Blugel, M.I. Katsnelson, A. Kirilyuk, and O. Eriksson, *Correlation effects and orbital magnetism of Co clusters.* Physical Review B, 2016. **93**(22): p. 224428.

169. Arroyo-de Dompablo, M.E., A. Morales-Garcia, and M. Taravillo, *DFT plus U calculations of crystal lattice, electronic structure, and phase stability under pressure of $TiO_2$ polymorphs.* Journal of Chemical Physics, 2011. **135**(5): p. 054503.

170. Perdew, J.P., K. Burke, and M. Ernzerhof, *Generalized gradient approximation made simple.* Physical Review Letters, 1996. **77**(18): p. 3865-3868.

171. Heyd, J., G.E. Scuseria, and M. Ernzerhof, *Hybrid functionals based on a screened Coulomb potential.* Journal of Chemical Physics, 2003. **118**(18): p. 8207-8215.
172. Kresse, G. and J. Furthmuller, *Efficient iterative schemes for ab initio total-energy calculations using a plane-wave basis set.* Physical Review B, 1996. **54**(16): p. 11169.
173. Moruzzi, V.L., *Singular volume dependence of transition-metal magnetism.* Physical Review Letters, 1986. **57**(17): p. 2211-2214.
174. Meyer, A.J.P. and G. Asch, *Experimental g' and g values of Fe, Co, Ni, and their alloys.* Journal of Applied Physics, 1961. **32**(3): p. S330.
175. Ceresoli, D., U. Gerstmann, A.P. Seitsonen, and F. Mauri, *First-principles theory of orbital magnetization.* Physical Review B, 2010. **81**(6): p. 060409.
176. Sharma, S., S. Pittalis, S. Kurth, S. Shallcross, J.K. Dewhurst, and E.K.U. Gross, *Comparison of exact-exchange calculations for solids in current-spin-density- and spin-density-functional theory.* Physical Review B, 2007. **76**(10): p. 100401.
177. Langenberg, A., K. Hirsch, A. Lawicki, V. Zamudio-Bayer, M. Niemeyer, P. Chmiela, B. Langbehn, A. Terasaki, B.V. Issendorff, and J.T. Lau, *Spin and orbital magnetic moments of size-selected iron, cobalt, and nickel clusters.* Physical Review B, 2014. **90**(18): p. 184420.
178. Chambers, S., S. Thevuthasan, R. Farrow, R. Marks, J. Thiele, L. Folks, M. Samant, A. Kellock, N. Ruzycki, and D. Ederer, *Epitaxial growth and properties of ferromagnetic co-doped $TiO_2$ anatase.* Applied Physics Letters, 2001. **79**(21): p. 3467-3469.
179. Cortie, D.L., Y. Khaydukov, T. Keller, D.J. Sprouster, J.S. Hughes, J.P. Sullivan, X.L. Wang, A.P. Le Brun, J. Bertinshaw, S.J. Callori, R. Aughterson, M. James, P.J. Evans, G. Triani, and F. Klose, *Enhanced magnetization of cobalt defect clusters embedded in $TiO_2$-delta films.* Acs Applied Materials & Interfaces, 2017. **9**(10): p. 8783-8795.
180. Qiang, Y., R.F. Sabiryanov, S.S. Jaswal, Y. Liu, H. Haberland, and D.J. Sellmyer, *Magnetism of Co nanocluster films.* Physical Review B, 2002. **66**(6): p. 064404.
181. Guevara, J., A.M. Llois, F. Aguilera-Granja, and J.M. Montejano-Carrizales, *Structural evolution of free Co cluster magnetism.* Solid State Communications, 1999. **111**(6): p. 335-340.

182. Souto-Casares, J., M. Sakurai, and J.R. Chelikowsky, *Structural and magnetic properties of large cobalt clusters.* Physical Review B, 2016. **93**(17): p. 174418.
183. Sellmyer, D., M. Zheng, and R. Skomski, *Magnetism of Fe, Co and Ni nanowires in self-assembled arrays.* Journal of Physics: Condensed Matter, 2001. **13**(25): p. R433.
184. Peredkov, S., M. Neeb, W. Eberhardt, J. Meyer, M. Tombers, H. Kampschulte, and G. Niedner-Schatteburg, *Spin and orbital magnetic moments of free nanoparticles.* Physical Review Letters, 2011. **107**(23): p. 233401.
185. Payne, F.W., W. Jiang, J.W. Emmert, J. Deng, and L.A. Bloomfield, *Magnetic structure of free cobalt clusters studied with Stern-Gerlach deflection experiments.* Physical Review B, 2007. **75**(9): p. 094431.
186. Meyer, J., M. Tombers, C. van Wullen, G. Niedner-Schatteburg, S. Peredkov, W. Eberhardt, M. Neeb, S. Palutke, M. Martins, and W. Wurth, *The spin and orbital contributions to the total magnetic moments of free Fe, Co, and Ni clusters.* Journal of Chemical Physics, 2015. **143**(10): p. 104302.
187. Koch, S.A., G. Palasantzas, T. Vystavel, J.T.M. De Hosson, C. Binns, and S. Louch, *Magnetic and structural properties of Co nanocluster thin films.* Physical Review B, 2005. **71**(8): p. 085410.
188. Parras, M., A.u. Varela, R. Cortés-Gil, K. Boulahya, A. Hernando, and J.M. González-Calbet, *Room-temperature ferromagnetism in reduced rutile $TiO_{2-\delta}$ nanoparticles.* The Journal of Physical Chemistry Letters, 2013. **4**(13): p. 2171-2176.
189. Zhou, S., E. Čižmár, K. Potzger, M. Krause, G. Talut, M. Helm, J. Fassbender, S. Zvyagin, J. Wosnitza, and H. Schmidt, *Origin of magnetic moments in defective $TiO_2$ single crystals.* Physical Review B, 2009. **79**(11): p. 113201.
190. Lee, C., X.D. Wei, J.W. Kysar, and J. Hone, *Measurement of the elastic properties and intrinsic strength of monolayer graphene.* Science, 2008. **321**(5887): p. 385-388.
191. Deng, J., P.J. Ren, D.H. Deng, and X.H. Bao, *Enhanced electron penetration through an ultrathin graphene layer for highly efficient catalysis of the hydrogen evolution reaction.* Angewandte Chemie-International Edition, 2015. **54**(7): p. 2100-2104.
192. Avouris, P., *Graphene: Electronic and photonic properties and devices.* Nano Letters, 2010. **10**(11): p. 4285-4294.

193. Batzill, M., *The surface science of graphene: Metal interfaces, CVD synthesis, nanoribbons, chemical modifications, and defects.* Surface Science Reports, 2012. **67**(3-4): p. 83-115.

194. Mohiuddin, T.M.G., A. Lombardo, R.R. Nair, A. Bonetti, G. Savini, R. Jalil, N. Bonini, D.M. Basko, C. Galiotis, N. Marzari, K.S. Novoselov, A.K. Geim, and A.C. Ferrari, *Uniaxial strain in graphene by Raman spectroscopy: G peak splitting, Gruneisen parameters, and sample orientation.* Physical Review B, 2009. **79**(20): p. 205433.

195. Ahmed, S. and J. Yi, *Two-dimensional transition metal dichalcogenides and their charge carrier mobilities in field-effect transistors.* Nano-Micro Letters, 2017. **9**(4): p. 50-72.

196. Ataca, C., H. Sahin, and S. Ciraci, *Stable, single-layer $MX_2$ transition-metal oxides and dichalcogenides in a honeycomb-like structure.* Journal of Physical Chemistry C, 2012. **116**(16): p. 8983-8999.

197. Wang, F., Z. Wang, Q. Wang, F. Wang, L. Yin, K. Xu, Y. Huang, and J. He, *Synthesis, properties and applications of 2D non-graphene materials.* Nanotechnology, 2015. **26**(29): p. 292001.

198. Benameur, M.M., B. Radisavljevic, J.S. Heron, S. Sahoo, H. Berger, and A. Kis, *Visibility of dichalcogenide nanolayers.* Nanotechnology, 2011. **22**(12): p. 125706.

199. Lukowski, M.A., A.S. Daniel, F. Meng, A. Forticaux, L. Li, and S. Jin, *Enhanced hydrogen evolution catalysis from chemically exfoliated metallic MoS2 nanosheets.* Journal of the American Chemical Society, 2013. **135**(28): p. 10274-10277.

200. Loo, A.H., A. Bonanni, A. Ambrosi, and M. Pumera, *Molybdenum disulfide ($MoS_2$) nanoflakes as inherently electroactive labels for DNA hybridization detection.* Nanoscale, 2014. **6**(20): p. 11971-11975.

201. Lee, K., H.Y. Kim, M. Lotya, J.N. Coleman, G.T. Kim, and G.S. Duesberg, *Electrical characteristics of molybdenum disulfide flakes produced by liquid exfoliation.* Advanced Materials, 2011. **23**(36): p. 4178-4182.

202. Feng, L.P., N. Li, M.H. Yang, and Z.T. Liu, *Effect of pressure on elastic, mechanical and electronic properties of $WSe_2$: A first-principles study.* Materials Research Bulletin, 2014. **50**: p. 503-508.

203. Zhou, Y., P. Yang, H. Zu, F. Gao, and X. Zu, *Electronic structures and magnetic properties of $MoS_2$ nanostructures: atomic defects, nanoholes, nanodots and antidots.* Physical Chemistry Chemical Physics, 2013. **15**(25): p. 10385-10394.

204. Li, W.B. and J. Li, *Ferroelasticity and domain physics in two-dimensional transition metal dichalcogenide monolayers.* Nature Communications, 2016. **7**: p. 10843.

205. Wang, Y.R., S.A. Li, and J.B. Yi, *Electronic and magnetic properties of Co doped $MoS_2$ monolayer.* Scientific Reports, 2016. **6**: p. 24153.

206. Wang, Y.R., L.T. Tseng, P.P. Murmu, N.N. Bao, J. Kennedy, M. Ionesc, J. Ding, K. Suzuki, S. Li, and J.B. Yi, *Defects engineering induced room temperature ferromagnetism in transition metal doped $MoS_2$.* Materials & Design, 2017. **121**: p. 77-84.

207. Ahmed, S., X. Ding, N.N. Bao, P.J. Bian, R.K. Zheng, Y.R. Wang, P.P. Murmu, J.V. Kennedy, R. Liu, H.M. Fan, K. Suzuki, J. Ding, and J.B. Yi, *Inducing high coercivity in $MoS_2$ nanosheets by transition element doping.* Chemistry of Materials, 2017. **29**(21): p. 9066-9074.

208. Sagynbaeva, M., P. Panigrahi, Y. Li, M. Ramzan, and R. Ahuja, *Tweaking the magnetism of $MoS_2$ nanoribbon with hydrogen and carbon passivation.* Nanotechnology, 2014. **25**(16): p. 165703.

209. Mao, X.Z., Y. Xu, Q.X. Xue, W.X. Wang, and D.Q. Gao, *Ferromagnetism in exfoliated tungsten disulfide nanosheets.* Nanoscale Research Letters, 2013. **8**: p. 430-435.

210. Li, W.F., C.M. Fang, and M.A. van Huis, *Strong spin-orbit splitting and magnetism of point defect states in monolayer WS2.* Physical Review B, 2016. **94**(19): p. 195425.

211. Olivas, A., I. Villalpando, S. Sepulveda, O. Perez, and S. Fuentes, *Synthesis and magnetic characterization of nanostructures N/$WS_2$, where N=Ni, Co and Fe.* Materials Letters, 2007. **61**(21): p. 4336-4339.

212. Xie, L.Y. and J.M. Zhang, *Electronic structures and magnetic properties of the transition-metal atoms (Mn, Fe, Co and Ni) doped $WS_2$: A first-principles study.* Superlattices and Microstructures, 2016. **98**: p. 148-157.

213. Zhao, X., C.X. Xia, X.Q. Dai, T.X. Wang, P. Chen, and L. Tian, *Electronic and magnetic properties of X-doped (X=Ni, Pd, Pt) $WS_2$ monolayer.* Journal of Magnetism and Magnetic Materials, 2016. **414**: p. 45-48.

214. Zhu, B., H. Zeng, J. Dai, Z. Gong, and X. Cui, *Anomalously robust valley polarization and valley coherence in bilayer $WS_2$.* Proceedings of the National Academy of Sciences of the United States of America, 2014. **111**(32): p. 11606-11611.

215. Piao, J.Y., L.T. Tseng, and J.B. Yi, *Ferromagnetism in Sm doped ZnO nanorods by a hydrothermal method.* Chemical Physics Letters, 2016. **649**: p. 19-22.

216. Wang, Y.R., J.Y. Piao, Y.H. Lu, S.A. Li, and J.B. Yi, *Intrinsic ferromagnetism in Sm doped ZnO.* Materials Research Bulletin, 2016. **83**: p. 408-413.

217. Stengl, V., S. Bakardjieva, and N. Murafa, *Preparation and photocatalytic activity of rare earth doped TiO2 nanoparticles.* Materials Chemistry and Physics, 2009. **114**(1): p. 217-226.

218. Zheng, J.H., J.L. Song, Z. Zhao, Q. Jiang, and J.S. Lian, *Optical and magnetic properties of Nd-doped ZnO nanoparticles.* Crystal Research and Technology, 2012. **47**(7): p. 713-718.

219. Luo, X., L.T. Tseng, W.T. Lee, G.Z. Xing, T. Liu, S. Li, and J.B. Yi, *Monodispersed ZnO quantum dots with Nd doping.* Nanoscience and Nanotechnology Letters, 2015. **7**(5): p. 417-421.

220. Kumar, S. and P.D. Sahare, *Nd-doped ZnO as a multifunctional nanomaterial.* Journal of Rare Earths, 2012. **30**(8): p. 761-768.

221. Wang, D.D., Q. Chen, G.Z. Xing, J.B. Yi, S.R. Bakaul, J. Ding, J.L. Wang, and T. Wu, *Robust room-temperature ferromagnetism with giant anisotropy in Nd-doped ZnO nanowire arrays.* Nano Letters, 2012. **12**(8): p. 3994-4000.

222. Berkdemir, A., H.R. Gutierrez, A.R. Botello-Mendez, N. Perea-Lopez, A.L. Elias, C.I. Chia, B. Wang, V.H. Crespi, F. Lopez-Urias, J.C. Charlier, H. Terrones, and M. Terrones, *Identification of individual and few layers of $WS_2$ using Raman Spectroscopy.* Scientific Reports, 2013. **3**: p. 1755-1762.

223. Zeng, H.L., G.B. Liu, J.F. Dai, Y.J. Yan, B.R. Zhu, R.C. He, L. Xie, S.J. Xu, X.H. Chen, W. Yao, and X.D. Cui, *Optical signature of symmetry variations and spin-valley coupling in atomically thin tungsten dichalcogenides.* Scientific Reports, 2013. **3**: p. 1608-1612.

224. Chakraborty, B., A. Bera, D.V.S. Muthu, S. Bhowmick, U.V. Waghmare, and A.K. Sood, *Symmetry-dependent phonon renormalization in monolayer $MoS_2$ transistor.* Physical Review B, 2012. **85**(16): p. 161403.

225. Mao, N.N., Y.F. Chen, D.M. Liu, J. Zhang, and L.M. Xie, *Solvatochromic Effect on the Photoluminescence of $MoS_2$ Monolayers.* Small, 2013. **9**(8): p. 1312-1315.

226. McDonnell, S., R. Addou, C. Buie, R.M. Wallace, and C.L. Hinkle, *Defect-dominated doping and contact resistance in $MoS_2$.* Acs Nano, 2014. **8**(3): p. 2880-2888.

227. Xu, Z.Q., Y.P. Zhang, S.H. Lin, C.X. Zheng, Y.L. Zhong, X. Xia, Z.P. Li, P.J. Sophia, M.S. Fuhrer, Y.B. Cheng, and Q.L. Bao, *Synthesis and transfer of large-area monolayer $WS_2$ crystals: Moving toward the recyclable use of sapphire substrates.* Acs Nano, 2015. **9**(6): p. 6178-6187.

228. Donarelli, M., F. Bisti, F. Perrozzi, and L. Ottaviano, *Tunable sulfur desorption in exfoliated $MoS_2$ by means of thermal annealing in ultra-high vacuum.* Chemical Physics Letters, 2013. **588**: p. 198-202.

229. Ye, G.L., Y.J. Gong, J.H. Lin, B. Li, Y.M. He, S.T. Pantelides, W. Zhou, R. Vajtai, and P.M. Ajayan, *Defects Engineered Monolayer $MoS_2$ for Improved Hydrogen Evolution Reaction.* Nano Letters, 2016. **16**(2): p. 1097-1103.

230. Arizumi, T., T. Mizutani, and K. Shimakawa, *EPR study on surface properties of ZnS and CdS.* Japanese Journal of Applied Physics, 1969. **8**(12): p. 1411-1416.

231. Ma, Y., Y. Lu, J. Yi, Y. Feng, T. Herng, X. Liu, D. Gao, D. Xue, J. Xue, and J. Ouyang, *Room temperature ferromagnetism in Teflon due to carbon dangling bonds.* Nature communications, 2012. **3**: p. 727.

232. Zheng, H.L., B.S. Yang, D.D. Wang, R.L. Han, X.B. Du, and Y. Yan, *Tuning magnetism of monolayer $MoS_2$ by doping vacancy and applying strain.* Applied Physics Letters, 2014. **104**(13): p. 132403.

233. Zhao, X., X.Q. Dai, C.X. Xia, and T.X. Wang, *Structural defects in pristine and Mn-doped monolayer $WS_2$: A first-principles study*. Superlattices and Microstructures, 2015. **85**: p. 339-347.

234. de Araujo, A.E.P., F.L.A. Machado, A.R. Rodrigues, A. Azevedo, F.M. de Aguiar, J.R.L. de Almeida, S.M. Rezende, and W.F. Egelhoff, *Spin-glass and random-field effects in exchange-biased NiFe film on a NiO single-crystal substrate.* Journal of Applied Physics, 2002. **91**(10): p. 7754-7756.

235. Imry, Y. and S.-k. Ma, *Random-field instability of the ordered state of continuous symmetry.* Physical Review Letters, 1975. **35**(21): p. 1399.

236. Nattermann, T. and I. Vilfan, *Anomalous relaxation in the random-field Ising-model and related systems.* Physical Review Letters, 1988. **61**(2): p. 223-226.

237. Jones, P., E. Knözinger, W. Langel, R. Moyes, and J. Tomkinson, *Adsorption of molecular hydrogen at high pressure and temperature on $MoS_2$ and $WS_2$; observed by inelastic neutron scattering.* Surface science, 1988. **207**(1): p. 159-176.

238. Li, X., Q. Xin, X. Guo, P. Grange, and B. Delmon, *Reversible hydrogen adsorption on $MoS_2$ studied by temperature-programmed desorption and temperature-programmed reduction.* Journal of Catalysis, 1992. **137**(2): p. 385-393.

239. Ouyang, F.P., X. Ni, Z.X. Yang, Y. Chen, X.J. Zheng, and X. Xiong, *Effects of edge hydrogenation on structural stability, electronic, and magnetic properties of $WS_2$ nanoribbons.* Journal of Applied Physics, 2013. **114**(21): p. 213710.

240. Li, W., A.I. Frenkel, J.C. Woicik, C. Ni, and S.I. Shah, *Dopant location identification in $Nd^{3+}$-doped $TiO_2$ nanoparticles.* Physical Review B, 2005. **72**(15): p. 155315.

241. Atuchin, V.V., T.A. Gavrilova, J.C. Grivel, and V.G. Kesler, *Electronic structure of layered titanate $Nd_2Ti_2O_7$.* Surface Science, 2008. **602**(19): p. 3095-3099.

242. Sim, D.M., M. Kim, S. Yim, M.J. Choi, J. Choi, S. Yoo, and Y.S. Jung, *Controlled doping of vacancy-containing few-layer $MoS_2$ via highly stable thiol-based molecular chemisorption.* Acs Nano, 2015. **9**(12): p. 12115-12123.

243. Nan, H.Y., Z.L. Wang, W.H. Wang, Z. Liang, Y. Lu, Q. Chen, D.W. He, P.H. Tan, F. Miao, X.R. Wang, J.L. Wang, and Z.H. Ni, *Strong photoluminescence enhancement of $MoS_2$ through defect engineering and oxygen bonding.* Acs Nano, 2014. **8**(6): p. 5738-5745.

244. Xing, G.Z., J.B. Yi, F. Yan, T. Wu, and S. Li, *Positive magnetoresistance in ferromagnetic Nd-doped $In_2O_3$ thin films grown by pulse laser deposition.* Applied Physics Letters, 2014. **104**(20): p. 202411.

245. Matte, H., K.S. Subrahmanyam, and C.N.R. Rao, *Novel magnetic properties of graphene: Presence of both ferromagnetic and antiferromagnetic features and other aspects.* Journal of Physical Chemistry C, 2009. **113**(23): p. 9982-9985.

246. Le, D., T.B. Rawal, and T.S. Rahman, *Single-layer $MoS_2$ with sulfur vacancies: Structure and catalytic application.* Journal of Physical Chemistry C, 2014. **118**(10): p. 5346-5351.

247. Komsa, H.-P., S. Kurasch, O. Lehtinen, U. Kaiser, and A.V. Krasheninnikov, *From point to extended defects in two-dimensional $MoS_2$: Evolution of atomic structure under electron irradiation.* Physical Review B, 2013. **88**(3): p. 035301.